A Carrier-Suppressing Interferometer for Ultra-Low-Noise Amplitude- and Phase-Detection

Vom Promotionsausschuss der
Technischen Universität Hamburg
zur Erlangung des akademischen Grades
Doktor-Ingenieurin (Dr.-Ing.)

genehmigte Dissertation

von
Louise Springer

aus
Hamburg

2023

First Examiner:	Prof. Dr.-Ing. Arne F. Jacob
Second Examiner:	Prof. Dr.-Ing. Alexander Kölpin
Third Examiner:	Dr. Holger Schlarb
Chair of Examination Board:	Prof. Dr.-Ing. Herbert Werner

Date of Thesis Defense: March 31, 2023

Summary

This thesis introduces a Carrier-Suppression Interferometer (CSI) and considers the enhancement of the noise performance of the control system for linear particle accelerators at DESY without the necessity of re-designing and modifying the existing core components. A good starting point is found in the RF detection front-end picking up the RF field inside the accelerating cavities. The introduced method suppresses the carrier by destructive signal interference. Optimized versions of this fundamental approach in radio-frequency (RF) signal detection can in principle be found in literature together with the underlying theory. However, the actual application in a particle accelerator context has not been demonstrated so far.

This work is based on a proof-of-principle of the CSI at an operating frequency of 1.3 GHz. There, the detection resolution of the conventional control system for linear accelerators at DESY of −147 dBc/Hz was improved to a white noise detection level of −175 dBc/Hz at an offset frequency of 1 MHz and an integrated timing jitter of below 100 as in a control bandwidth of 20 kHz. During the investigations presented in this thesis, the noise floor of the detection system is further increased to −205 dBc/Hz at an offset of 1 MHz, yielding a timing jitter of 10.8 as in the measuring band from 40 Hz to 1 MHz. This achievement is possible due to an intensive investigation on noise sources in the setup and its environment as well as connected steady improvements regarding stability and noise reduction. After an introductory section and a brief theory overview, the most relevant phase and amplitude measurement methods are described. Against this background, the new method is introduced and the implementation process of the CSI measurement setup as well as associated challenges and limits are discussed. Followed by this, the application of the CSI setup as a noise analyzer in the laboratory is discussed and obtained results are shown. The latter include the extensive noise investigation of RF components, such as different phase shifter technologies based on passive switches, varactor diodes, capacitors, and mechanical waveguide structures, necessary for the compactification and automation of the measurement setup. In the end, a proposal for the application of the CSI in the accelerator control loop for CW machines is given and upcoming tasks and challenges are discussed.

Acknowledgment

I would like to take the opportunity to thank all the people who have supported me along this long road.

First of all, my thanks go to my doctoral supervisor Prof. Dr.-Ing. Arne Jacob from the Hamburg University of Technology, who enabled this dissertation, supported me on many levels and encouraged me more than once along the way.

I would like to thank my supervisors at DESY, Dr. Frank Ludwig and Dr. Uroš Mavrič, for their valuable support and openness to discussions and questions. Of course, Dr. Holger Schlarb and the entire DESY infrastructure enabled me to do this research and I am very grateful for them giving me this opportunity. In addition, I would like to thank all of my other colleagues at MSK, especially in the Analog Electronics group, for always supporting and never rejecting me. The working students Volodomyr Vasylyuk and Johannes Voss accelerated the research project and I would like to thank them for accompanying me during my doctorate.

My friends and family each individually showed a tremendous amount of patience, understanding, and love. Thank you. I do not want to miss the chance to say thank you to my parents and my brother, who always believed in my abilities and supported my interests.

Finally and most important, I would like to say thank you to you, Djam. Thank you for taking care that I don't lose myself or the orientation on this rough journey. Without you being by my side, I would not have been able to carry on.

Contents

1 Introduction

The Deutsches Elektronen-Synchrotron (DESY), part of the Helmholtz Association of German Research Centers, is one of the world's leading accelerator research centers and operates several of the most brilliant light sources in the world, giving answers to fundamental questions in science. A large variety of technologies tightly connected to each other is hidden behind generating X-rays of high intensity and extremly short pulse durations for sophisticated experiments. DESY has different accelerator facilities on site for accelerator research as well as industrial and scientific usage. Next to the research on novel accelerator concepts, such as plasma accelerators, two main acceleration concepts dominate the facilities today: circular ring accelerators like the synchrotron storage ring PETRA III [1], and linear accelerators like the European X-Ray Free-Electron Laser (EuXFEL) [2]. Additionally, the Free-Electron Laser Hamburg (FLASH) is used for fundamental and applied sciences from many different disciplines as well as accelerator research and development. Its ultra-short and soft (i.e., relatively long-wavelength) X-ray pulses are used for a wide variety of research fields such as molecular biology, chemistry, and materials science. The properties of the photon pulses from FLASH allow scientists for instance to monitor ultra-fast chemical and molecular processes non-destructively in time domain and understand the underlying mechanisms [3], [4]. The ultra-short X-ray pulses generated at EuXFEL enable scientist to monitor these processes with much higher spatial and time resolution.

With an electron energy of 17.5 GeV and 10 pulses of 2700 electron bunches per second, the EuXFEL is one of the most powerful linear accelerator (LINAC) facilities in the world. Measuring a length of 3.3 km from the gun over the superconducting niobium cavities to the experiment beam lines, it crosses the border between the two German federated states Hamburg and Schleswig-Holstein and brings together experts and organizations from all over the world.

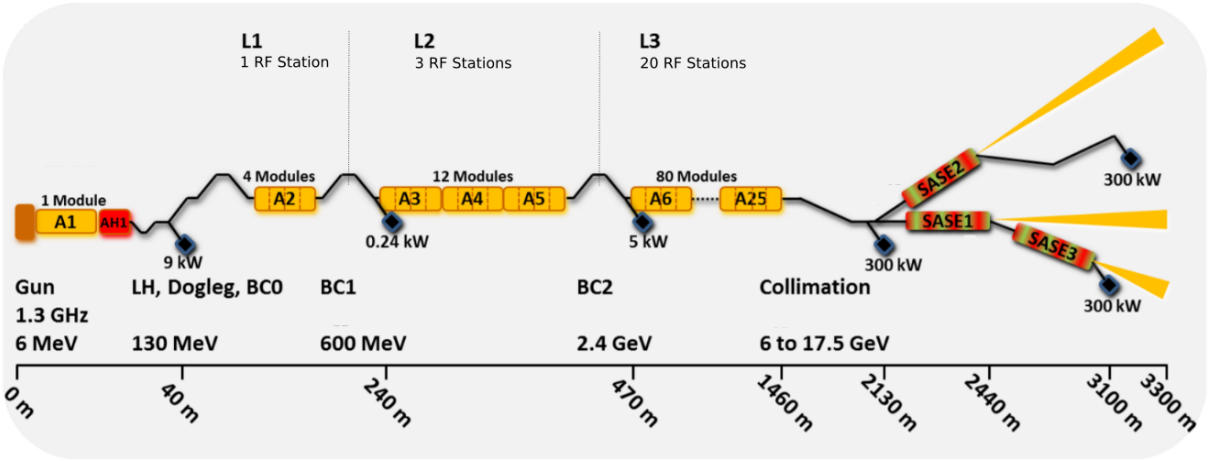

Figure 1.1: Schematic diagram of the EuXFEL [5].

1.1 The Low-Level RF System

To provide the EuXFEL users with such bright X-rays, a complex control system is necessary and thereby at the heart of the entire accelerator facility: The EuXFEL consists of a photo-injector (a so-called gun) where bunched electron beams are produced by directing a laser onto a photo-cathode. The beam is then further accelerated in superconducting niobium cavities to a final energy of 17.5 GeV. The beam is longitudinally compressed at intermediate energy levels in magnetic bunch compressors at time scales from a few picoseconds to a few femtoseconds. A stable compression requires precise control of the RF field in the accelerator cavities. Depending on the spatial spread of the incident electron bunches and their arrival time accuracy, succeeding undulator sections lead to the generation of photons for the experiments by deflection of the electrons [6].

The RF field jitter in the cavity, which describes the shaking of, e.g., the phase of the field in time domain, corresponds to the arrival time jitter of the electron bunches. This is due to the fact, that accelerating field variations in amplitude and phase result in a change in electron beam energy. In the energy dependent path length inside the magnetic bunch compressors, this variation translates into changes in arrival time and peak current of the beam. The accelerating RF field is detected and controlled accordingly, directly correlating with the arrival time accuracy of the electron bunches [7], [8]. This is crucial for a variety of experiments, for instance pump-probe experiments, which are of main interest at the EuXFEL [9]. To achieve high field stabilities, a so-called Low-Level RF (LLRF)-system is installed. It is comprised of several detection and diagnostics components. The term

"Low-Level" is used since typically only signal levels of below 1 W are processed in the system, while the high-power RF part commonly deals with power levels in the pre-amplifiers, klystrons and waveguides, which are three to six orders of magnitude larger.

As shown in Figure 1.1, the LINAC is composed of different sections. Each acceleration section includes so-called RF stations, controlled by the LLRF-system. A block diagram of the LLRF-control loop is displayed in Figure 1.2.

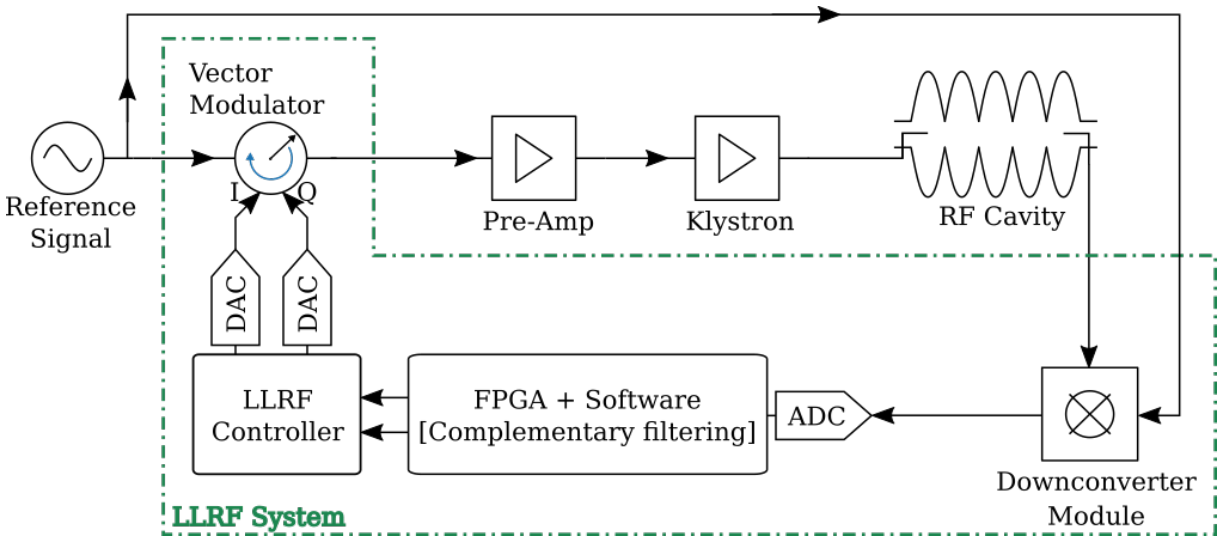

Figure 1.2: Basic schematic of the LLRF-system.

Picked up from the cavity with an antenna, the RF signal enters the LLRF system, which feeds the corrected signal back to the klystron and the accelerating cavity [10], [11]. The reference signal is provided by the main oscillator. In detail, the LLRF-system fulfills multiple tasks:

1. The field detection - A probe close to the cavity end-cell picks up the accelerating electromagnetic field, which carries all distortions and inaccuracies. This RF signal is downconverted by a frequency mixer. The intermediate frequency (IF) signal is digitized by an analog-to-digital converter (ADC), which is one of the key components in the system. Since the ADC is one of the major noise contributors, the work in this thesis tries to mitigate its influence.

2. The control - The digital signal passes a data processing unit. The data stream, divided into a real and an imaginary part, is filtered and adjusted by

a rotation matrix and gain fitted according to the selected operating point of the controller. The error values are calculated for the signal adjustment. The better the resolution of the signal detection is, the more precise the error calculation can be. The feedback signals are calculated and converted back to analog signals.

3. The actuator section - The signal correction follows within the actuator section, which includes a vector modulator, a pre-amplifier, and a klystron. The vector modulator, controlled by the feedback signals, adjusts the reference signal from the main oscillator such that the accelerating electromagnetic field inside the cavities increases in accuracy and stability. The vector modulator signal is amplified by a klystron and its pre-amplifier before heading back to the cavity and closing the loop.

This certainly is a much-simplified representation of the capabilities and duties of the LLRF-system, but it underlines its primary task, i.e., maintaining the phase and amplitude of the cavity's accelerating RF field. This thesis is based on an underlying project with the aim of improving the RF field detector performance of the system: the idea is to develop an advanced receiver front-end based on the principle of suppressing the carrier to enhance the detection resolution and lower the overall accelerator timing jitter. This thesis discusses the method of suppressing the carrier, shows the advantages and disadvantages, and the implementation progress.

Even with ideal noise behavior of the detector, the performance of the overall system still depends on many sub-factors, e.g., the controller gain and the quality factor of the cavity. In the current receiver concept, apart from the downconverter noise, the ADC noise dominates the overall system noise performance. There has been only little development progress regarding noise performance for ADCs over the past decade. The components have improved in speed, but not necessarily in noise [7], [8]. However, with its semiconductor-based RF components and its prime position within the signal chain, the downconverter module is, according to Friis [12], one of the most influential modules regarding resolution and therefore a good starting point for improvements. Considering the constraints given by state-of-the-art electronics, the achievable phase noise performance of the detector in the LLRF-system at the EuXFEL is currently $-147\,\mathrm{dBc/Hz}$ for white phase noise at a carrier offset of 1 MHz with a timing jitter of 6 fs within a measurement band from 10 Hz to 1 MHz.

Not only the free-electron lasers FLASH and EuXFEL rely on an LLRF-system based on down-conversion. Similar LLRF-systems are spread across the world

at SACLA in Japan, SwissFEL in Switzerland, and LCLS in the United States of America, to name only a few [13]–[15]. Nevertheless, they all share the two main problematic noise sources (downconverter and ADC noise) and thereby their fundamental limitations.

There are different options applicable for increasing the resolution of the LLRF-system. For instance, one could increase the signal input power to enlarge the signal-to-noise ratio (SNR). But as most of the RF components are limited in input signal power, major parts of the RF distribution would need to be adapted and extremely low-noise RF downconversion and signal processing systems would have to be developed, while the ADC bottleneck remains.

This work, in contrast, considers the enhancement of the noise performance without the necessity of re-designing and modifying the existing core components of the LLRF-system. A good starting point is found in the field detection by downconverting the RF signal to an intermediate or baseband frequency, as this is a common tool for phase-noise detection. Optimized versions of this fundamental approach in terms of phase- and amplitude-detection of RF signals can in principle be found in literature. A carrier-less noise detection scheme was already proposed in the year 1968 [16], [17], but to the best of the author's knowledge, it has not been successfully applied in accelerator facilities to date. Labaar et al. [18] improved the classical frequency discriminator phase-noise testing by applying the carrier suppression technique in the 1980's and improved the robustness against leaking amplitude noise. In the 2000's, Ivanov and Rubiola [19]–[22] independently began to build such a system for studying the stability and purity of amplifiers and oscillators, achieving impressive results. Within the accelerator research community, based on earlier results, colleagues at Argonne National Laboratory, USA, also applied the principle and showed in a laboratory-based prototype how a possible realization in the accelerator context might look like [23], [24]. At a carrier frequency of 2.815 GHz very promising phase detection results with $-176\,\mathrm{dBc/Hz}$ at a 10 kHz offset were obtained. However, an actual system application was never published. This is the point where this work picks up.

After a proof-of-principle within the course of a master's thesis [25] and first promising results on a mechanical breadboard setup, the presented work was able to emphasize the potentials of the proposed method in the context of accelerator controls. For the first time, the field detection range of the LLRF-system for RF cavities at DESY was enlarged to a white phase noise floor of $-175\,\mathrm{dBc/Hz}$ at an offset frequency of 1 MHz for a fundamental frequency of 1.3 GHz and an integrated timing jitter of below 100 as for the control bandwidth of 20 kHz.

1.2 Outline of this Thesis

The introductory section is followed by a review of the most important noise definitions and related terminology considered during the investigation. The introduction of phase noise measurement techniques is discussed subsequently, followed by the core of this work - the carrier-less measurement technique. Chapter 3 describes how this measurement setup is realized, what difficulties had to be solved and discusses the results achieved by applying this method to the LLRF-system. Based on this, Chapter 4 discusses the application of the setup as a noise analyzer in the laboratory and in the accelerator control loop. This also includes the extensive noise investigation of RF components necessary for the compactification and automation of the measurement setup. A concluding section wraps up the developments and discusses ideas for future work.

2 Fundamentals of Phase and Amplitude Noise

This chapter outlines the physical relations and metrics as a background to the investigations within this thesis. After starting with an introduction to amplitude- and phase-noise processes, measurement techniques and more advanced terms of noise measurements are presented.

2.1 Definitions and Metrics

In the following, the definition and the description of phase and amplitude noise, as well as noise specific terms and associated metrics are outlined.

2.1.1 Amplitude and Phase Noise

Statistically distributed fluctuations in the amplitude and phase of time-domain signals are referred to as amplitude and phase noise, respectively. The underlying noise processes can come from a large variety of possible influences: non-linear modulations within electronic components, mechanical disturbances (i.e., vibrations, stress effects), or even the flow of current in inhomogeneous materials, to mention only a few. Section 2.1.2 introduces noise processes in more detail. As it is the case for most noisy signals, amplitude and phase noise can lead to errors in the signal processing and further unwanted uncertainties.

Usually, phase and amplitude noise occur simultaneously and are then linked to each other. Superposition of both noise types is the consequence. Figure 2.1 shows the dependencies in the time domain and correspondingly in equivalent vector diagrams in the complex plane.

Phase noise is commonly defined as a measurand in dependence on the power of the evaluated signal [26]. The historic, nowadays obsolete definition of phase noise as the relationship between the noise within a 1 Hz bandwidth at a certain

(a) Superposition of phase and amplitude noise as phasors.

(b) Phasor constellation for a noise-afflicted signal.

Figure 2.1: Noise as vector diagrams in the complex plane.

frequency offset and the amplitude of the carrier signal is additionally explained in Appendix A.1.

In general, a noisy time domain signal $v(t)$ can be exemplified by the additive superposition of an ideal signal at an angular frequency $\omega_0 = 2\pi f_0$ and a comparably small stochastic noise signal $n(t)$ of arbitrary distribution via

$$v(t) = V_0 \cos(\omega_0 t + \varphi_0) + n(t). \tag{2.1}$$

V_0 denotes the amplitude of the signal and φ_0 is an arbitrary constant phase value. As depicted in Figure 2.1, amplitude and phase noise are fluctuations in amplitude and phase, respectively, and can therefore be represented by adding time-dependent amplitude and phase terms.

Analytically, the superimposed signal in the time domain at the fundamental frequency ω_0 can then be expressed using the example of a voltage oscillation as

$$v(t) = V_0 \left(1 + \alpha\left(t\right)\right) \cos\left(\omega_0 t + \varphi_0 + \varphi\left(t\right)\right). \tag{2.2}$$

Here $1 + \alpha\left(t\right)$ denotes a time-varying amplitude factor of the signal and $\varphi\left(t\right)$ the equivalent for the phase component of the signal [27]. The signal can now be represented in complex notation as

$$v(t) = \mathrm{Re}\left[V_0(1 + \alpha(t))e^{j(\omega_0 t + \varphi_0 + \varphi(t))}\right]. \tag{2.3}$$

Assuming a very small phase noise component $\varphi(t)$, the expression can be simplified via

$$e^{j\varphi(t)} = \cos(\varphi(t)) + j\sin(\varphi(t)) \approx 1 + j\varphi(t). \tag{2.4}$$

Furthermore, as both $\alpha(t)$ and $\varphi(t)$ can be assumed to be small, the product of the amplitude and phase noise components is negligible and thus $\alpha(t) \cdot \varphi(t) \approx 0$ holds. Following equations (2.3) and (2.4), $v(t)$ can be represented as

$$v(t) = \mathrm{Re}\left[V_0(1 + \alpha(t) + j\varphi(t))e^{j(\omega_0 t + \varphi_0)}\right], \tag{2.5}$$

where the carrier signal and noise quantities are expressed in a more separated manner. The ideal carrier signal is then represented by

$$\underline{v}_{\text{ideal}} = V_0 \cdot e^{j(\omega_0 t + \varphi_0)}. \tag{2.6}$$

The respective noise quantities are expressed by

$$\alpha(t) = \frac{1}{2}\left(\underline{\alpha}(t)e^{j\omega t} + \underline{\alpha}^*(t)e^{-j\omega t}\right) \tag{2.7}$$

and

$$\varphi(t) = \frac{1}{2}\left(\underline{\varphi}(t)e^{j\omega t} + \underline{\varphi}^*(t)e^{-j\omega t}\right). \tag{2.8}$$

Applying these substitutions to equation (2.5), one obtains the expression

$$v(t) = \text{Re}\left[\frac{\underline{v}_{\text{ideal}}}{2}\left(1 + \underline{\alpha}(t)e^{j\omega t} + \underline{\alpha}^*(t)e^{-j\omega t} + j\underline{\varphi}(t)e^{j\omega t} + j\underline{\varphi}^*(t)e^{-j\omega t}\right)\right] \tag{2.9}$$

$$= \text{Re}\left[\frac{\underline{v}_{\text{ideal}}}{2}\left(1 + e^{j\omega t}\left(\underline{\alpha}(t) + j\underline{\varphi}(t)\right) + e^{-j\omega t}\left(\underline{\alpha}^*(t) + j\underline{\varphi}^*(t)\right)\right)\right]. \tag{2.10}$$

Here, the terms $e^{j\omega t}$ and $e^{-j\omega t}$ indicate components shifted in frequency to $\omega_0 + \omega$ and $\omega_0 - \omega$, the upper and lower sideband components, respectively. Following the sideband representation, the individual voltage terms in time domain can be considered in the frequency domain via a Fourier transformation $\mathcal{F}\{v(t)\}$ as spectral densities with

$$S_v(f) = \lim_{T\to\infty} \frac{1}{T}\left|\mathcal{F}\{v(t)\}\right|^2. \tag{2.11}$$

Thus, with equation (2.10) and $f_m = f \pm f_0$ it follows for both sidebands

$$S_v(f_m) = A_0^2\left[\delta(f_m) + S_\alpha(f_m) + S_\varphi(f_m) + O^n\left(S_\alpha(f_m), S_\varphi(f_m)\right)\right], \tag{2.12}$$

where $O^n\left(S_\alpha(f \pm f_0), S_\varphi(f \pm f_0)\right)$ accounts for the higher-order mixing terms. The carrier signal itself is represented by a Dirac pulse $\delta(f_m)$ at frequency f_m, the amplitude noise by the density component $S_\alpha(f_m)$, and the phase noise likewise by $S_\varphi(f_m)$.

The time equivalent of the phase in seconds can be defined as

$$x(t) = \frac{\varphi(t)}{\omega_0} = \frac{\varphi(t)}{2\pi f_0}. \tag{2.13}$$

Furthermore, the frequency fluctuation can be described as the first derivative of the time domain phase fluctuation with

$$y(t) = \dot{x}(t) = \frac{\dot{\varphi}(t)}{\omega_0} = \frac{2\pi\Delta f(t)}{2\pi f_0}. \tag{2.14}$$

The phase noise present due to a randomly varying phase in the system can now be determined by the two-sideband spectral power density $S_\varphi(f)\left[\frac{\text{rad}^2}{\text{Hz}}\right]$, which is obtained by Fourier transforming the autocorrelation function of $\varphi(t)$. For the consideration of the frequency noise or phase noise with respect to time, Appendix A.2 shows the relationships analogously.

In practice, the power density spectrum is given as $\mathcal{L}(f)$ in dBc/Hz, defined as

$$\mathcal{L}(f) = \frac{1}{2} S_\varphi(f), \tag{2.15}$$

and is only valid in relation to the absolute carrier power. Even though this relationship is a redundant definition, typical commercial phase noise measurement systems preferably refer to $\mathcal{L}(f)$ instead of $S_\varphi(f)$.

2.1.2 Noise Power Law

The noise power density spectrum $S_\varphi(f)$ consists of various separable sections of power and frequency components. The resulting spectrum is the sum of all individual noise processes and can be calculated by the power law

$$S_\varphi(f) = \sum_{i=-\infty}^{0} b_i f^i. \tag{2.16}$$

Each summand represents an independent noise sideband. In principle, the index i goes from negative infinity to zero. In practice, due to reasons of convergence and simplicity the index is only considered down to values of $i = -4$. Table 2.1 shows the classification and the commonly used descriptive terms of the individual noise contributions starting from $i = -4$.

The relationship between the spectral quantities $S_\varphi(f)$ is descriptively displayed in the Appendix A.2 in Figure A.2(a). The coefficients b_i define the weighting factor of the respective noise components. b_0 thus indicates the white noise component.

The umbrella term 1/f-noise collects a variety of processes contributing to noise of this general type, which can be found in various electrical components, e.g., frequency mixers, amplifiers or ADCs.

One can briefly assign the 1/f-noise terms to categories of devices: Contact noise is closely connected to diodes, transistors and semiconductor-based devices in general, and is a phenomenon in atomic order and the lattice structures of materials [28]–[32]. It occurs for instance whenever current flow passes through inhomogeneous material structures. Generation-recombination noise for instance appears in pn-junctions by carrier movement even without external biasing of the

Frequency characteristic	Common denotation
f^0	white phase noise
f^{-1}	$\frac{1}{f}$-noise, pink noise, flicker phase noise
f^{-2}	Brownian phase noise, red noise, random walk of phase (white frequency noise)
f^{-3}	flicker frequency noise
f^{-4}	Brownian frequency noise, random walk of frequency

Table 2.1: Classification of $f^{-\alpha}$ type noise.

component [33]. Shot noise is introduced as well by currents passing a potential barrier, e.g., the diode current over a pn-junction, but acts independently of the offset frequency and thus is white noise. The term flicker noise is regularly found in the microwave tube context and excess noise is typically used for resistive devices and structures [34], [35].

Additionally, thermal noise is always present, if the network impedance's real part is different from zero, but as it generally adds to all frequencies it is considered white noise [36]. An extensive summary on 1/f-noise is given in [37], [38].

If one wants to consider the noise power independently of a discrete frequency the derivation takes place via the approach of the black-body radiation with

$$S(f) = \frac{hf}{e^{hf/k_\mathrm{B}T} - 1} \approx k_\mathrm{B}T = N_\mathrm{T} \quad \text{for } hf \ll k_\mathrm{B}T, \tag{2.17}$$

where $h = 6.026 \times 10^{-34}$ Js is Planck's constant, $k_\mathrm{B} = 1.38 \times 10^{-23}\ \frac{\mathrm{J}}{\mathrm{K}}$ is Boltzmann's constant and T is the absolute ambient temperature in Kelvin [27]. Considered within a bandwidth B, the noise power can be given as

$$P_\mathrm{n} = N_\mathrm{T}B = k_\mathrm{B}TB, \tag{2.18}$$

where T corresponds to the noise temperature.

An additional approach to spectral noise analysis, which has no application in the scope of this presented work, is the inspection of the time domain signal itself. This can be achieved by the evaluation of the variance of the measured signal. This tool is known as the Allan variance and is additionally explained in Appendix A.3.

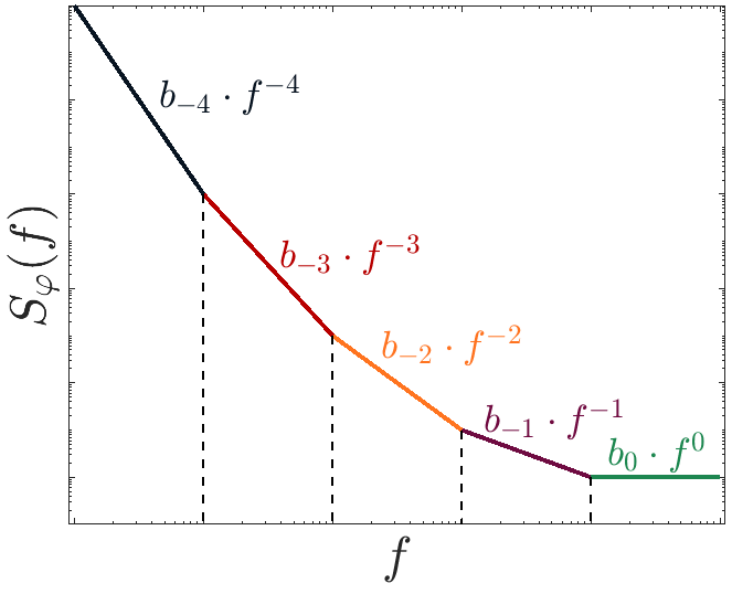

Figure 2.2: Illustration of the power laws of phase and frequency noise over frequency.

2.1.3 Time Jitter

In order to make quantitative statements about the properties of a phase noise spectrum, not only the measured spectrum is of interest, but also related quantities such as the so-called jitter in time, phase, and frequency, as well as properties of the considered measurement equipment.

The term jitter in this context refers to the amount of jittering, of, for example in phase, excited by noise processes. The smaller the jitter, the more stable the measurement signal is in its own fundamental phase. The jitter represents short-term processes, whereas the similar looking effect of drifting, which is mostly caused by temperature changes and mechanical instabilities, regards long-term processes and is only visible for observations over long periods and is to be distinguished from the jitter. As shown in Equation (2.19), the jitter averaged in time can be accumulated according to Parseval's theorem [39] from the cross-correlation spectrum $S_x(f)$ over a specified frequency range $[f_1, f_2]$ with

$$\overline{\Delta t^2_{f_1,f_2}} = \frac{1}{(2\pi f_0)^2} \int_{f_1}^{f_2} S_\varphi(f)\,\mathrm{d}f. \tag{2.19}$$

Commonly, this range is limited by the carrier frequency $f_1 = f_0$ (lower limit) and the technologically possible distance to the carrier frequency f_2 (upper limit) [40],

[41], [42]. Analogously, the phase jitter results in

$$\overline{\Delta\varphi^2_{f_1,f_2}} = \int_{f_1}^{f_2} S_\varphi(f)\,\mathrm{d}f. \tag{2.20}$$

Common terms of this fluctuation of the signal over time are also clock jitter, timing jitter or time jitter. For the following sections a slight variation of the time jitter definition is used with

$$t_{\mathrm{RMS}} = \frac{1}{2\pi f_0}\sqrt{2\int_{f_1}^{f_2} \mathcal{L}(f)\,\mathrm{d}f}. \tag{2.21}$$

This modification is commonly used in the LLRF environment as a figure of merit for system stability. All stated jitter values in this thesis are based on the root mean square (RMS) timing jitter in Equation (2.21).

2.1.4 Noise Figure

The noise performance of a device is commonly expressed by the so-called noise figure. This concluding term is useful in many cases, but not always sufficient as it does not distinguish between individual noise components but represents the overall noise performance. With respect to Section 2.1, a typical application of the equivalent noise temperature is the calculation of the noise figure, which is an important parameter for the selection of, e.g., amplifiers in a communication system. The noise figure of a component is defined as the ratio between the SNR at its input and the SNR at the output by

$$F = \frac{\mathrm{SNR}_{\mathrm{input}}}{\mathrm{SNR}_{\mathrm{output}}} = \frac{N_{\mathrm{e}}}{k_{\mathrm{B}}T_0}, \tag{2.22}$$

where the equivalent noise spectrum N_{e} includes the full noise power in the device to be evaluated for matched input ports at $T_0 = 290\,\mathrm{K}$ [43]. For a rough selection of components this might be useful information, but in practice the noise figure F is not sufficient when the interest is in low phase and amplitude noise. Nevertheless, if an amplifier is part of the noise measurement setup, the corresponding noise figure needs to be regarded in the resulting spectrum $\mathcal{L}(f)$.

For multi-stage devices like, e.g., receivers, the system noise figure can be derived by Friis' formula [12]. Assuming a system of k stages, the total noise figure is

$$F_{\mathrm{total}} = F_1 + \frac{F_2 - 1}{G_1} + \frac{F_3 - 1}{G_1 \cdot G_2} + \cdots + \frac{F_k - 1}{G_1 \cdot G_2 \cdot G_3 \cdots G_{k-1}}, \tag{2.23}$$

where F_k and G_k are the noise figure and the power gain of stage k, respectively. Following this relationship, the first stage in a cascaded device structure is the most important and fundamental stage for the total noise figure. In combination with a high power gain in stage $k = 1$, the influence of the second stage is drastically reduced. In the scope of low-noise receiver development, the first stage is therefore the most significant stage concerning its noise figure and power gain.

2.1.5 Conversion Ratio

Typically, every commercial measurement device is already calibrated for system factors when handed out to the customer. Within specific measurement systems a wide variety of these system quantities can be measured and defined. For phase noise measurements, one of these quantities is the so-called conversion factor, which indicates the systems sensitivity. In this case, the conversion ratio from a voltage change to a phase change is of main interest. Especially for baseband measurements, this ratio needs to be considered as a calibration unit in the calculation of $\mathcal{L}(f)$, which is described in subsequent chapters. If a small change in the phase of the signal causes a large deflection of the output voltage of the measurement setup, the system's sensitivity to changes in the phase is very high and even the smallest noise signals can be detected. In general, the conversion ratio k_φ is defined as

$$k_\varphi = \sqrt{\frac{S_V(f)}{S_\varphi(f)}} \left[\frac{\mathrm{V}}{\mathrm{rad}}\right] \tag{2.24}$$

and plays a major role in noise measurement schemes based on frequency mixers.

2.2 Measurement Techniques for Phase- and Amplitude-Noise

The detection of phase and amplitude noise is a crucial factor of the measurement and control systems at DESY. In principle, the better the phase and amplitude noise is identified, the better the control system can control the accelerating electric field inside, the better the resulting beam quality is.
This section outlines the most common techniques for the measurement of phase or else amplitude noise. The preferred measurement procedure depends on the application and the required precision [8]. While spectrum analyzers and frequency counters are mainly used for larger phase noise effects and direct measurement methods, more sensitive noise effects can be detected by carrier-nulling, so-called

indirect measurement methods, for instance, using a frequency mixer as a phase detector [26], [44]. As this thesis treats extremely small noise powers, mainly indirect measurement procedures are considered in detail. At the same time, measurement techniques can be distinguished between absolute noise measurements and residual (otherwise known as additive) noise measurements. Absolute measurements include all noise sources within the evaluated signal chain. Residual measurements allow to evaluate single components in the signal chain by exclusion of the external noise sources, e.g., the source signal.

2.2.1 Phase Detector Method

The phase detector method, also known as the saturated mixer method or phase discriminator method, is used for noise analysis in the baseband and is an indirect, residual measurement procedure. The noise of the device under test (DUT) is converted down to the baseband using a frequency mixer, as shown in Figure 2.3. As the local oscillator (LO) frequency is the same as the RF signal, the main carrier is reduced and shifted to other harmonics, but the sidebands differ [26]. Ideally, the noise from the signal source vanishes. The process of downconversion is depicted in

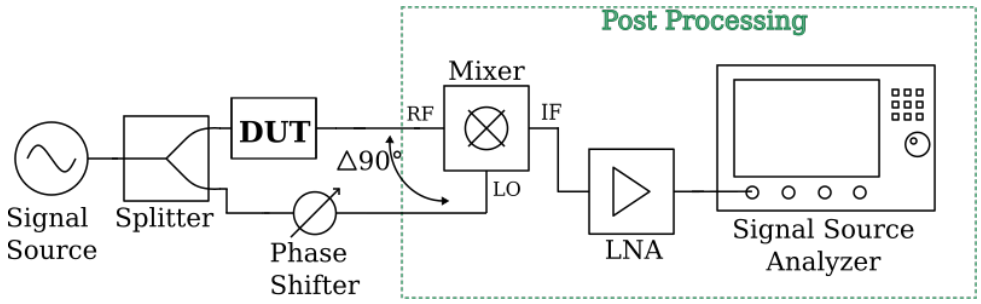

Figure 2.3: Block diagram for the saturated mixer measurement setup.

Figure 2.4 assuming an ideal source signal and simplified noise sidebands of the DUT. This operation is very broadband and only limited by the mixer characteristics.

In order to distinguish amplitude noise from phase noise, the phase difference between the signals at the RF and the LO port has to be either 0° or 90°, respectively. During the mixing process this so-called quadrature condition ideally limits the amplitude noise for 90°-adjustment and the phase noise for 0°-adjustment. In practice a rejection between amplitude noise (AN) and phase noise (PN) of roughly

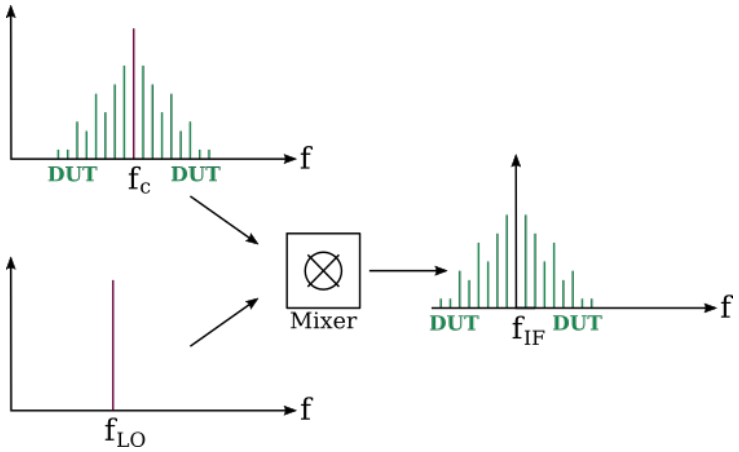

Figure 2.4: Sketch of the ideal downconversion process in the frequency mixer.

30 dB is achievable [45]. Consequently, the phase difference of 90° between the mixer input ports as required for phase noise measurements is obtained by a phase shifter in the LO path. A deviation from the ideal quadrature leads to a mixture of amplitude and phase noise. As the frequency mixer acts as a converter from phase or amplitude fluctuations in RF to voltage fluctuations in direct current (DC) at the IF port, the quadrature condition can be cross-checked by the measurement of the voltage swing at the IF port. For phase noise measurements the voltage should be at minimum, for amplitude noise measurements at maximum, respectively. As the frequency mixer is now part of the detection chain, the conversion factor of the mixer has to be considered in the evaluation of the resulting baseband spectrum. The conversion factor in this case describes the sensitivity of the mixer regarding phase and voltage fluctuations and is commonly defined for this method as the slope of the voltage swing at the zero-crossing by

$$k_\varphi = \frac{\Delta v(t)}{\Delta \varphi(t)}, \tag{2.25}$$

while the 90°-condition holds, analogously to Section 2.1.5. A low-pass filter can be used to eliminate appearing higher order harmonics. In addition, the low noise amplifier (LNA) placed between the mixer and the spectrum analyzer has to be considered in the resulting spectrum. According to Friis formula, the internal noise of the spectrum analyzer is of lesser importance than the noise introduced by the LNA in front [12], [46]. The noise spectrum observed with this method is commonly dominated by the RF mixer noise, especially in the 1/f-noise region close to the carrier frequency. For very low noise signals this is a significant drawback, as the

actual DUT-noise might be covered by the noise of the mixer. The noise behavior of the LNA is of secondary importance for phase detector based measurements.

The phase detector method is sensitive against drifting processes in the signals, as they can lead to deviations from the quadrature condition. Nowadays, the usage of a phase-locked loop (PLL) with a small control bandwidth is common to indirectly stabilize the source signals against such drifts.

This method is the most commonly used procedure to measure phase and amplitude noise and is also the most commonly implemented method for commercial signal source analyzers found in most laboratories. A comparative plot of the most common noise measurement devices is presented in Section 4.1.

2.2.2 Frequency Detector Method

The frequency detector method, also referred to as frequency discriminator or delay line discriminator, can be seen as an extension of the phase detector method and is preferably used to evaluate the frequency noise of a source signal [26], [44], [47]. Besides the phase shifter in Figure 2.3 a delay line introducing a certain time shift τ_d is placed in the same signal path. The delay in time introduces a shift in the phase of the signal. By comparing the nominal signal with the delayed signal, frequency shifts Δf_c in the source signal can be identified [48]. In analogy to the phase detector, the phase difference is converted to a voltage difference, which then can be evaluated in the baseband with a spectrum analyzer. The system's sensitivity depends on the conversion factor k_φ of the phase detector and the chosen measurement offset frequency δf with

$$k_f = k_\varphi \cdot 2\pi\tau_d \cdot \frac{\sin(\pi\delta f\tau_d)}{\pi\delta f\tau_d}. \tag{2.26}$$

Depending on the evaluated offset frequency δf, corrective factors might be necessary for valid measurement results, as k_f is frequency-dependent. Commonly, measurements with offset frequencies up to

$$\delta f = \frac{1}{2\pi\tau_d} \tag{2.27}$$

are valid without corrections for frequency dependency.

2.2.3 IQ-Demodulation and non-IQ-Detection

The in-phase/quadrature (IQ)-demodulation offers the possibility to decompose the RF signal of interest into its in-phase (I) and quadrature (Q) components, which

then can be used to distinguish between phase and amplitude information of the RF signal. Figure 2.5 shows the basic schematic of an analog IQ-demodulator.

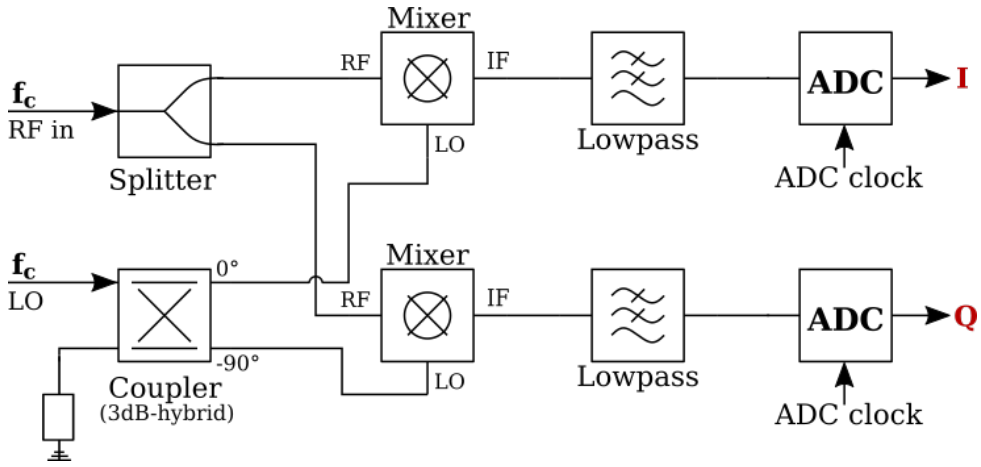

Figure 2.5: Block diagram for analog IQ-demodulation.

The signal of interest at frequency f_c is split into two paths both heading towards a frequency mixer. The LO signal passes through a hybrid coupler, such that one path is delayed in phase by a quarter wavelength compared to the other path. The two resulting LO signals are now 90° apart. After the mixing process with the DUT signal and low-pass filtering, the baseband signals are directly detected by an ADC. The procedure results in signal components in-phase and in quadrature at the same time for each sample [49]. The sinusoidal signal

$$y_{\mathrm{IQ}}(t) = A \cdot \sin(\omega t + \varphi), \tag{2.28}$$

with amplitude A, angular frequency ω and the phase term φ is decomposed into

$$y_{\mathrm{IQ}}(t) = \underbrace{A \cdot \cos(\varphi)}_{I} \cdot \sin(\omega t) + \underbrace{A \cdot \sin(\varphi)}_{Q} \cdot \cos(\omega t) = I \sin(\omega t) + Q \cos(\omega t), \tag{2.29}$$

with the in-phase component $I = A \cdot \cos(\varphi)$ and the quadrature component $Q = A \cdot \sin(\varphi)$. The interest is in the amplitude and phase information, which are connected by

$$A = \sqrt{I^2 + Q^2} \quad \text{and} \quad \varphi = \arctan\left(\frac{Q}{I}\right). \tag{2.30}$$

Drawbacks of the analog implementation of the demodulation are possible additional disturbances due to imperfections in the coupler structures and the RF mixers [11].

To overcome often occurring baseband disturbances from environmental noise, the downconversion with $f_{\mathrm{RF}} \neq f_{\mathrm{LO}}$ is to be preferred, instead of downconverting with $f_{\mathrm{RF}} = f_{\mathrm{LO}}$ [50].

The demodulation can also be performed digitally in an ADC after analog downconversion of the RF signal. For the classical IQ-demodulation, the sampling frequency of the ADC is set to a quarter of the operating frequency, which allows to take a sample each quarter period [51].

In case of unwanted excitation of higher-order odd harmonics due to non-linearities in the setup's components, this demodulation scheme can lead to faulty detection. This is due to the fact that with only four sampling points per period it is not possible to distinguish between these harmonics and the carrier signal. Especially for the LLRF field control system, the error would be too high for proper field trace-back.

In contrast, the non-IQ-detection aims for higher linearity by lower error rates. The signals to be detected are non-IQ demodulated, which refers to a demodulation scheme deviating from quadrature detection with its sampling frequency $f_{\mathrm{sampling}} = 4f_{\mathrm{IF}}$, as sketched in Figure 2.6. Here, the samples for $f_{\mathrm{sampling}} = 4f_{\mathrm{IF}}$ are marked in

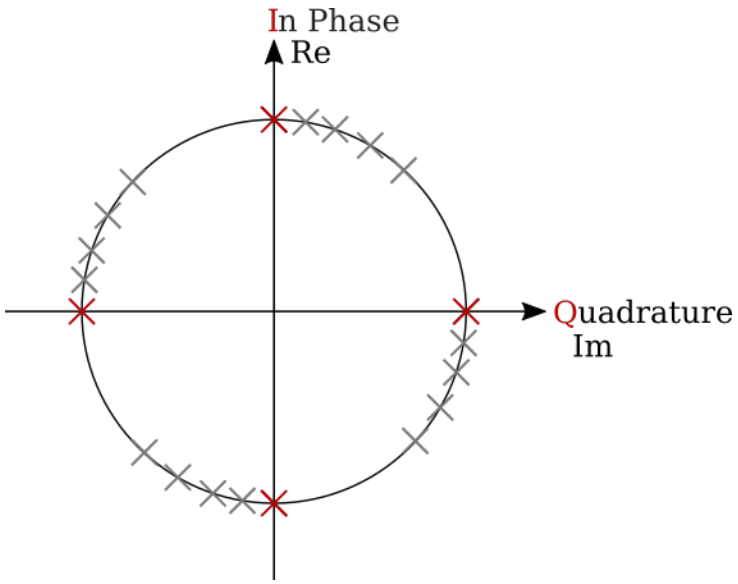

Figure 2.6: Illustration of the IQ detected signal and the relationship to the complex plane. The IQ demodulation points are marked in red, the non-IQ sampling points exemplarily in grey.

red, the non-IQ-detected samples are indicated as gray markers. Depending on the type of ADC used for signal processing, the sampling frequency can be extended to higher numbers. Still, not all sampling frequency choices are advantageous and applicable to accelerator control systems [52]. For the proper detection of the accelerating field, the digital signal must not only be of high resolution, linearity and repeatability are likewise of importance. A well working demodulation scheme is for example achieved with a sampling frequency of $3.75 f_{\mathrm{IF}}$. For this specific non-IQ-detection scheme, the occurring harmonics do not disturb within the filter range and are not lining up with the system-defined accelerator cavity modes, thus ease the evaluation of the signal of interest. In consequence, the reconstructability of the original signal is less error-prone than with classical IQ-demodulation and leads to a more accurate and robust control of the cavity field [53].

2.2.4 Cross-Correlated Measurements

To enhance the performance of detection systems, cross-correlation techniques can be applied. The benefits of correlation techniques have been known for many decades, e.g., in astronomy and radio-spectrometry. Applications in digital signal detection systems were introduced in the late 20^{th} century [54], [55], [56]. The method allows to reduce the noise contribution stemming from the measurement device itself. To apply the cross-correlation techniques to for instance phase noise measurements of a DUT, one has to introduce two independent measurement channels, both including the same DUT [57], [58]. This can be achieved by a split of the DUT signal feeding both signals through a measurement device, as is shown in Figure 2.7.

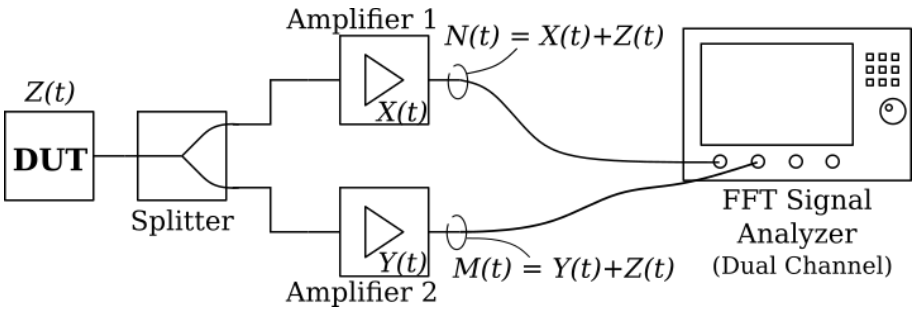

Figure 2.7: Block diagram of a possible cross-correlation phase noise measurement setup.

The DUT induces the noise signal of interest $z(t)$. Two amplifiers add noise contributions to the split DUT signal as well, in the form of $x(t)$ and $y(t)$. As the noise contributions of the amplifiers can be assumed as statistically independent, the cross-correlation of these signals S_{nm}, performed in the Fast Fourier Transform (FFT) analyzer, converges to the expectation $\mathbb{E}\{\cdot\}$ [59] of the autocorrelated signal of the DUT's noise contribution S_{zz}. With the FFTs of the noise signals $X(f), Y(f)$ and $Z(f)$, the latter will be substantiated by the cross-correlation calculation of spectral densities:

$$\begin{aligned}\mathbb{E}\{S_{nm}\} &= \frac{1}{T}\mathbb{E}\{NM^*\} \\ &= \frac{1}{T}\mathbb{E}\{[X+Z]\times[Y+Z]^*\} \\ &= \frac{1}{T}\left[\mathbb{E}\{XY^*\}+\mathbb{E}\{XZ^*\}+\mathbb{E}\{ZY^*\}+\mathbb{E}\{ZZ^*\}\right] \\ &= \frac{1}{T}\mathbb{E}\{ZZ^*\} \\ &= S_{zz}\end{aligned} \tag{2.31}$$

The factor T denotes the measurement time. Due to statistical independence it follows

$$\mathbb{E}\{XY^*\} = \mathbb{E}\{XZ^*\} = \mathbb{E}\{ZY^*\} = 0.$$

For multiple measurements k the expectation $\mathbb{E}\{S_{nm}\}$ can be substituted with

$$\begin{aligned}\langle S_{nm}\rangle_k &= \frac{1}{T}\mathbb{E}\langle NM^*\rangle_k \\ &= S_{zz} + O\left(\sqrt{1/k}\right).\end{aligned} \tag{2.32}$$

The term $O\left(\sqrt{1/k}\right)$ then refers to the remaining error, that decreases with a sufficiently high number of averages k [57]. For a classical DUT characterization two main conditions have to be ensured: The number of samples for the averaging has to be high enough such that $\langle S_{nm}\rangle_k \to \mathbb{E}\{S_{zz}\}$ and the DUT noise needs to be significantly higher than the instrument noise. With this method, several decibels in the noise floor power are gained. Figure 2.8 exemplarily shows the DUT measurement with a commercial FFT analyzer with and without applying a cross-correlation estimation. The factor indicates the number of cross-correlations computed for each frequency decade. In addition, the system integrated cross-correlation optimizer is applied for one curve, denoted with "optimized", to show the benefit of sophisticated signal processing methods. Nevertheless, this is all at the expense of valuable

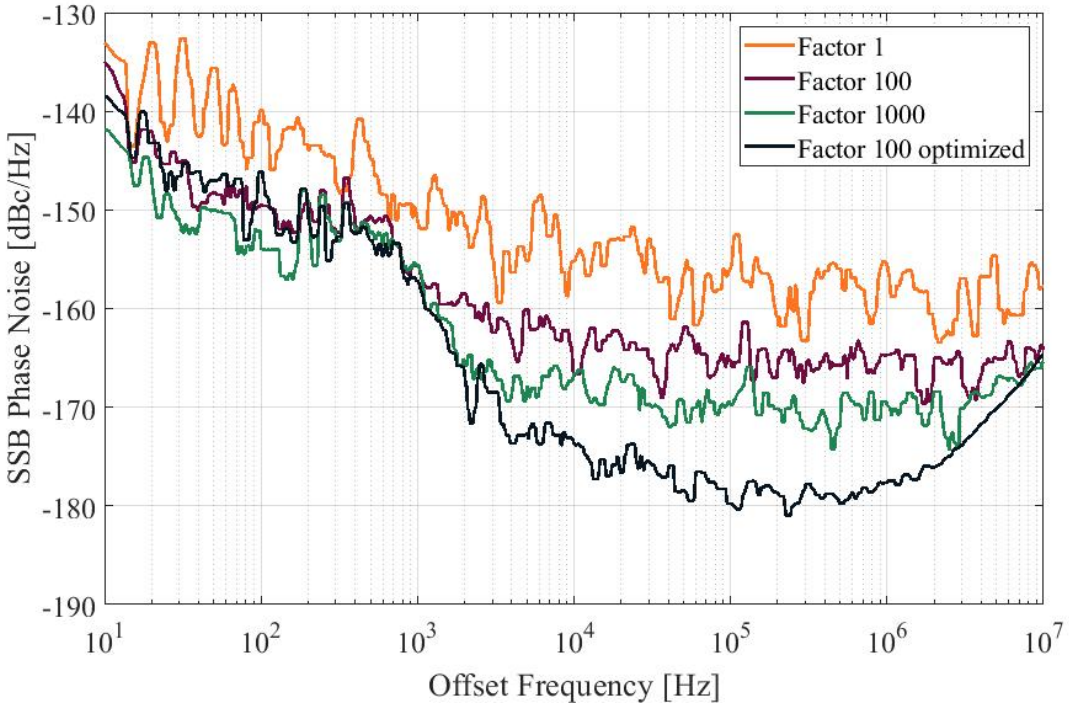

Figure 2.8: Comparison of measuring the same DUT with increasing number of cross-correlations. The DUT is the internal signal source of the measurement device (R&S FWSP [60]) itself.

processing time. Internal cross-talk effects in the device or imperfections of the splitting components can additionally impair the measurement results and constrain the measurement resolution.

2.3 Carrier-Based versus Carrier-Less Measurement Principles

Referring to the main measurement principle of carrier-less noise measurement, which this thesis discusses in detail, one has to emphasize that all so far mentioned noise measurement methods are heavily relying on the knowledge of the main carrier's properties. To be aware of the phase information and the signal power at the carrier frequency helps to keep a fixed reference while measuring. Nevertheless, the carrier-based measurement principles have drawbacks when it comes to the overall noise performance of the measurement system. The main component of carrier-based measurement principles is the frequency mixer, which according to

Friis' formula is in the most critical position. As discussed Section 2.2, the main signal is mixed across a diode down to baseband or an intermediate frequency before the evaluation of the noise sidebands. Having the already noisy main signal converted in the non-linear frequency mixer is the most significant noise contributing factor for these measurement principle types.

Limiting the incident signal power before evaluating the noise sidebands however ensures lower noise contributions from the mixer than compared to normal signal power. This is in fact due to the linear downscaling of noise power with declining signal power. However, only reducing the signal power is not sufficient for the investigation of noise sidebands, as they are scaled down as well. It is important to change the power ratio between the carrier frequency and the noise sidebands. This can be achieved by a carrier-mitigating interferometric system structure, where the reduced carrier power is narrowly band-limited and the noise sidebands remain. Another advantage of such a carrier-less noise measurement is the circumstance that, by placing a structure to destructively interfere with the main carrier signal, the first relevant noise inducing stage, and thus, according to Friis noise formula, the most important for overall noise performance, changes from the mixer diode (or any other post-processing system) to the noise contribution from the inside of the interferometer. These two advantages of decreasing the detector's noise floor and avoiding noise and non-linearities of the RF mixer have already been clear in very early stages of noise evaluation and detection. The first traces to carrier-free measurement experiments have been left in the early second half of the 20th Century [16], [17]. Due to the high complexity of the measurement principle and the noise requirements, such a system was never set up and commercially distributed as a detector front-end nor is it used in particle accelerator environment. There are a few major obstacles, which are outlined in the subsequent chapters.

3 The Carrier Suppression Interferometer at DESY

This chapter describes the structure of the carrier-less measurement setup, introduced in Section 2.3, the Carrier Suppression Interferometer (CSI), and its working principle. Furthermore, the laboratory CSI setup is shown and the measurement routines and challenges related to the experiment are discussed. At the end of this chapter, the resolution limit of the applied setup is assessed and connected observations are highlighted.

The basic principle of the carrier-suppressed measurement is simple, as is sketched in Figure 3.1. The reference signal is split into two paths. One of them passes through the DUT, while the other one is adjusted in phase and amplitude by several actuators to match for interference. Both signals are subsequently recombined. The adjustment in phase and amplitude is set for destructive interference, thus ideally resulting in maximal carrier suppression. After the signal recombination, an LNA follows and amplifies the remaining noise sidebands, which are ideally only introduced by the DUT. By the amplification of the noise sidebands, the dynamic range of the detection is extended and enables a higher detection resolution. The detection system becomes near-completely independent of the LNA's and the post-processing system's noise behavior. By nulling the carrier signal, the subsequent systems are prevented from saturation effects, which is one of the main benefits compared to standard noise detection systems. This opens large improvement possibilities for the control systems of particle accelerators.

Depending on the initial post-processing system's noise floor, the CSI as a front-end extends the overall noise floor by at least the gain of the LNA. This principle is elaborated in the subsequent sections.

3.1 The Laboratory Setup

Starting with a successful prior proof-of-principle [25], a more compact version of the CSI is developed and available for noise characterization of components and

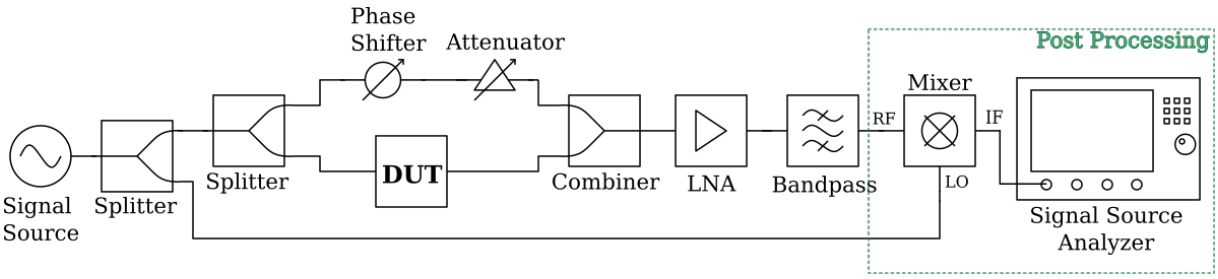

Figure 3.1: Basic block diagram outlining the measurement principle.

devices in the laboratory. The system is optimized for the fundamental frequency of 1.3 GHz given by the geometry of the accelerating cavities at DESY. Figure 3.2 and Figure 3.3 show the development of the carrier suppression system over the last years up to the latest setup. During the process of collecting experience with the CSI a second signal path was introduced to ease maximum suppression. The extended block diagram in Figure 3.4 shows the added signal path. As displayed, it is decoupled from the main signal in the front and recombined in a coupler after the so-called coarse suppression. Within the coarse suppression region, the carrier adjustment is highly sensitive and the actuators have the strongest influence. For the manually adjustable actuators, the suppression is too unstable for proper system operation. Compared to the coarse suppression adjustment, the secondary signal path holds only a small fraction of the main signal power and is therefore used as an additive and less sensitive fine-adjustment of the carrier suppression. In the following, the secondary suppression is referred to as fine suppression. Additionally, new in this block diagram is the calibration unit and the combination of the CSI and the receiver section of the LLRF-system.

Figure 3.5 shows the mechanics of the CSI setup. All elements are mounted on an optical breadboard to ensure mechanical stability, which has shown to be crucial for the reliability and repeatability of the results. The coarse suppression is achieved with a continuous 360° phase shifter and step attenuators. The DUT is also located within the coarse suppression region. To enable comparing the measurement using carrier suppression to the measurement with the existing detector system at DESY, the signal path behind the DUT is split a second time and one branch serves as the reference (REF) measurement signal directly to the post-processing system. After the recombination of the fine suppression path with the coarse suppression path via a coupler, the amplification by the LNA of about 40 dB follows. Due to the carrier suppression, only the remaining noise sidebands are amplified and used for further detection. This allows a higher resolution of the noise processes and a

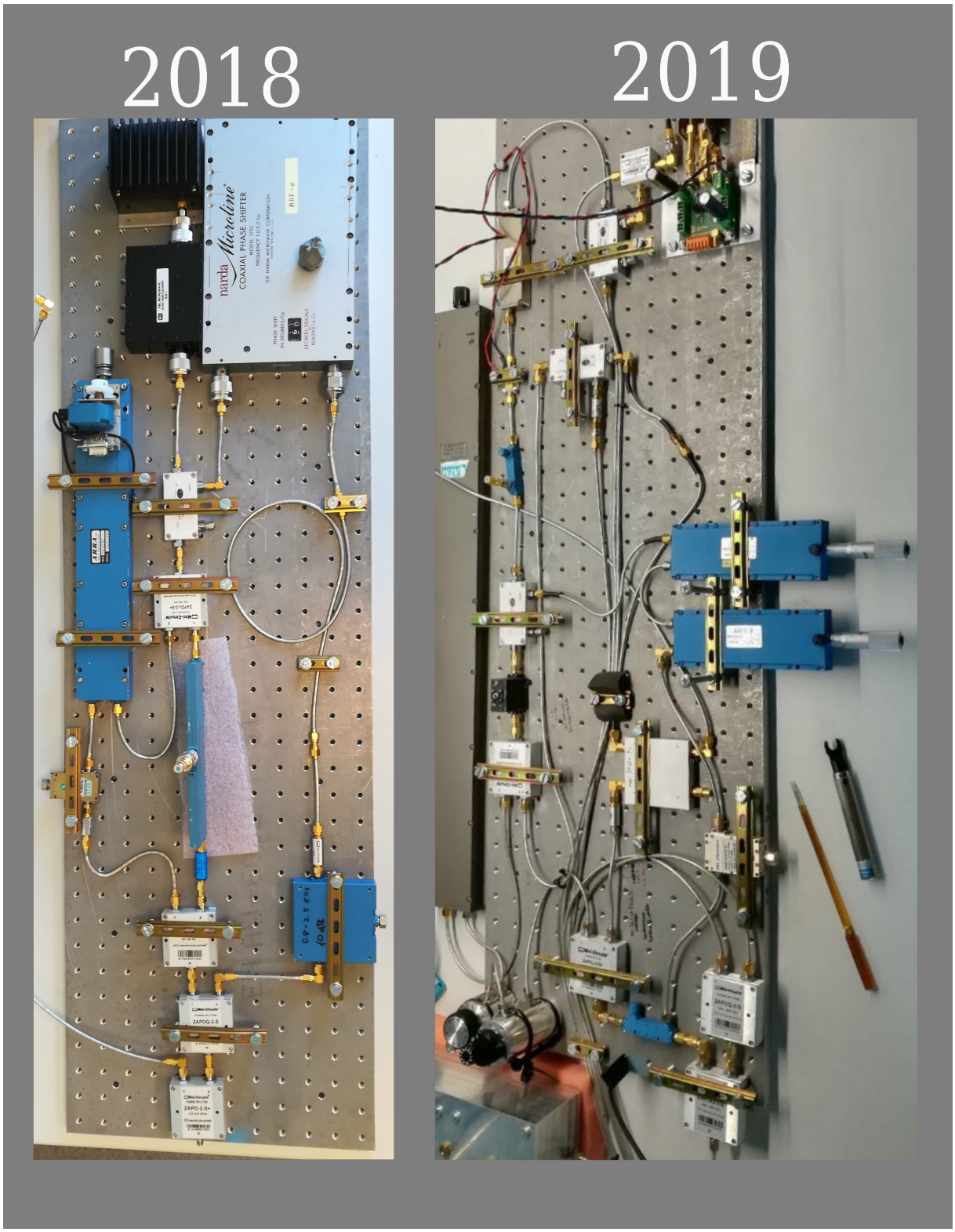

Figure 3.2: CSI evolution from 2018 (left) to 2019 (right).

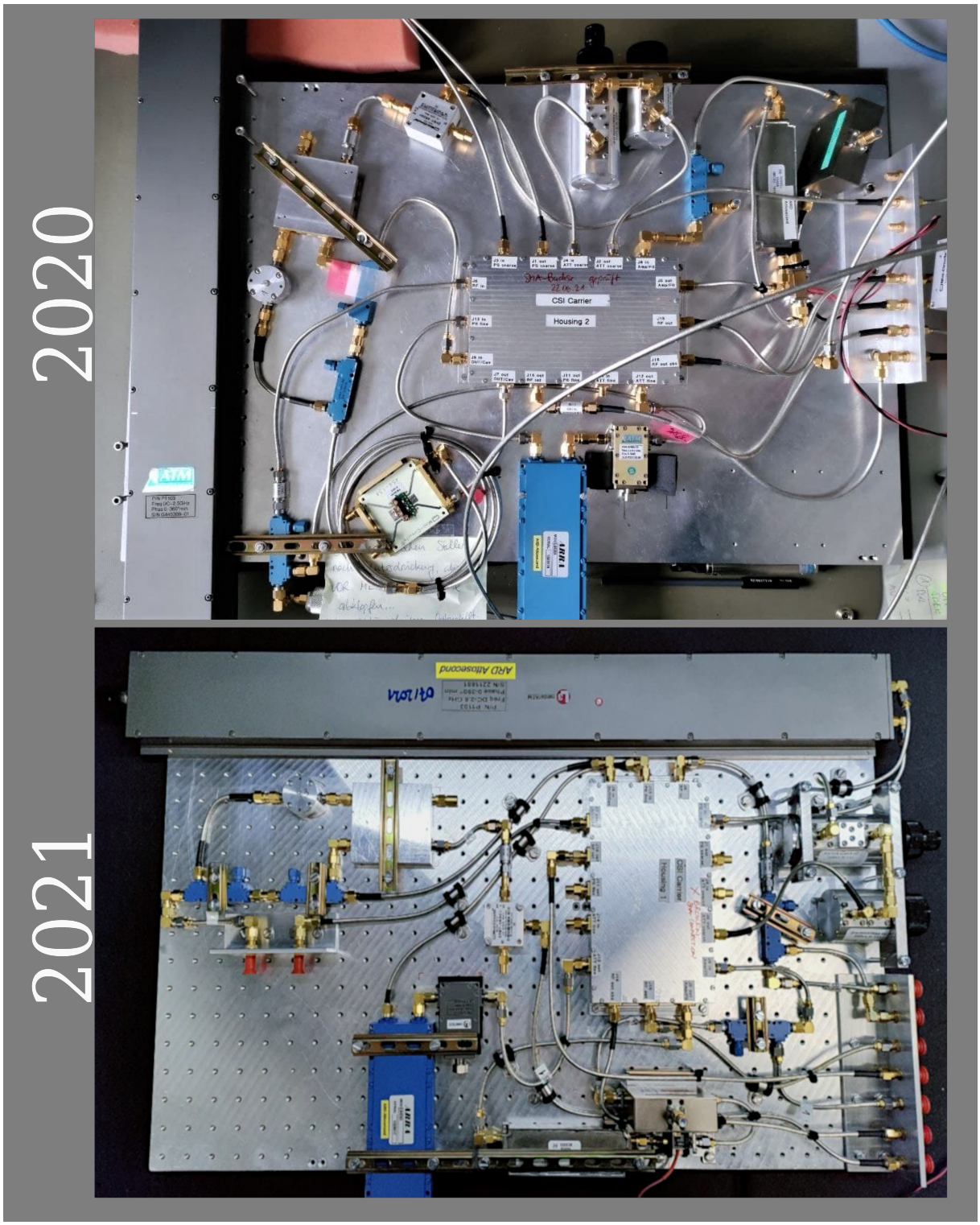

Figure 3.3: CSI evolution from 2020 (top) to 2021 (bottom).

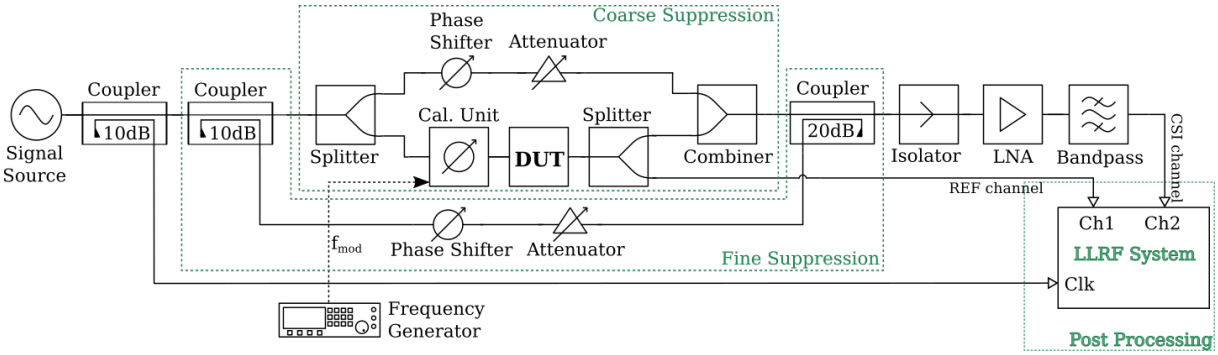

Figure 3.4: Extended block diagram of the measurement setup.

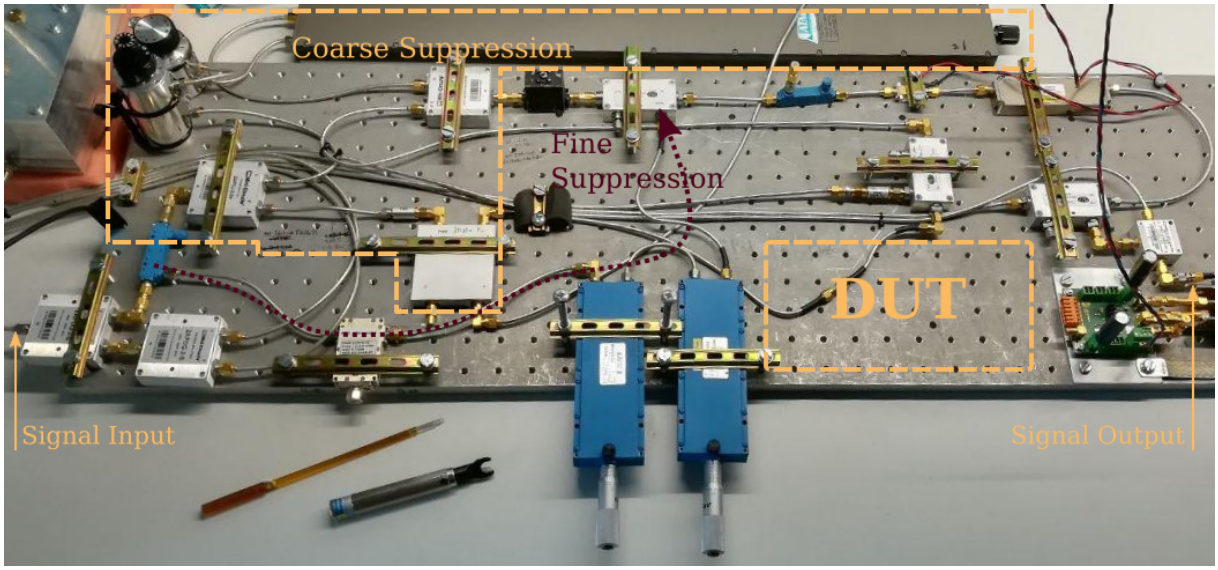

Figure 3.5: The CSI in 2019 with highlighted sections for clarification.

larger margin to the noise floor of the post-processing system. For the calibration, a voltage-controlled phase shifter is inserted in the DUT path. The effect of this phase shifter and the calibration routine are discussed in Section 3.3.

For future accelerator application, further compactification of the CSI setup is mandatory. The process of compressing the CSI to a smaller form factor occurs in a steady trade-off between size and performance. To reduce the size of the setup, it is necessary to swap from mechanical actuators to electronically adjustable devices. Unfortunately, as the electronic devices are mostly based on active semiconductor components and often require dedicated bias and control voltages, both the devices and the power supplies are known to be comparatively noisy and would degrade the performance of the CSI severely. Therefore, the main initial application of the

considered measurement system is the characterization and identification of suitable components.

3.2 Theoretical Description

In the following, fundamental relations between the signals in the CSI as they were presented in the preceding Master's thesis are briefly revisited [19], [21], [25]. Referring to Figure 3.1, the standard system configuration has a sinusoidal local oscillator source signal

$$v_{\mathrm{src}}(t) = V_0 \cos(\omega_0 t), \tag{3.1}$$

which for now is assumed to be noise-free.

Passing through the DUT, the phase noise term $\varphi(t)$ and the amplitude noise term $\alpha(t)$ are added to the source signal, resulting in

$$\begin{aligned} v_{\mathrm{DUT}}(t) &= V_0 \left(1 + \alpha(t)\right) \cos\left(\omega_0 t + \varphi(t)\right) && (3.2)\\ &= V_0 \left(1 + \alpha(t)\right) \left[\cos(\omega_0 t)\cos(\varphi(t)) - \sin(\omega_0 t)\sin(\varphi(t))\right]. && (3.3) \end{aligned}$$

Assuming $\alpha(t)$ and $\varphi(t)$ to be negligible against the signal itself, the expression reduces further to

$$\begin{aligned} v_{\mathrm{DUT}}(t) &= V_0 \left(1 + \alpha(t)\right) \left[\cos(\omega_0 t) - \sin(\omega_0 t)\varphi(t)\right] && (3.4)\\ &= V_0 \left(\cos(\omega_0 t) - \sin(\omega_0 t)\varphi(t) + \cos(\omega_0 t)\alpha(t)\right). && (3.5) \end{aligned}$$

Substituting $n_\alpha(t) = V_0\alpha(t)$ and $n_\varphi(t) = V_0\varphi(t)$ leads to

$$v_{\mathrm{DUT}}(t) = V_0 \cos(\omega_0 t) + n_\alpha(t)\cos(\omega_0 t) - n_\varphi(t)\sin(\omega_0 t). \tag{3.6}$$

Before entering the receiver, the carrier amplitude is mitigated by means of destructive signal interference, resulting in a carrier-less signal

$$v_{\mathrm{sup}}(t) = \left(n_\alpha(t)\cos(\omega_0 t) - n_\varphi(t)\sin(\omega_0 t)\right). \tag{3.7}$$

A following Fourier transform of $v_{\mathrm{sup}}(t)$ leads to the power spectral density

$$S_{\mathrm{sup}}(f) = \left(N_\alpha(f) + N_\varphi(f)\right) \tag{3.8}$$

with $N_\alpha(f)$ and $N_\varphi(f)$ being the power spectral densities of $n_\alpha(t)$ and $n_\varphi(t)$, respectively.

The mixing process redistributes the power components from around frequency f to baseband. This means, that any component at Δf stems from the respective noise components at $f_0 + \Delta f$. The output voltage spectrum follows with:

$$S_{\mathrm{out,V}}(\Delta f) = \left(\underbrace{(N_\alpha(f_0+\Delta f))}_{\propto V_0^2 S_\alpha(\Delta f)} \cos^2(\Delta\varphi) + \underbrace{(N_\varphi(f_0+\Delta f))}_{\propto V_0^2 S_\varphi(\Delta f)} \sin^2(\Delta\varphi) \right) l_\mathrm{s} g_\mathrm{LNA} l_\mathrm{M} R_0 \tag{3.9}$$

$$= \left(S_\alpha(\Delta f)\cos^2(\Delta\varphi) + S_\varphi(\Delta f)\sin^2(\Delta\varphi) \right) V_0^2 l_\mathrm{s} g_\mathrm{LNA} l_\mathrm{M}, \tag{3.10}$$

where l_s and l_M denote the losses within the interferometer and the subsequent down-converting mixer, respectively. R_0 denotes the termination resistance of the mixer output and g_LNA the LNA gain. The phase noise power spectral density in dependence of the frequency offset is expressed via

$$S_\varphi(\Delta f) = \frac{N_\varphi(f_0+\Delta f) R_0}{V_0^2}. \tag{3.11}$$

With fulfilled 90°-condition for phase noise measurements, the output voltage spectrum results in

$$S_{\mathrm{out,V}}(\Delta f) = N_\varphi(f_0+\Delta f) R_0 l_\mathrm{s} g_\mathrm{LNA} l_\mathrm{M}, \tag{3.12}$$

which contains only the phase noise signal components.

This together with Equation 3.11 leads to the output voltage spectrum in frequency domain

$$S_{\mathrm{out,V}}(\Delta f) = S_\varphi(\Delta f) V_0^2 l_\mathrm{s} g_\mathrm{LNA} l_\mathrm{M} \tag{3.13}$$

$$= 2 S_\varphi(\Delta f) R_0 P_0 l_\mathrm{s} g_\mathrm{LNA} l_\mathrm{M}. \tag{3.14}$$

The LNA gain g_LNA and the signal power P_0 after the DUT section are next to the DUT's phase noise $S_\varphi(\Delta f)$ the main noise level influences.

The voltage noise spectrum is connected to the phase noise spectrum $S_\varphi(\Delta f)$ and the power density $S_{\mathrm{out,P}}(\Delta f)$ via

$$S_\varphi(\Delta f) = \frac{S_{\mathrm{out,V}}(\Delta f)}{k_\varphi^2} = \frac{S_{\mathrm{out,P}}(\Delta f)}{k_\varphi}. \tag{3.15}$$

Referring to Section 2.1.5, k_φ denotes the conversion factor of the downconverting frequency mixer of the phase detector, and analogously describes the sensitivity of the CSI measurement setup. As

$$S_{\text{out}}(\Delta f) = S^{\varphi}_{\text{out}}(\Delta f) + S^{\alpha}_{\text{out}}(\Delta f) \tag{3.16}$$

holds, the amplitude noise $S^{\alpha}_{\text{out}}(\Delta f)$ can be determined analogously with k_α instead of k_φ.

For the relationship in time domain

$$v_{\text{out}}(t) = -\frac{1}{2}\, l_{\text{M}}\, g_{\text{LNA}}\, V_0^2\, \varphi(t) \tag{3.17}$$

holds, assuming the signal amplitude remains unchanged while passing the DUT. A low-pass filtering removes all higher order terms and as the noise terms are assumed to be small against the main carrier, a small-angle approximation with respect to the noise quantities φ, α, φ_{src}, and α_{src} with $\cos(\text{x}) \approx 1$ and $\sin(\text{x}) \approx x$ is applied.

Equations 3.14 and 3.17 are only valid for the CSI if the carrier suppression is assumed to be ideal: the DUT introduces no losses, the 90°-condition is perfectly fulfilled and there is no phase imbalance in the suppression region [21], [25].

The following discussion considers these likely occurring imperfections and interprets the consequences as seen in theory. In reference to Figure 3.1, the following signals are defined for this evaluation:

1. the noisy source signal given by

$$v_{\text{src}}(t) = V_0(1 + \alpha_{\text{src}}(t)) \cos(\omega_0 t + \varphi_{\text{src}}(t)) \tag{3.18}$$

   with the phase noise components $\varphi_{\text{src}}(t)$ and amplitude noise component $\alpha_{\text{src}}(t)$, and

2. the output signal of the DUT

$$v_{\text{DUT}}(t) = V_{\text{DUT}} \cdot (1 + \alpha_{\text{src}}(t) + \alpha(t)) \cdot \cos(\omega_0 t + \varphi_{\text{src}}(t) + \varphi(t)). \tag{3.19}$$

The remaining components (e.g., splitter, phase shifter) between signal input to the point of suppression are assumed to be ideally noise-free and symmetrical. It follows an imperfect signal subtraction represented by the factor p to simulate the non-ideal carrier suppression, resulting in a signal v_{sup} with

$$v_{\text{sup}}(t) = v_{\text{DUT}}(t) - p \cdot v_{\text{src}}(t). \tag{3.20}$$

The resulting signal $v_{\mathrm{sup}}(t)$ enters the mixer. In order to maintain the aforementioned 90°-condition between RF and LO port of the mixer, which is necessary for the phase noise detection, the signal is shifted by a phase of $\frac{\pi}{2}$ to

$$v_{\mathrm{LO,\ 90^\circ}}(t) = V_0 \cdot (1 + \alpha_{\mathrm{src}}(t)) \cdot \sin(\omega_0 t + \varphi_{\mathrm{src}}(t)). \tag{3.21}$$

After the mixing stage with the IF signal

$$v_{\mathrm{IF,\ 90^\circ}}(t) = v_{\mathrm{sup}}(t) \cdot v_{\mathrm{LO,\ 90^\circ}}(t) \cdot l_{\mathrm{M}}, \tag{3.22}$$

which is influenced by conversion losses l_{M} from the mixer and the LNA with the amplification gain g_{LNA}, a low-pass filtering follows. When small-angle approximations are not applied, the resulting output signal is

$$\begin{aligned} v_{\mathrm{out}}(t) = &- g_{\mathrm{LNA}} l_{\mathrm{M}} V_0 V_{\mathrm{DUT}} \left(\frac{\sin(\varphi(t))}{2} + \alpha_{\mathrm{src}}(t) \sin(\varphi(t)) \right. \\ &\left. + \frac{\alpha(t) \sin(\varphi(t))}{2} + \frac{\alpha_{\mathrm{src}}(t)^2 \sin(\varphi(t))}{2} + \frac{\alpha(t)\alpha_{\mathrm{src}}(t) \sin(\varphi(t))}{2} \right). \end{aligned} \tag{3.23}$$

After applying small-angle approximations with respect to φ, α, φ_{src}, and α_{src} the output signal $v_{\mathrm{out}}(t)$ is reduced to

$$v_{\mathrm{out}}(t) = -\frac{g_{\mathrm{LNA}} l_{\mathrm{M}} V_0 V_{\mathrm{DUT}} \varphi(t)}{2}, \tag{3.24}$$

which directly corresponds to Equation 3.17, where the suppression is assumed to be ideal. The remaining terms are independent of the partial suppression factor p as well. An imperfect suppression shows under these conditions no influence as the suppression factor p is neither present in Equation 3.23 nor in Equation 3.24.

The next modification assumes a slight deviation from the ideal 90°-condition necessary for phase noise detection including an additional phase term q, representing the imperfection, in the main source signal given by Equation 3.18. After the partial carrier suppression, the mixing, and the low-pass filtering, the output signal results in

$$\begin{aligned} v_{\mathrm{out},q}(t) = &\ g_{\mathrm{LNA}} l_{\mathrm{M}} V_0^2 p \alpha_{\mathrm{src}}(t) \sin(q) - \frac{g_{\mathrm{LNA}} l_{\mathrm{M}} V_0 V_{\mathrm{DUT}} \alpha(t) \alpha_{\mathrm{src}}(t) \sin(\varphi(t))}{2} \\ &- \frac{g_{\mathrm{LNA}} l_{\mathrm{M}} V_0 V_{\mathrm{DUT}} \sin(\varphi(t))}{2} - g_{\mathrm{LNA}} l_{\mathrm{M}} V_0 V_{\mathrm{DUT}} \alpha_{\mathrm{src}}(t) \sin(\varphi(t)) \\ &- \frac{g_{\mathrm{LNA}} l_{\mathrm{M}} V_0 V_{\mathrm{DUT}} \alpha(t) \sin(\varphi(t))}{2} + \frac{g_{\mathrm{LNA}} l_{\mathrm{M}} V_0^2 p \alpha_{\mathrm{src}}(t)^2 \sin(q)}{2} \\ &- \frac{g_{\mathrm{LNA}} l_{\mathrm{M}} V_0 V_{\mathrm{DUT}} \alpha_{\mathrm{src}}(t)^2 \sin(\varphi(t))}{2} + \frac{g_{\mathrm{LNA}} l_{\mathrm{M}} V_0^2 p \sin(q)}{2}. \end{aligned} \tag{3.25}$$

In addition to the remaining very small terms, terms depending on $\sin(q)$ and on the partial suppression factor p appear and likely lead to a false detection of phase noise and amplitude noise in the resulting output spectrum instead of solely detecting pure phase or amplitude noise. Assuming a small-angle approximation of first order with respect to the noise quantities φ, α, φ_{src}, and α_{src} is still valid, the expression further reduces to

$$v_{\mathrm{out},q}(t) = g_{\mathrm{LNA}} l_{\mathrm{M}} V_0 \left(V_0 p \alpha_{\mathrm{src}}(t) \sin(q) + \frac{V_0 p \sin(q)}{2} - \frac{V_{\mathrm{DUT}} \varphi(t)}{2} \right). \quad (3.26)$$

Equation 3.26 shows that the critical noise contribution stems from the main oscillator amplitude noise in dependence of the phase deviation from 90°, and that a similar contribution from the suppression imperfection is present in the output spectrum. The small-angle approximation is valid as long as $\delta \lesssim 8°$ holds for either quantity δ, as the introduced error in this case stays below 1 %.

In case of a phase deviation in the coarse suppression region instead of in the LO path, introduced by a possible transmission line mismatch, the influence of the source signal's noise components changes further. With the phase deviation, denoted by a phase component r, the output signal turns into

$$\begin{aligned} v_{\mathrm{out},r}(t) = g_{\mathrm{LNA}} l_{\mathrm{M}} V_0 V_{\mathrm{DUT}} \Bigg(& -\alpha_{\mathrm{src}}(t) \sin(r) \cos(\varphi(t)) - \frac{\sin(r)\cos(\varphi(t))}{2} \\ & -\alpha_{\mathrm{src}}(t) \sin(\varphi(t)) \cos(r) - \frac{V_{\mathrm{DUT}} \alpha_{\mathrm{src}}(t)^2 \sin(\varphi(t)) \cos(r)}{2} \\ & - \frac{\alpha(t) \sin(r) \cos(\varphi(t))}{2} - \frac{V_{\mathrm{DUT}} \alpha(t) \sin(r) \cos(\varphi(t)) \alpha_{\mathrm{src}}(t)}{2} \\ & - \frac{\alpha(t) \sin(\varphi(t)) \cos(r)}{2} - \frac{V_{\mathrm{DUT}} \alpha(t) \sin(\varphi(t)) \cos(r) \alpha_{\mathrm{src}}(t)}{2} \\ & - \frac{\alpha_{\mathrm{src}}(t)^2 \sin(r) \cos(\varphi(t))}{2} - \frac{V_{\mathrm{DUT}} \sin(\varphi(t)) \cos(r)}{2} \Bigg), \end{aligned} \quad (3.27)$$

where the phase component r is present in all terms. Depending on whether the deviation is either small or close to $\pi/2$, the phase component r supports different terms in their influence. For small r, the terms including amplitude noise are reduced, whereas for larger r the amplitude noise components are not affected. How this is visible in the measured spectrum is shown in Section 3.4.5.

Considering a non-ideal mixing stage by taking higher order mixing processes into account and expanding the mixing product likewise into a Taylor series according to

$$i_{\mathrm{mix,\ out}}(t) = I_0 + \frac{G}{1!} (v_{\mathrm{RF}} + v_{\mathrm{src}}) + \frac{G'}{2!} (v_{\mathrm{RF}} + v_{\mathrm{src}})^2 + \frac{G''}{3!} (v_{\mathrm{RF}} + v_{\mathrm{src}})^3 + \ldots, \quad (3.28)$$

leads to a vast amount of additional frequency components to be considered [46]. Still, as the frequency of interest is solely the IF, the third order term can be neglected as it only appears as multiples of the RF and LO frequency components, which typically are easy to filter. The next higher order term in contrast introduces signal power in the IF, but does not change the output spectrum significantly. The operating point of the mixer for accelerator control application is typically set such that the dynamic conductance G is approximately linear. If irregularities occur and the operating point of the phase detector's mixer moves to more non-linear conditions, based on the discussion above, no additional noise sources appear.

Considering a noisy source signal, the theoretical description of the output spectrum in Equation 3.17 does not change when only taking first order terms into account.

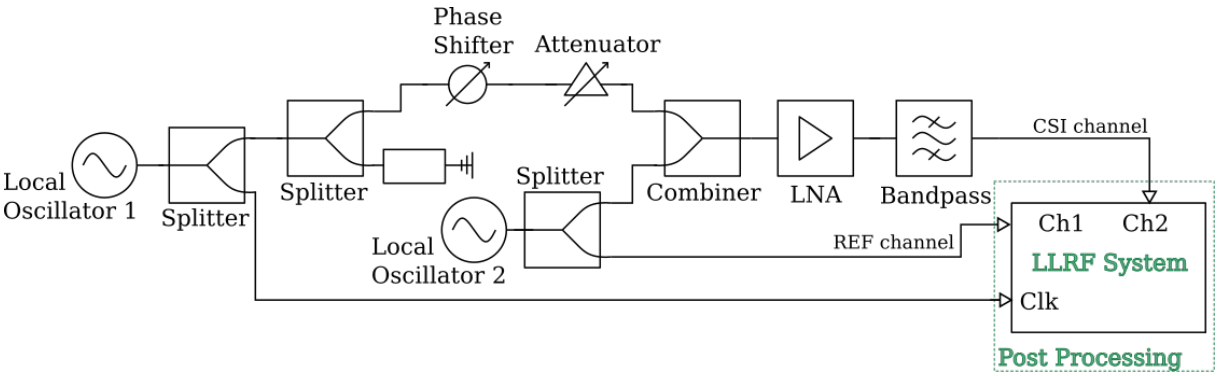

Figure 3.6: CSI block diagram with two independent signal sources at 1.3 GHz.

For the next consideration in line with the future accelerator application, the system is supplied not by one but by two sinusoidal signal sources denoted as *Signal Source 1* (reference signal) and *Signal Source 2* (cavity signal), as shown in Figure 3.6. Both sources are locked to the same fundamental frequency ω_0, where *Signal Source 2* is the source which is to be evaluated and the other one holds as the reference. The result in Equation 3.19 changes to

$$v_{\mathrm{src2}}(t) = V_2(1 + \alpha_{\mathrm{src2}}(t)) \cos(\omega_0 t + \varphi_{\mathrm{src2}}(t)). \tag{3.29}$$

For a non-ideal carrier suppression and ideal 90°-conditions, the output spectrum contains the following terms after low-pass filtering and small-angle approximation:

$$v_{\mathrm{out}}(t) = \frac{1}{2} g_{\mathrm{LNA}} l_{\mathrm{M}} V_1 V_2 \left(\varphi_{\mathrm{src1}}(t) - \varphi_{\mathrm{src2}}(t)\right). \tag{3.30}$$

The phase noise terms stemming from the two sources are independent from the suppression factor p. The specific noise performance of one source can only be investigated, if the noise contribution of the other source equals zero. Analogously to Equations 3.25 and 3.27, additional phase delays either in the suppression bridge or the LO path lead to leakage of amplitude noise during the phase noise detection and the presence of the phase noise footprints of both sources in the output spectrum. This holds vice versa for the presence of amplitude noise.

For laboratory work, the aforementioned relation $\mathcal{L}(f) = \frac{1}{2}S_\varphi(f)$ is commonly used, as most of the measurement devices already display the single sideband (SSB) power spectral density $\mathcal{L}(f)$. In practice, $\mathcal{L}(f)$ can handwavingly be expressed with

$$\begin{aligned}[\mathcal{L}(f)]_{\mathrm{dB}} =&[\text{SSB thermal noise}]_{\mathrm{dB}} - [\text{signal power}]_{\mathrm{dB}} + [\text{LNA noise figure}]_{\mathrm{dB}} \\ &+ [\text{internal losses}]_{\mathrm{dB}}\end{aligned} \tag{3.31}$$

as a proof of power consistency and plausibility [61]. The signal power is measured behind the DUT, the noise figure is specified in the corresponding data sheet and the internal system losses originate in the coupler and waveguide sections.

3.3 Calibration

The main task of the calibration procedure for the CSI is to provide the ability to read out the noise signal in degrees or else from the plotted spectrum in dBc/Hz. To achieve this, a factor has to be found by which the CSI output signal is expanded compared to the common output signal (REF) going into the LLRF-system without nulling the carrier frequency. The LLRF-system is well-known in phase and amplitude noise characteristics, pre-calibrated, and verified by independent commercial noise analyzers [8], [62]. There are a few options to solve this task of calibrating the measurements, either in time domain or in frequency domain. This section highlights the routines applied so far and discusses the possibilities of further improvement.

3.3.1 Calibration in Frequency Domain

The calibration routine for the CSI in frequency domain follows the fundamental idea of injecting a known modulated signal in both signal channels (CSI and the REF signal channel), as this modulation signal should be visible as a striking disturbance in the resulting frequency spectra on both channels. As shown in Figure 3.4, besides the DUT an additional phase shifter is placed within the coarse suppression region. This phase shifter is used to imprint the calibration signal. It modulates the RF

signal by applying a modulated sinusoidal voltage coming from a function generator at the biasing port of the phase shifter. The amplitude of the modulation signal has to be high enough to be detected on both measurement channels.

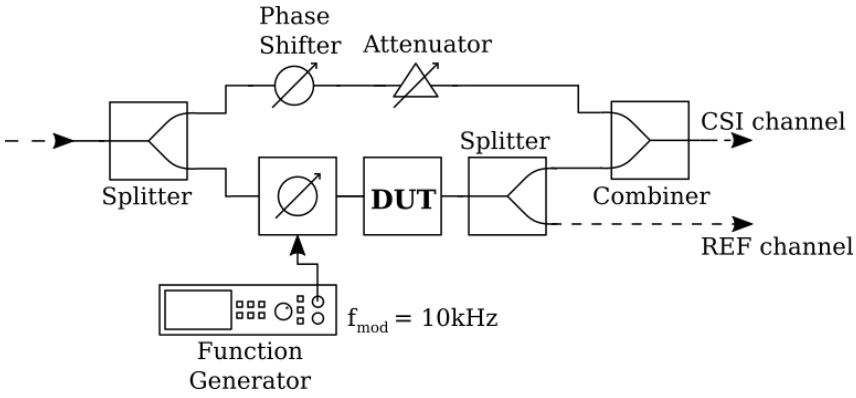

Figure 3.7: Coarse suppression region with phase modulation.

The modulating device is placed before splitting the DUT signal in order to see the modulation in the CSI signal channel as well as in the REF path, as displayed in Figure 3.7. The modulation results in sidebands of the carrier frequency of 1.3 GHz, which is displayed by a spectrum analyzer in Figure 3.8. In this picture the suppressed carrier is the center peak. The peaks directly next to the carrier frequency show the modulated sidebands, the peaks further away are harmonics.

As the modulated signal passes the same conditioning as the noise sidebands of the carrier signal, one can compare the peaks introduced by the modulation in the frequency domain in both input channels. By fitting the level of the two peaks in frequency domain and under the assumption that the calibration of the LLRF-system itself is valid, the CSI spectrum is subsequently adjusted by the amount that the suppression and the amplification have introduced. The resulting adjusted spectra are shown in Figure 3.9, with the peaks enlarged. A slight difference between both maxima is visible, which is caused by limited amount of considered data points and additional rounding errors in the post-processing system. The resulting correction factor one needs to apply can be described by the ratio of the maxima at the modulation frequency f_{mod}. It follows for the calibration factor qualitatively

$$F_{\mathrm{FD}} = \frac{C_{\mathrm{REF}}(f_{\mathrm{mod}})}{C_{\mathrm{CSI}}(f_{\mathrm{mod}})}, \tag{3.32}$$

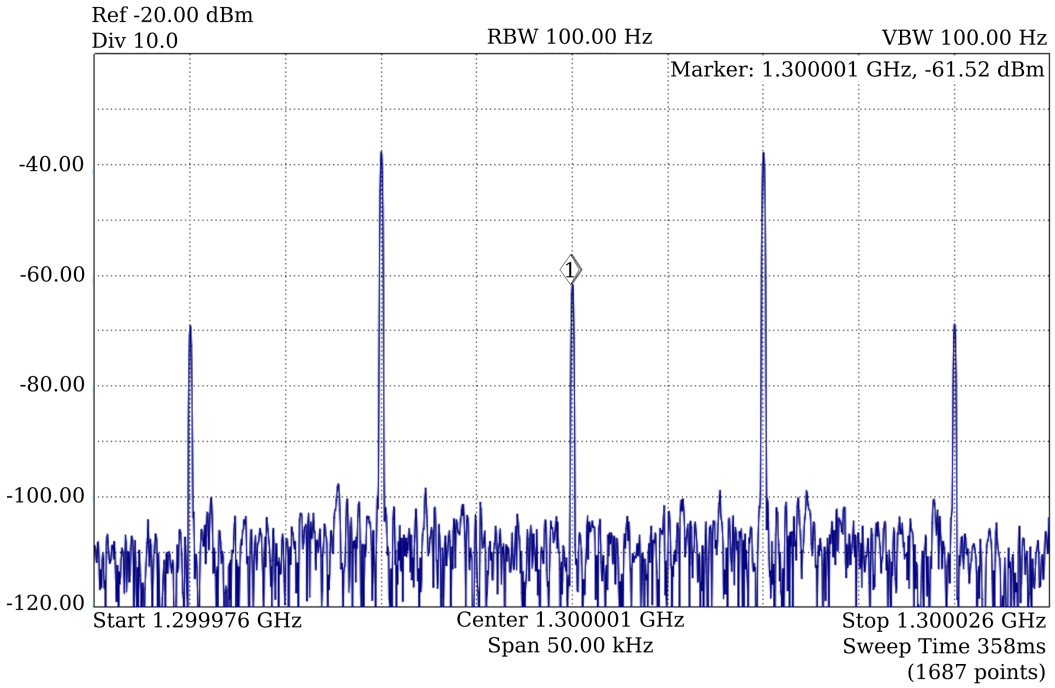

Figure 3.8: Screenshot of the spectrum analyzer for the calibration modulation of $f_{\mathrm{mod}} = 10\,\mathrm{kHz}$ while suppressing the carrier frequency.

with the spectral densities of the signal of the reference channel C_{REF} and of the CSI C_{CSI} as defined in Equation 2.11 and evaluated at f_{mod}. The spectrum detected by the reference channel is pre-calibrated with system specific factors, where a sinusoidal modulation signal is presumed [63]. In practice, the calculated calibration factor F_{FD} deviates by up to 0.5 dB.

Since a modulation in phase is introduced, the correction factor is only suitable for PN measurements, assuming the phase modulation is significantly stronger than a possible amplitude modulation that is unintentionally introduced at the same time. One has to note that the calibration device is always within the coarse suppression region and therefore might cause noise as well. Furthermore, the device must be capable of handling the high signal power levels within this region, as the carrier power is not yet limited. The calibration for AN measurements can be realized analogously with a modulated attenuator.

To overcome the risk of introducing noise by the calibration unit and overlaying the actual noise of the DUT, a more complex structure, the two-coupler-modulation unit, is implemented. The adapted calibration unit is shown in Figure 3.10. The incoming signal is split in the first coupler. The larger part of the signal power

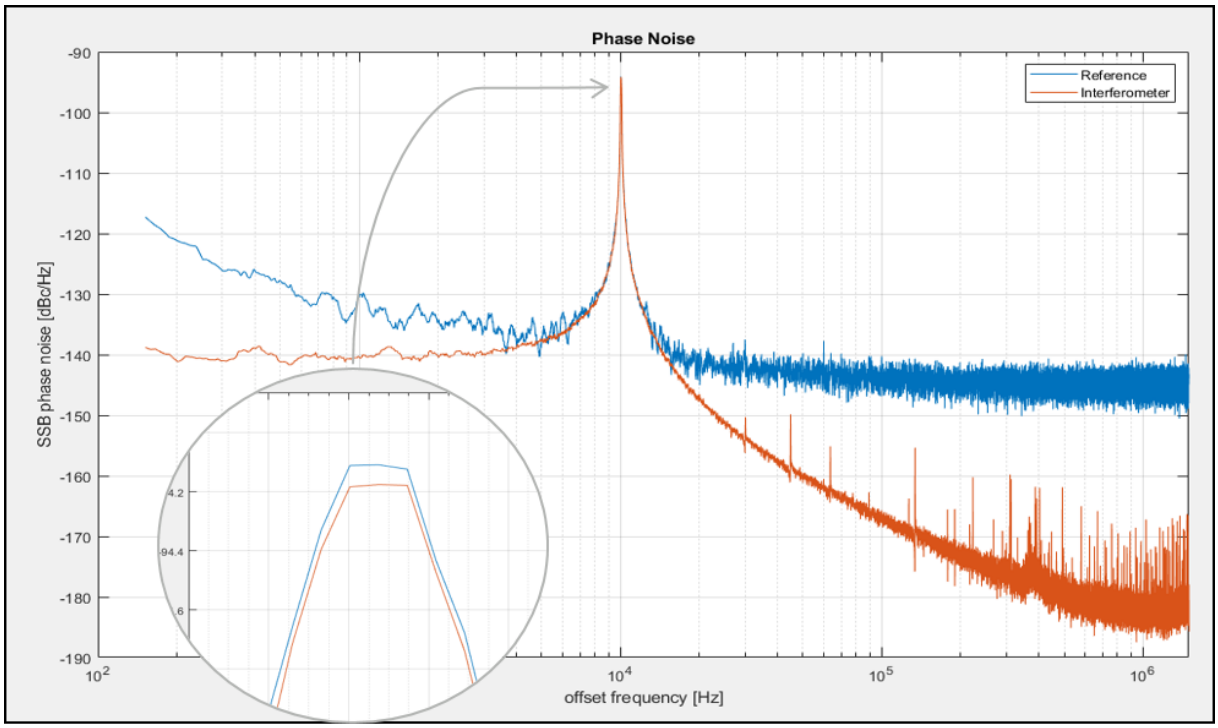

Figure 3.9: Calibration spectrum after peak fitting.

passes with only small losses of around 0.4 dB compared to several decibels when directly passing the calibration actuator. The decoupled signal heads towards the actuator, again a phase shifter, which is used for the modulation of the calibration signal. A further benefit is the reduced signal power at the input of the actuator. Depending on the coupling factor of the first coupler, it is possible to measure with high signal power levels without damaging active parts of the calibration device. Another advantage of this unit is the coupling factor of the second coupler to combine the main signal and the modulation again. If the calibration device itself is noisy, the second coupler limits the influence of the calibration device noise on the overall spectrum.

Due to the change in amplitude and phase when summing up two sinusoidal signals in the coupler, one cannot distinguish clearly between phase and amplitude modulation. Adjusting the electrical path length within the calibration unit by a mechanical phase shifter results in the separation of the observable modulation, either in phase or amplitude. The modulation in phase is at maximum, when the amplitude of the output signal of the calibration unit is at minimum. Since the change in amplitude is rather small depending on the coupling factor, it helps to

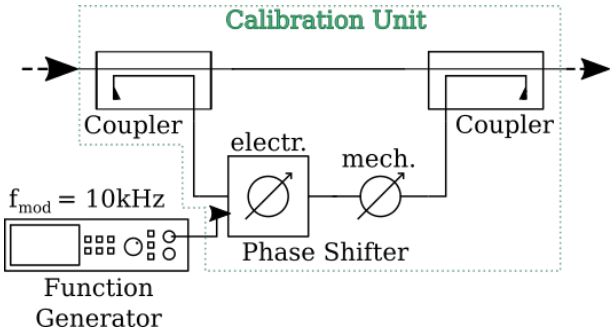

Figure 3.10: Block diagram of the two-coupler-modulation unit replacing the calibration phase shifter.

simultaneously cross-check the visibility of the introduced modulation with a signal source analyzer (SSA).

Nevertheless, using a phase shifter as a calibration actuator inside the coupler structure without path length adjustment introduces mainly a phase modulation, while using an attenuator mainly results in amplitude modulation. There are two options to switch the system between amplitude and phase calibration. One option is to exchange the modulator, i.e., change between a variable attenuator and a phase shifter. This option requires two different setups, which is not practical. The other option is to take advantage of the trigonometric relations between both signals in the enhanced two-coupler-modulation unit. By adjusting the electrical path length of the decoupled signal, the influence of the phase modulation can be maximized or minimized. In the latter case, the previously unintended detection of the amplitude modulation is maximized. There is no need to exchange the actuator between the couplers if the path lengths match. A rejection between amplitude and phase modulation of 30 dB can be achieved. This behavior has not only been investigated in theory, but also with a commercial phase noise analyzer [60] by displaying amplitude and phase noise simultaneously.

To simplify this calibration unit further, one could consider using a vector modulator (VM) as a calibration actuator. The advantages of exchanging the calibration phase shifter with a VM are that, on the one hand, both actuator types are combined in one unit whereas, on the other hand, one can avoid the path length required to distinguish between amplitude and phase modulation. Still, for properly adjusting the post-processing system prior to measurements, one has to assume the modulation peak to be of either phase or amplitude type. The post-processing system then detects the signal phase and corrects it internally to either phase or amplitude noise measurement conditions. Considering this, calibrating for phase

and amplitude noise at the same time is not realizable in frequency domain at the moment and thus has to be done sequentially.

Figure 3.11 shows the cross-checking results of the CSI calibration compared to commercial noise analyzers. Therefore, it is important to consider a DUT which is noisy enough across a broad band of frequencies to be detected by all systems of interest. For validating both types of measurements the chosen DUT inside the

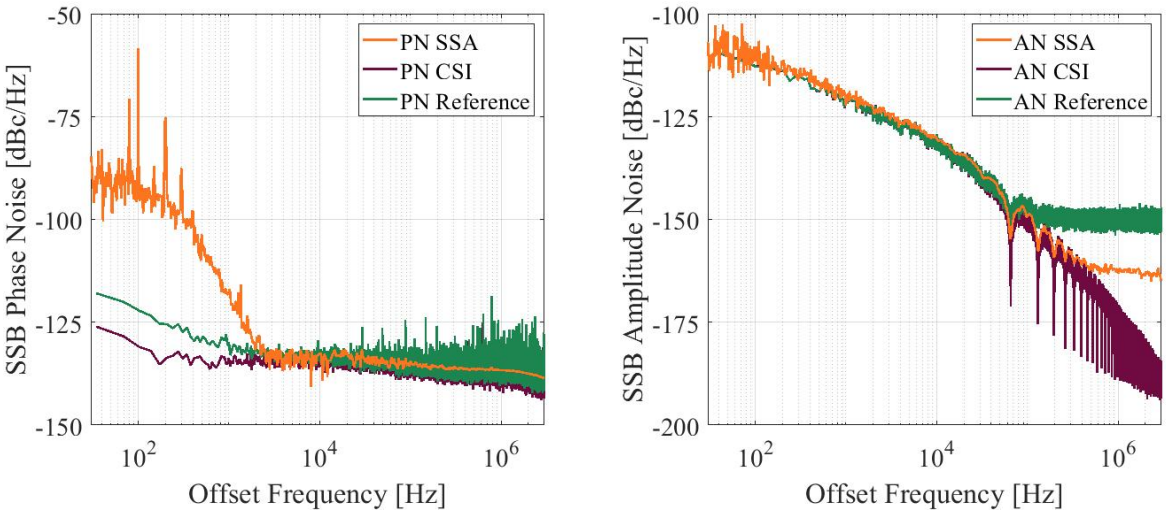

(a) Phase Noise. **(b)** Amplitude Noise.

Figure 3.11: Comparison of the CSI and commercial noise detection systems and proof of the calibration routine by measuring the same noise-modulated signal. For the phase noise measurements a phase shifter was modulated with a white noise signal, for amplitude noise an attenuator was modulated with a pink noise signal.

CSI (see Figure 3.4) is a phase shifter combination biased with a noise signal of a certain amplitude such that the imprinted noise is visible in all measurement devices. Different noise signal generators are used for the presented test results. For the phase noise test white noise is applied, while for the amplitude noise test it is pink noise. Both plots show that the CSI measurement results matches with a certainty of 1 dB to 2 dB the results of the commercial systems. Figure 3.11(a) shows a steep increase of phase noise for close-in offset frequencies in the data from the SSA. This is probably caused by the common signal part, which is strongly reduced within

the LLRF-system by downconversion. For the amplitude noise measurements in Figure 3.11(b) the three curves split for offset frequencies of above 500 kHz due to the different resolution limits of the systems. These two measurements confirm the calibration routine of the CSI in frequency domain.

3.3.2 Calibration in Time Domain

Considering that the incoming DUT time signal includes both PN and AN information, a calibration in time domain can be assumed to be advantageous. Without the need to subsequently calculate the FFT of the incoming time signal, the signal processing can be faster and the calibration routine more time-efficient. Instead of the previously described sensitive calibration unit, a simple signal coupler is placed after the DUT for the injection of an externally generated calibration signal of known offset to the carrier frequency.

The block diagram for this type of calibration routine is shown in Figure 3.12. The calibration signal is a sinusoidal wave signal with a distinct offset from the

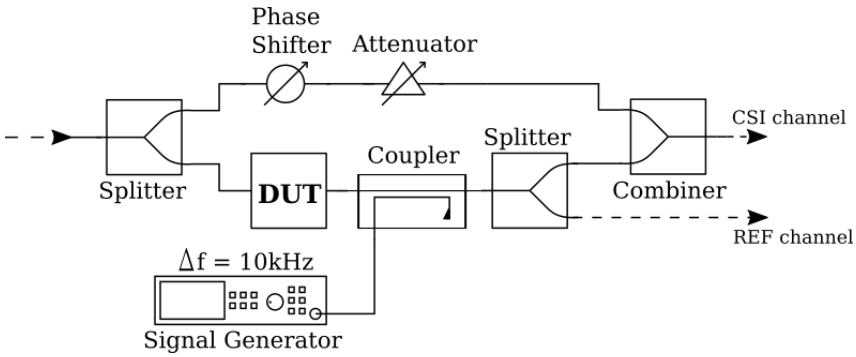

Figure 3.12: Block diagram of the inner setup configuration for calibration by offset frequency injection.

carrier signal. As the calibration signal is not dependent on an exact frequency offset and purity, there is no need to have a special signal source or frequency locking for the generation of the calibration signal. By injecting this signal into the system via the coupler, again a sum of both signals is generated leading to amplitude and phase modulation.

The overall assumption of this method is the constant phase relation between the signals of the REF and the CSI channel. This leads to the possibility to use the phase

position of the REF channel for the CSI channel phase position. As shown in Figure 3.13, in time domain the maximum for amplitude noise is found in the maxima of the time signal, the maximum for phase noise is to be detected at zero crossing or by shifting the data vector by 90°. This option to identify the turning points in the

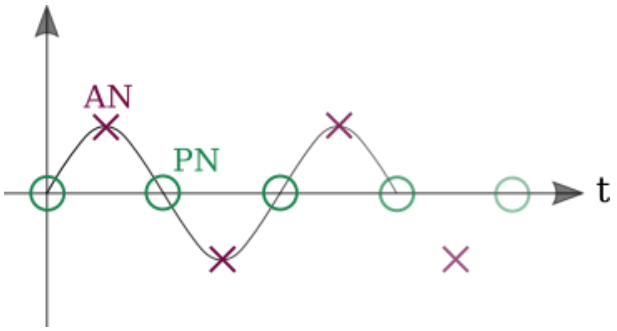

Figure 3.13: Illustration of the relationship of the signal information for both measurement channels during time domain calibration in time domain.

reference signal and translate them to the CSI signal is substantial for this method as the phase information in the CSI channel is undetectable for the LLRF-system if the carrier is suppressed. Figure 3.14 gives an overview of the relationship between

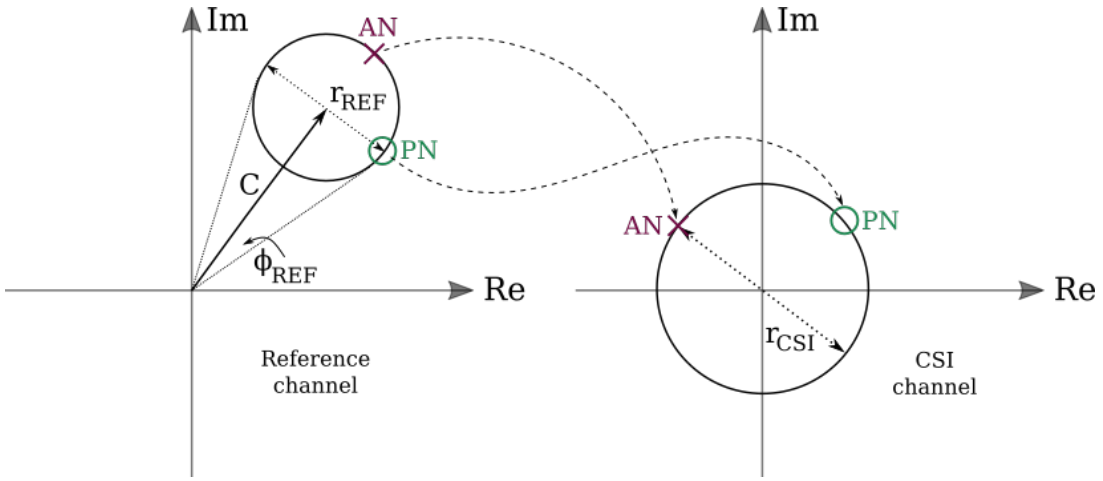

Figure 3.14: Illustration of the relationship between the extrema of the measured time signal and amplitude noise or phase noise, respectively.

the REF and CSI channel signals in the complex plane. The measurements from the REF channel allow to determine the PN and AN contribution in the CSI channel. In order to adjust the post-processing system's phase to the correct angle, one needs to find the corresponding vector rotation information in the measurement signals for the adjustment in the complex plane. The necessary information is obtained from the time signal. Since, as shown in Section 2.2.3 and Equation 2.30, the amplitude and the phase of the IQ decomposed signal correspond to its real and imaginary part, the easiest approach is to find the amplitude information in the time signal and take the corresponding complex data vector entry to find the measurement data orientation in the complex plane [53]. Assuming the phase relation between the REF and the CSI channel remains constant, the maxima found in the time signal of the REF channel correspond to the non-detectable maxima in the CSI channel. The orientation or else the angle between the real axis and the amplitude data vector is now detected, such that the data vector for both channels can be rotated onto the real axis. Thus, the phase angle required for system calibration is now known. Following, the scaling factor corresponding to the difference in signal power between the REF and the CSI channel needs to be calculated. According to Figure 3.14, this can simply be done by the comparison of the diameters of the measurement data in the complex plane when the data vectors both originate in the same point. The small modulation deforms the unit circle only by a little, so that a circle can still be assumed in good approximation. Following trigonometric considerations, the scaling factor F_{TD} follows with

$$F_{\mathrm{TD}} = \frac{\Phi_{\mathrm{REF}}}{r_{\mathrm{CSI}}} = \frac{r_{\mathrm{REF}}}{r_{\mathrm{CSI}}} \cdot \frac{1}{C}, \tag{3.33}$$

where r_{REF} is the radius of the reference data and r_{CSI} that of the CSI data in the complex plane, respectively. The factor C represents the carrier vector.

The time domain calibration approach works without additional actuators like, e.g., a calibration phase shifter. This is beneficial as no unwanted additional noise sources and losses stemming from active devices in the setup are part of the system. Further advantages are the possibility to calibrate the system for AN and PN measurements at the same time, instead of subsequently, as both modulation types are generated at the same time.

While measurements are promising and agree with the frequency-domain based calibration, a few principle-inherent challenges remain. Firstly, if the injected offset frequency signal is too high in power, one is not able to distinguish clearly between the signal of interest and the calibration signal, which in consequence leads to a faulty calibration. A difference of around 25 dB between the power of the carrier

signal and the calibration signal has shown to be advantageous. Secondly, the calibration routine as it currently is configured runs into errors for highly noisy DUTs, because of the overlay of the injected modulation by the noise sidebands of the DUT. This issue was partially resolved by proper signal filtering before identifying the angular relations. A third and even more challenging error source is hidden in the post-processing system. Figure 3.15 shows exemplarily the calculated optimum points in the complex plane for the time signal calibration. One can see

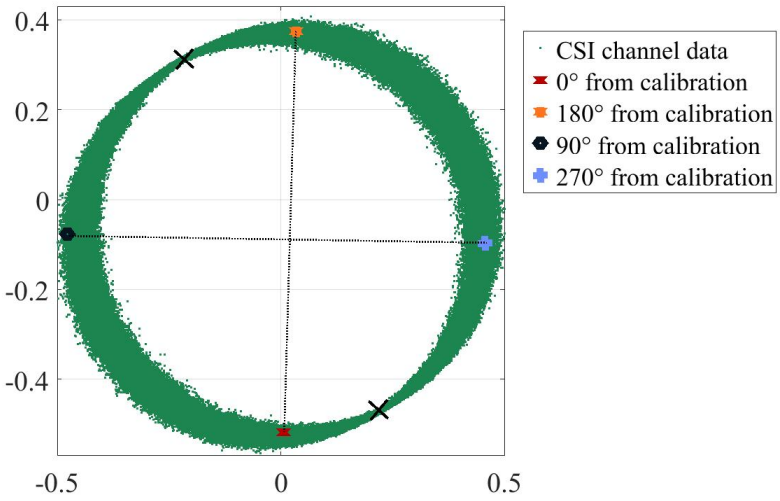

Figure 3.15: Measurement data in the complex plane with marked calculated optimum calibration points.

the four phase adjustments that are proposed by the algorithm as being optimal, marked by colored highlights. In addition, the corresponding measurement data is plotted in green. According to a system calibration for phase noise measurements, one would expect the 0° and 180° marker in the thinnest area of the green curve, marked by crosses. The search for the maximum and its phase position is executed multiple times in a row and averaged to a final optimum at the end.

One can exemplarily see in Figure 3.16, that for the identification of a single maximum, two data point clusters marked in green appear before averaging. The angle between both clusters is constant at around 20° and has been decreased by a firmware update of the post-processing system to around 10°. As the final rotation angle is determined by an average across all detected maxima, marked by a red

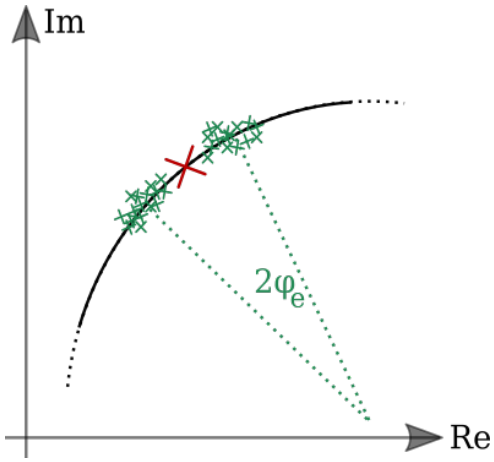

Figure 3.16: Example of calibration error due to data clustering and averaging.

cross in Figure 3.16, this discrepancy is a fundamental technical issue. The data points are not equally split in these two spots and it occurs that only a few outliers arise, but still the average is highly influenced and therefore the final angle rotation might not fit. If the rotation angle for the reference channel is calculated wrongly, the data rotation for the CSI data becomes faulty. Figure 3.17 highlights what happens to the measurement data vector when the calibration is faulty. Instead of a clear differentiation between AN and PN components, the calibration results in a mixture of both components and therefore in a mixed output spectrum of both AN and PN.

Additional experiments on the saturated mixer as a phase detector have shown that already a few degrees deviation from the optimal 90°-condition lead to changes in the baseband spectrum. The constant deviation in the calibration angle is very close to the turning point found in the experiments. This observation is supported by the brief analysis in Section 3.2.

With this calibration method in time domain, one could not only avoid noise contributions and power losses, since only a single coupler needs to be placed in the CSI and the calibration in AN and PN is derived simultaneously, it could also yield significant savings in terms of processing time, provided that future work enables solving the above challenges. Possibilities for improvements are to increase the sampling frequency, which in consequence requires a higher clock rate, and the usage of a lower modulation frequency, which requires the implementation of narrow-band filtering and leads to longer measurement durations.

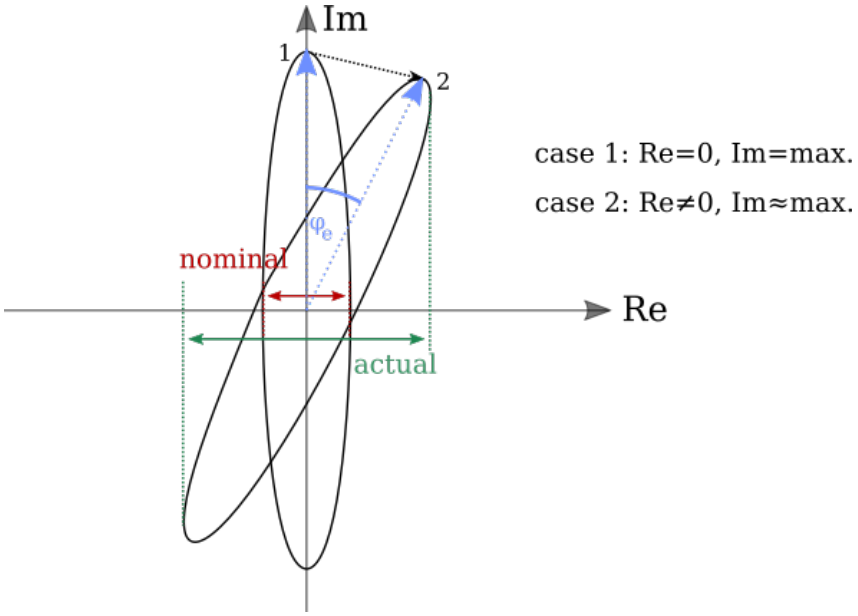

Figure 3.17: Depiction of the consequence of a faulty calibration angle for the time domain calibration.

3.4 Measurement Limitations

Over the years, as shown in the experimental setups in Section 3.1, the CSI setup constantly evolved for the sake of its steady noise optimization, stabilization, and compactification. During the development process various internal and external influences and boundary conditions detrimental to these goals were addressed and mitigated in order to achieve the presented measurement accuracies. This section highlights critical factors and issues in the setup, reports noise floor measurements of the CSI and investigates influences of related system components.

3.4.1 Environmental Influences

The setup has shown to be especially sensitive regarding environmental influences and electromagnetic disturbances, which were investigated thoroughly. Starting on the environmental background, vibrations in particular were critically disturbing, whether stemming from the outside, e.g., construction work, or from walking in and around the laboratory. Such vibrations lead to instabilities of the carrier suppression or leave a foot print in the measurement spectra. With the progress of the setup, the components of the CSI were properly fixed by clamps to an bread board used in optical measurement systems. This re-arrangement makes the setup less sensitive

against movements in its close vicinity. To decouple the entire CSI setup from outer vibrations, soft foam was placed between ground plate and desk surface.

Additionally, the size of the setup was reduced by around one half. This was possible by the exchange of noisy and instable components and the combination of the main signal splitting and recombination area inside a shielded printed circuit board (PCB), as shown in Figure 3.18.

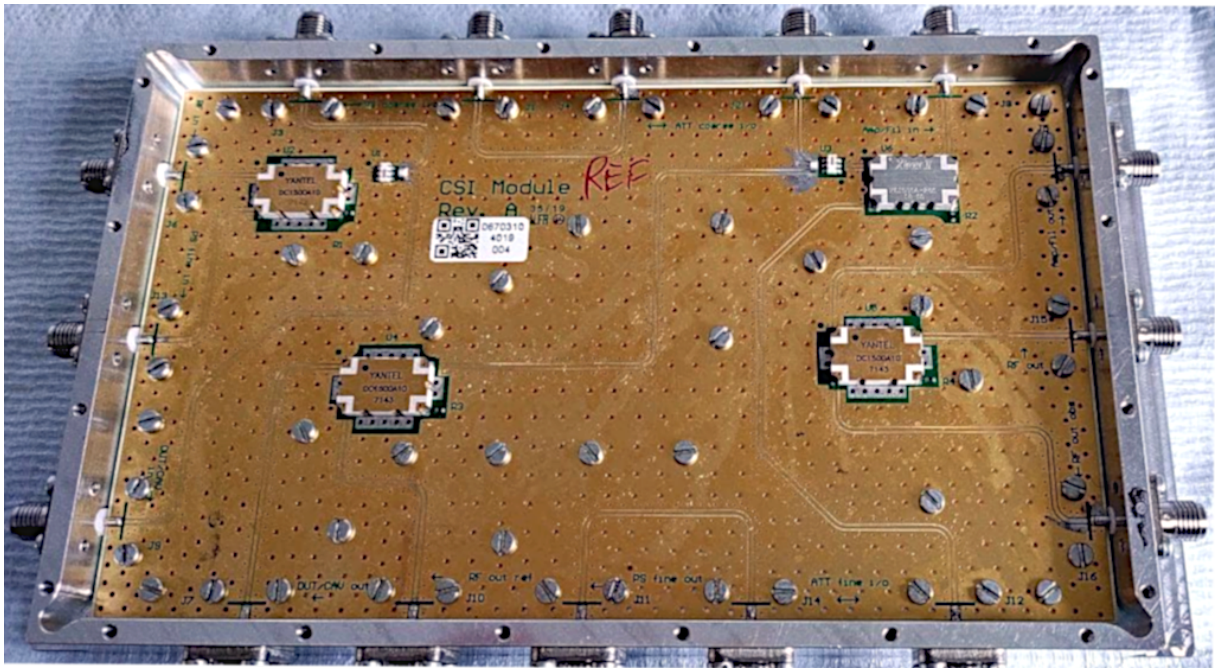

Figure 3.18: Picture of the PCB containing signal splitters and couplers.

The PCB is designed as a multilayer of RO4350B [64] to reach a robust board thickness of 1 mm. Besides its own stability, multiple copper planes offer a thermal shield to the components. For a solid ground connection, the PCB is screwed to its massive housing. This design not only compresses the setup, but also enables higher mechanical stability and signal stability, as the structure is shielded against outer electromagnetic disturbances.

Nevertheless, the setup is still not immune against vibrations as Figure 3.19 shows. Two measurements are taken in saturated mixer condition and show the output time signals for the CSI under two conditions: Figure 3.19(a) displays the result when dropping a plastic screw driver on the ground plate of the setup and Figure 3.19(b) shows the drop of a needle. The measurements are fed to a DC-

coupled oscilloscope. Each peak represents a jump in the output voltage signal of the phase detector, which again represents an instability of the carrier suppression and constantly changing conditions in the setup during operation.

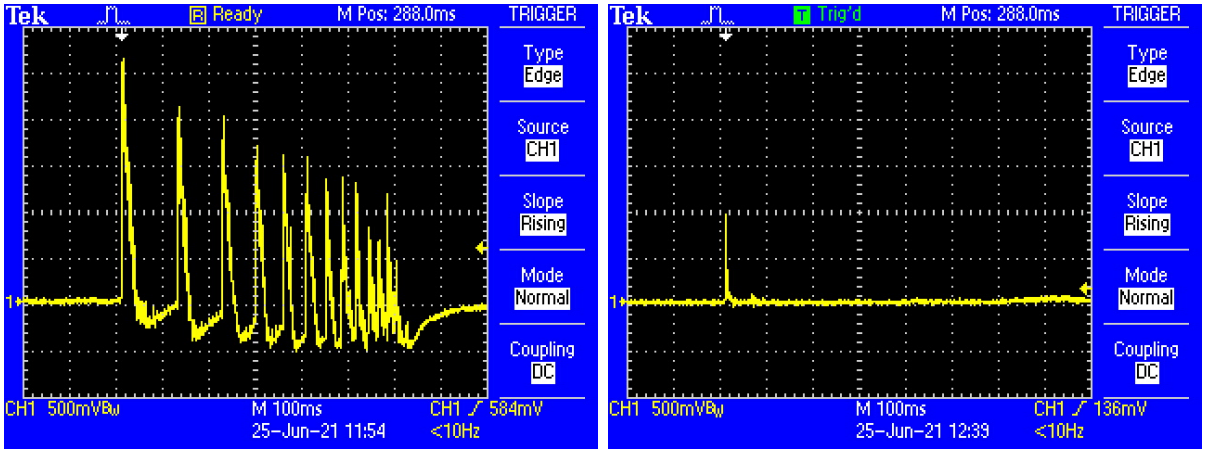

(a) Dropping a plastic screwdriver onto the CSI. **(b)** Dropping a needle onto the CSI.

Figure 3.19: Oscilloscope measurements of vibrational effects in the CSI.

Active fan-cooled components as, e.g., a high-power amplifier, are necessary for the CSI measurements with the very high input signal power, but simultaneously introduce clear disturbances to the measured spectrum. To reduce the influence of the fan to a minimum, the high-power amplifier is physically separated and decoupled, placed on soft foam, and the outgoing air flow is guided away from the measurement setup. The remaining mechanical vibrations transported by the connected RF cables are clearly reduced by sticky tape.

Not only artificial sources for vibrations and temperature changes (such as fans) are problematic. Increased air flow by, e.g., opened windows or doors of the laboratory leads to uncontrollable temperature and humidity changes inside the room. The changes in the air flow and its temperature and the instabilities in the signal source make it either very difficult to suppress the carrier frequency and hold it for a useful amount of time or even impossible to find the suppression conditions. Opening a window for only one minute can lead to a fluctuating carrier suppression for several minutes, violating critical suppression levels without re-adjustment. Unsurprisingly, the more stable the environment is, the easier it is to keep the carrier suppression at a sufficient low carrier power level. This effect decreases with

further steps of compactification and tighter sealing. The mentioned problems are only exemplary for a large variety of difficulties that can occur. Most of them result in spikes in the output noise spectra, but can likely be mitigated by an automated carrier suppression tracking.

3.4.2 Electromagnetic Disturbances

Shielding and solid electrical ground connections are crucial to avoid unwanted electromagnetic disturbances. Surrounding electric devices or signal sources, either

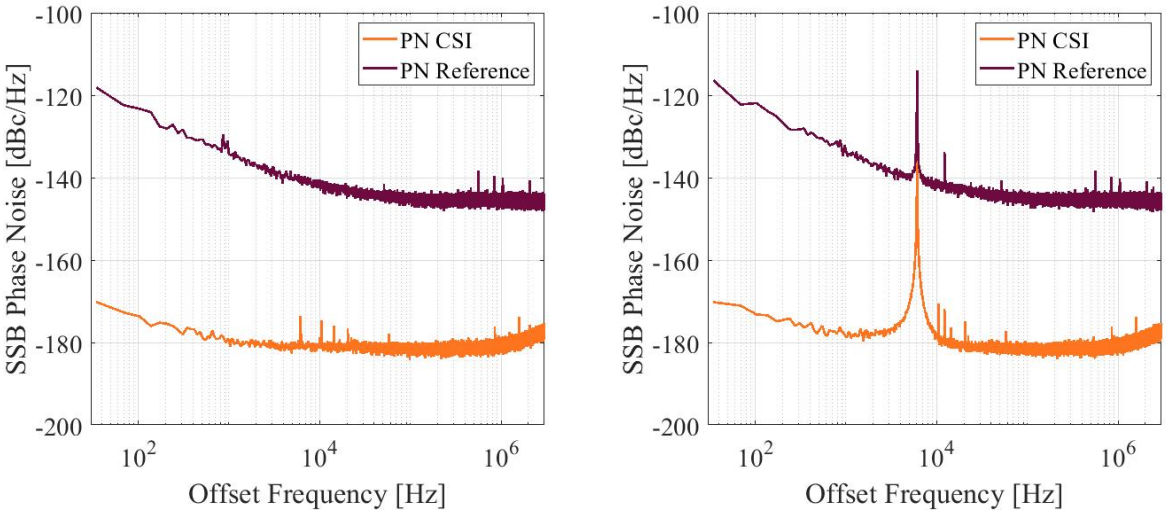

(a) No second signal source in operation.

(b) Second signal source turned on.

Figure 3.20: Phase noise measurements with the CSI showing the effect of neighboring active signal sources.

in the same room or in neighboring laboratories, can provoke electromagnetic disturbances as well. Every frequency generation close to 1.3 GHz in neighboring rooms can be detected as a spur in the measured spectra. Figure 3.20 shows two measurements with the CSI. In Figure 3.20(a) the undisturbed measurement is shown, Figure 3.20(b) presents the disturbed one, when a second signal source at 1.3 GHz in the same room is turned on, appearing as a clear peak in the spectrum. As the two sources are not frequency locked, the second source appears with a frequency offset from 1.3 GHz. Just as clearly, another signal source with a signal

level of about 1 W but terminated with care in the neighboring room could also be identified.

Next to leaking radiation, leakage currents in the baseband are problematic as well. As the CSI itself works in the high-frequency regime, it is robust against a lot of baseband disturbances. Still, some measurement devices need to be disconnected from the CSI setup in order to avoid disturbing spectral peaks, as unwanted non-linear behavior leads to up-conversion from baseband to higher frequencies within setup components. Some ground connection issues could be decreased by either the isolation of the involved reference ground planes or by providing an improved low-impedance ground connection. Future designs need to include solid and homogeneous ground connections and most compact component connections.

3.4.3 Performance in Phase Noise Measurements

After all process and setup optimizations, Figure 3.21 shows the resulting measurement limit of the CSI. It is the best performance that could be achieved with the current CSI front-end and given post-processing system. The CSI curve is shown in comparison to the system performance of the post-processing system without carrier suppression.

For this, a signal input power of 38 dBm at the center frequency of 1.3 GHz is used. The corresponding timing jitter for these uncorrelated measurements is 10.76 as for a measurement band from 40 Hz to 1 MHz. Contributions to the remaining phase noise in the 1/f-regime of the CSI spectrum most likely stem from mechanical RF components inside of the setup, as addressed in the subsequent sections about component characterizations. Nevertheless, a clear dominant remaining noise source is not yet identified. As a result of the investigations carried out, either thermal noise or contact noise inside the suppressing structure are potential suspects.

Following the approximation presented in Equation 3.31, the analytical limit of the SSB phase noise spectrum is given by

$$\begin{aligned}\mathcal{L}(f) =&[\text{SSB therm. noise}]_{\text{dB}} - [\text{signal power}]_{\text{dB}} + [\text{LNA noise figure}]_{\text{dB}} \\ &+ [\text{internal losses}]_{\text{dB}} \\ =&-177\,\text{dBm/Hz} - 33\,\text{dBm} + 0.7\,\text{dB} + 4\,\text{dB} \\ =&-205.3\,\text{dBc/Hz},\end{aligned} \tag{3.34}$$

for a signal power of 33 dBm at the DUT.

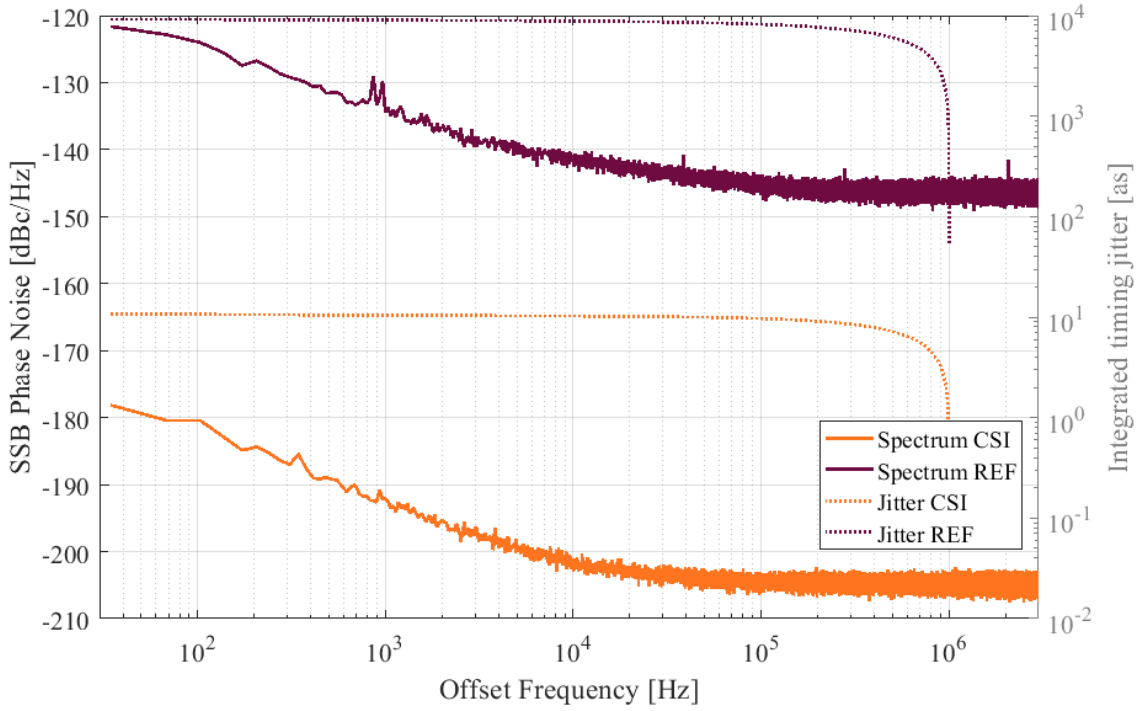

Figure 3.21: Phase noise measurements of the CSI itself in comparison to the standard LLRF measurement.

Bringing the achieved integrated timing jitter t_{RMS} of 10.76 as and the operation frequency $f_0 = 1.3\,\mathrm{GHz}$ into relation, the observable transmission path length change Δl breaks down to

$$\Delta l = t_{\mathrm{RMS}} \cdot f_0 \cdot \lambda = 10.8\,\mathrm{as} \cdot 1.3\,\mathrm{GHz} \cdot 0.23\,\mathrm{m} \approx 3\,\mathrm{nm} \tag{3.35}$$

for propagation in vacuum.

3.4.4 Performance in Amplitude Noise Measurements

Another measurement capability of the CSI is the evaluation of amplitude noise. As described in Section 3.3, the calibration routine for AN requires only an exchange of the calibration unit and minor changes to the software implementation.

The evaluation of amplitude noise measurements revealed a saturation effect in the time domain signal of the detector. The consequences are displayed in Figure 3.22, showing the detected time signals, demodulated in I and Q components. Figures 3.22(a) and 3.22(c) show the resulting scatter plots for each sample of the CSI and the REF channel, respectively, for standard working conditions. In contrast,

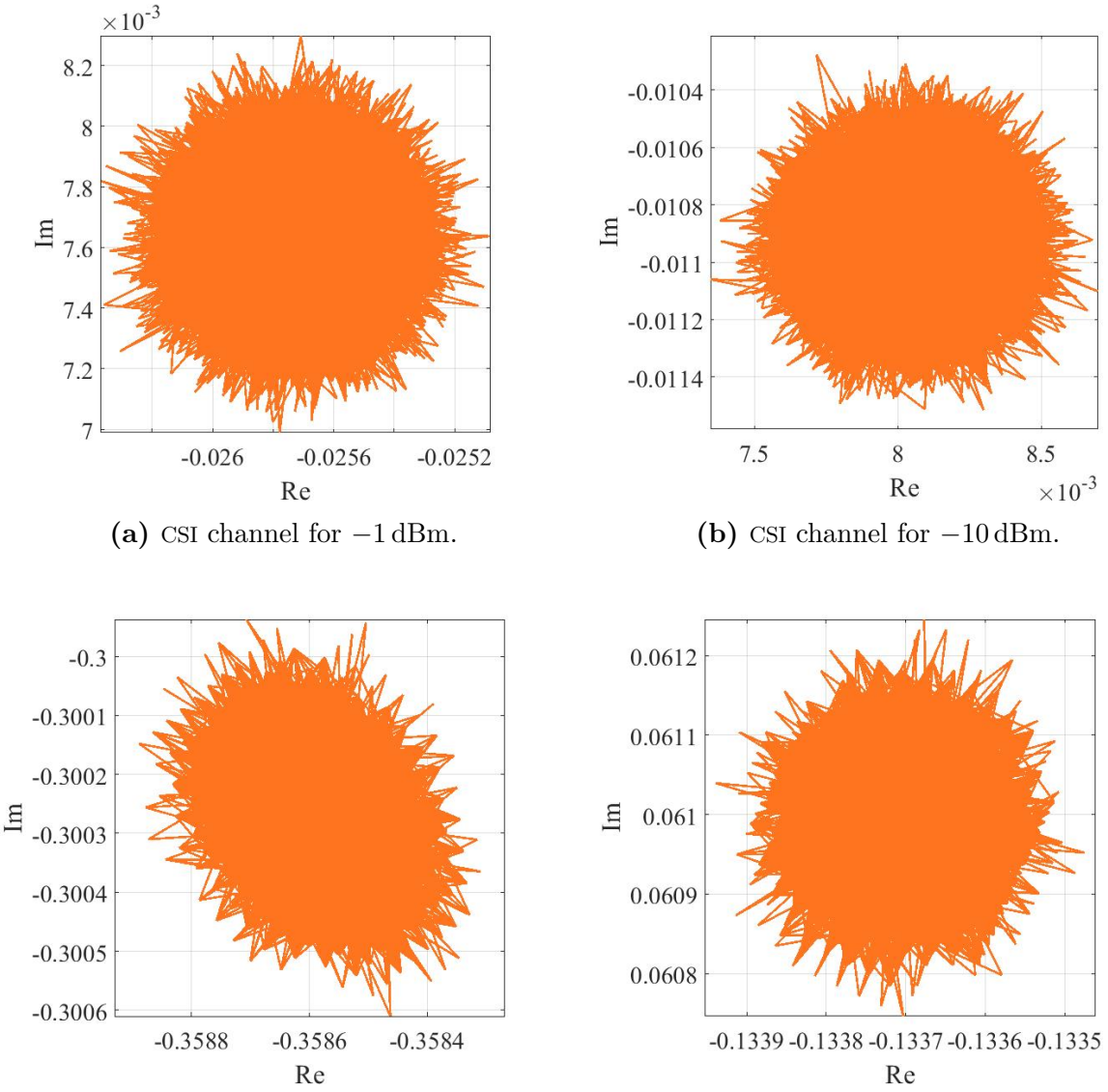

(a) CSI channel for −1 dBm.

(b) CSI channel for −10 dBm.

(c) REF channel for −1 dBm.

(d) REF channel for −10 dBm.

Figure 3.22: Comparison of demodulated signals from the REF and CSI channels for different input power levels.

Figures 3.22(b) and 3.22(d) show similar measurement results, but for a reduced input signal power. It can be seen that three of the four plots display a reasonable representation of a circle. In comparison, Figure 3.22(c) shows an ellipsoidal shape. As the spread of data points in the complex plane is now compressed, the ratio between amplitude and phase modulation is not the same as for the corresponding CSI channel data. This leads to a misinterpretation of the scaling values during amplitude calibration and subsequently to a miscalculation of the noise floor for

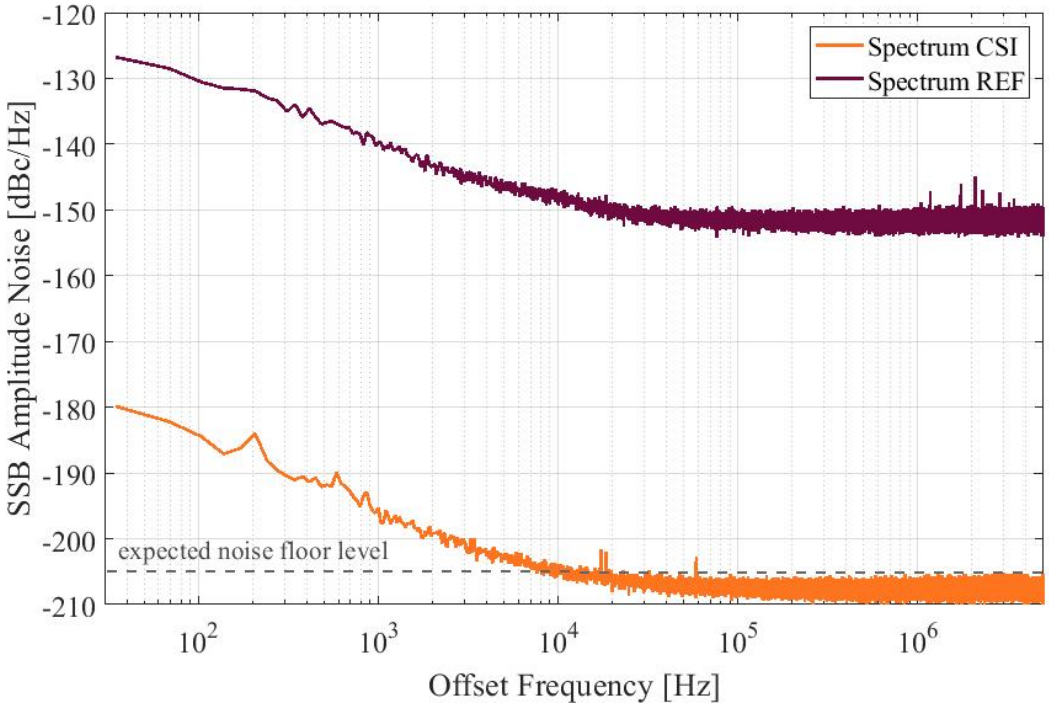

Figure 3.23: Preliminary amplitude noise measurement of the CSI itself in comparison to the standard LLRF measurement.

amplitude noise. If the REF channel is attenuated by 10 dB in comparison to the specified input power, the complex data is equally distributed again. This condition might help to keep the down-converter in linear operation but results in a wrong amplitude detection as the signal level is then too low. For further precise AN measurements this issue has to be solved.

Taking this into account, Figure 3.23 shows the achieved measurement result of the amplitude noise performance of the CSI without a DUT, representing the system performance. The measurement results are similar to the PN measurement results presented in Section 3.4.3. Despite the mentioned uncertainties introduced by the calibration routine, this measurement is still within the physical limits considering the combination of noise powers for amplitude and phase noise measurements taken under the same conditions. Still, for white noise measurements obtained under the same setup configurations, there is no explanation for a difference of 3 dB between phase and amplitude noise. If one takes a look at the white noise floor of the LLRF-system in this measurement, a drop by around 3 dB compared to the PN measurement floor exists as well. It has not been further investigated, where this

deviation in the LLRF-system channel comes from, but this task will be crucial for future work.

Nevertheless, the general calibration fits to commercial systems as shown in Section 3.3. This mismatch of fitting calibration result and partially non-physical noise floor has to be investigated in detail. Still, besides this 3 dB uncertainty, the characteristic of the noise floor for AN measurements is confirmed and represents an unrivaled low-noise amplitude detection result.

3.4.5 Observations and Limitations

This section outlines relevant observations made during the course of optimizing the CSI setup, regarding systematic influences from, e.g., the signal source, signal power levels, and the post-processing system.

Influence of the Signal Source and the Input Power Level

As discussed earlier, the main limitation of the CSI noise floor currently is the input signal power and associated constraints. A further increase of the signal power leads to the following consequences. Firstly, to increase the input signal power, one needs to exchange the amplifier between the signal source and the CSI to amplify the signal from the main oscillator even further. This amplifier needs to have a high gain while having a reasonably high compression point. Additionally, the amplifier is required to be in low-noise operation. Secondly, the selection of devices used for this setup needs to be adjusted for signal powers above 40 dBm for increasing the signal power level further. Changing the carefully chosen and characterized set of components, which for these highly precise measurements and the so far presented values are mainly mechanical, can degrade the result. As explained in Section 3.4.3, it is not fully understood yet, where the remaining 1/f-noise shown in Figure 3.21 comes from. In case it stems from the noise inside of the actuators that are used for signal adjustments to yield high carrier suppression, this is indeed a final limitation for the CSI without correlation techniques. Thirdly, with increasing signal power, the sensitivity of the carrier suppression increases as well. Reaching and keeping the carrier suppression becomes more challenging with higher input signal power, such that a more sensitive and fast reacting automatization is required for the adjustment of the CSI components.

A thorough investigation on the dependence of the output spectra on the noise of the source signal has been carried out to determine its performance impact. To test the CSI spectrum quality when the source signal is noise-afflicted, an AN- or

respectively PN-modulated offset signal is injected into the CSI. As noted in Section 3.3.1, the two-coupler-modulation unit is used to implement the frequency peak either in AN or in PN. The modulation amplitude is chosen such that the frequency peak in either the AN- or PN-spectrum is above the associated spectrum of the signal source and measured in parallel on an SSA, with a modulation frequency of 500 Hz. The phase and amplitude noise performance of the source signal are shown in Figure 3.24.

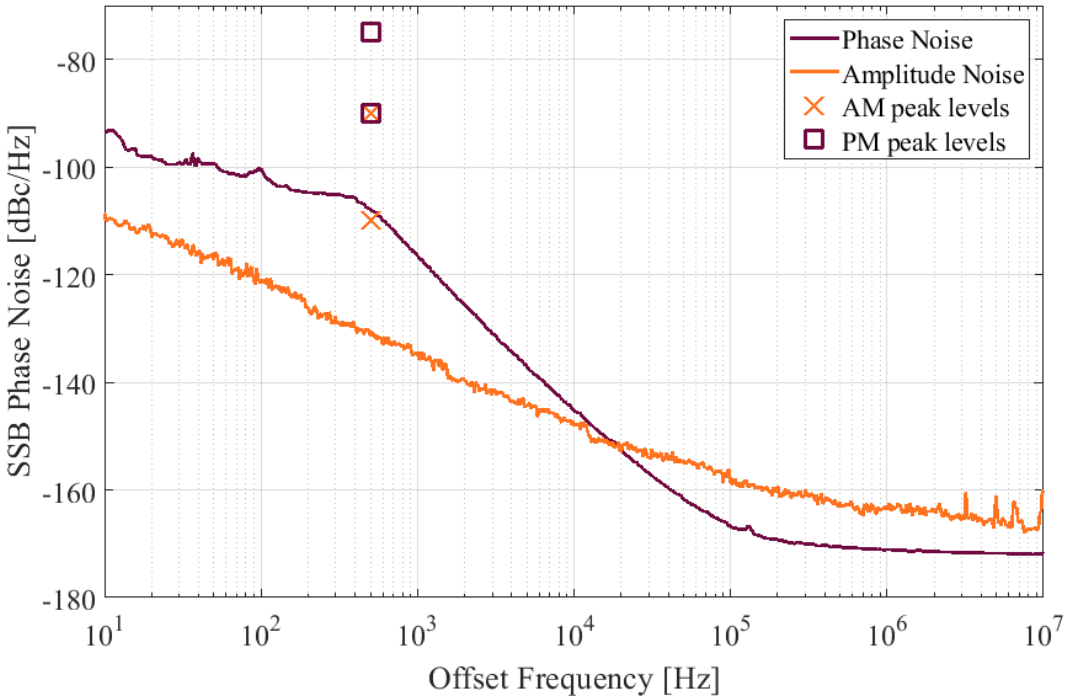

Figure 3.24: AN and PN spectrum of the main signal source, measured with commercial noise analyzers. The markers represent the measured modulation peak levels for phase and amplitude at 500 Hz, which have been introduced to investigate the influence of the reference source's noise on the CSI measurement results.

Figure 3.25(a) shows the phase noise spectra at two power levels for an injected phase-modulated signal while Figure 3.25(b) shows the same for an amplitude-modulated signal at two different power levels. In Figure 3.25(a) the injected phase modulations are chosen at −90 dBm and −75 dBm. While both values are above

the phase noise floor shown in Figure 3.24, for the peak level of −90 dBm there still is no change visible in the spectrum. For the modulation peak level of −75 dBm a small increase around 500 Hz offset frequency is detectable. The observations are similar in case of the injected amplitude modulation. Close to the AN spectrum of the main oscillator with a measured amplitude modulation level of −110 dBm no change in the spectrum is visible. For a higher modulation peak level of −90 dBm an increase is clearly visible.

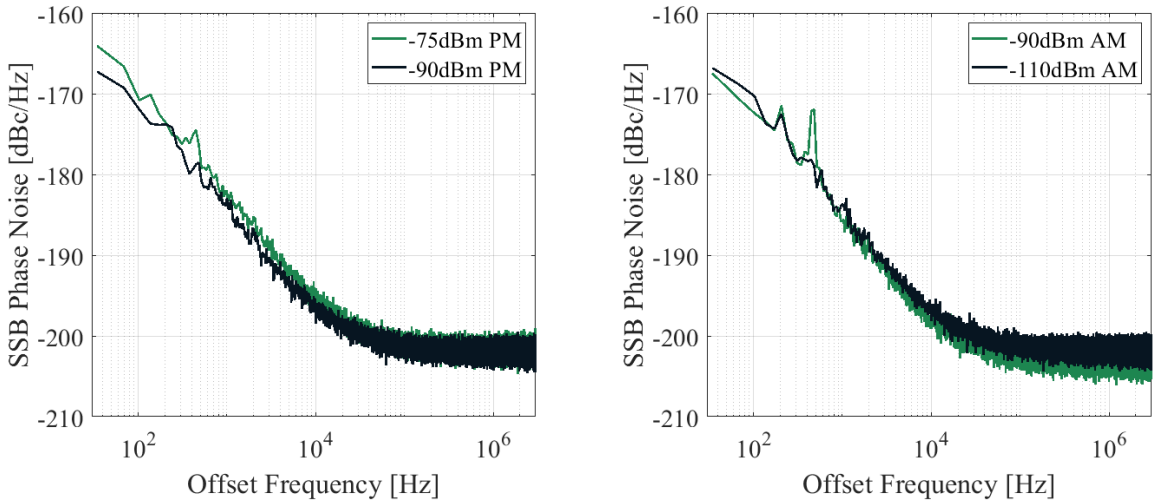

(a) Influence for PN modulation.

(b) Influence for AN modulation.

Figure 3.25: CSI measurement results for the transport of artificially modulated main signals through the interferometric structure.

With this experiment the influence of the used signal source noise characteristics is excluded. It shows the rough limits that need to be satisfied by a source signal in order to not negatively influence the measurement results. From the theory derived in Section 3.2, the noise behavior of the signal source is negligible, but by measurements and observations a connection was found, which is yet to be investigated in detail. Obviously, these results and limits may change if the setup improves or changes significantly in future work.

Influence of the Carrier Suppression Quality

The stability and the quality of the carrier suppression are crucial for the CSI measurements. As discussed, the measurement takes about two minutes, which is enough time for components to drift, e.g., due to environmental influences. The most easily disturbed and sensitive component is found out to be the continuously adjustable attenuator. As shown and discussed earlier in this section, a similar effect can be observed with increasing signal power as the suppression stability becomes even more sensitive.

Influence of the Post-IQ-Detection System

The higher the input signal power is, the more sensitive does the carrier suppression react, the more complicated the suppression tracking without an automatization gets. As the carrier suppression level degrades over the measurement duration of roughly two minutes, it is likely that the suppression reaches a threshold where the suppression levels affect the measurement results. To investigate this threshold on the post-processing system, a fraction of the signal is fed to the post-processing system instead of the CSI signal. Figure 3.26 shows an excerpt from the overall block diagram for guidance. This partial signal is limited by fixed attenuators to reasonable power levels comparable to the usual signal levels after suppression (tap point B) and re-amplification (tap point A). Figure 3.27 shows the measured single

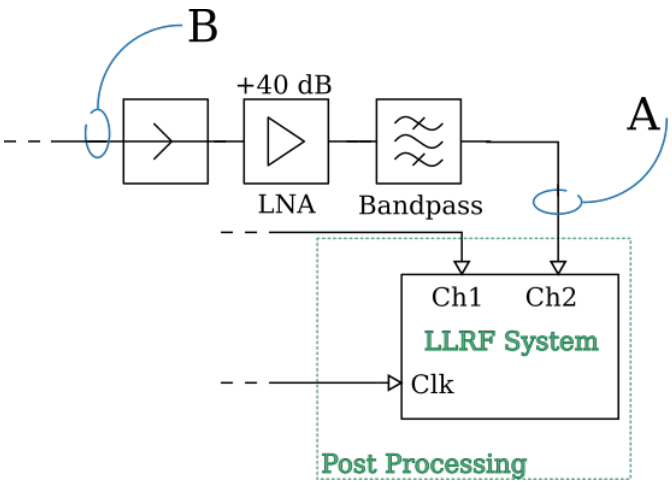

Figure 3.26: Excerpt taken from Figure 3.4.

sideband phase noise for an increased signal power starting from −20 dBm up to 0 dBm input power, measured at A, to the input channel of the LLRF-system. The figure's legend states the signal power levels being incident on the LNA (power gain of approx. 40 dB), at tap point B. Having a closer look at the region below a 1 kHz offset frequency in the spectrum, a steep edge rises when the signal power increases. To ensure that the remaining noise contribution does not arise from the performance of the LNA, the same measurement is performed by feeding the fractional signal in the LNA before sending it to the LLRF-system at corresponding signal power. No changes are visible in the resulting curve.

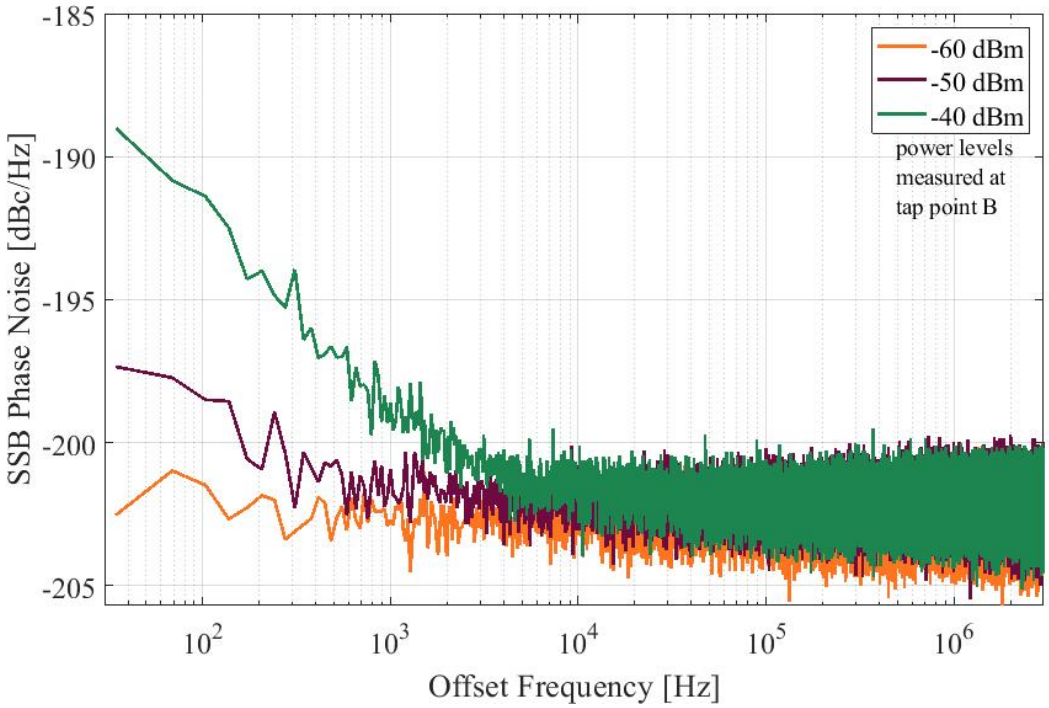

Figure 3.27: Change of spectrum depending on the input power to the signal channel of the post-processing system. The incident signal levels are measured at tap point B.

These results lead to constraints for the carrier suppression quality: The suppressed and amplified signal has to be kept below −30 dBm after the amplification by the LNA by 40 dB, denoted with A in Figure 3.26. This value corresponds

to a signal suppression of roughly 100 dB, assuming a signal power inside of the interferometer of about 30 dBm.

For increasing input power, the slope and the behavior match better and better the phase noise performance curve of the post-processing system, as shown previously in Figure 3.21. The rising slope below 10 kHz offset frequency can be assumed to be the influence of the downconverting mixer as the first stage of the post-processing system. As the signal power through the mixer or the ADC in the post-processing systems gets larger, its own noise contribution becomes visible.

Influence of Delay-Line Mismatches

When the setup is adjusted to a high input signal power of 38 dBm, additional disturbances become visible scaling with gain in measurement resolution. The disturbances can mostly be traced back to their origin, though one was always present at an offset frequency of around 1 MHz and above. It seemed independent of input power, considered DUT or other involved components. After some research, the rise in the spectrum could be traced back, as in the frequency discriminator measurement method [44], to a mismatch between the electrical lengths of the two suppression arms. One of the arms includes a mechanical 360° phase shifter and carries the main signal power, such that the influence of the arm is tremendous. The single sideband noise is shown before and after length adjustment in Figure 3.28.

Although the physical length of a transmission line can be expressed as a change in phase for a certain frequency, this translation does not hold for any other frequency. This mismatch causes the distortion of frequency components for offset frequencies around 1 MHz and above, such that these frequency components are not cancelled out as they are for lower offset frequencies. Phrased in attoseconds of timing jitter, the mismatch diminishes the result by 3 as in the frequency band of interest. This effect is avoidable by carefully matching the electrical length in the measurement setup [65]. Having a DUT changing in phase, one either needs to accept the slight mismatch for higher offset frequencies or needs to adjust the electrical length in the parallel path accordingly.

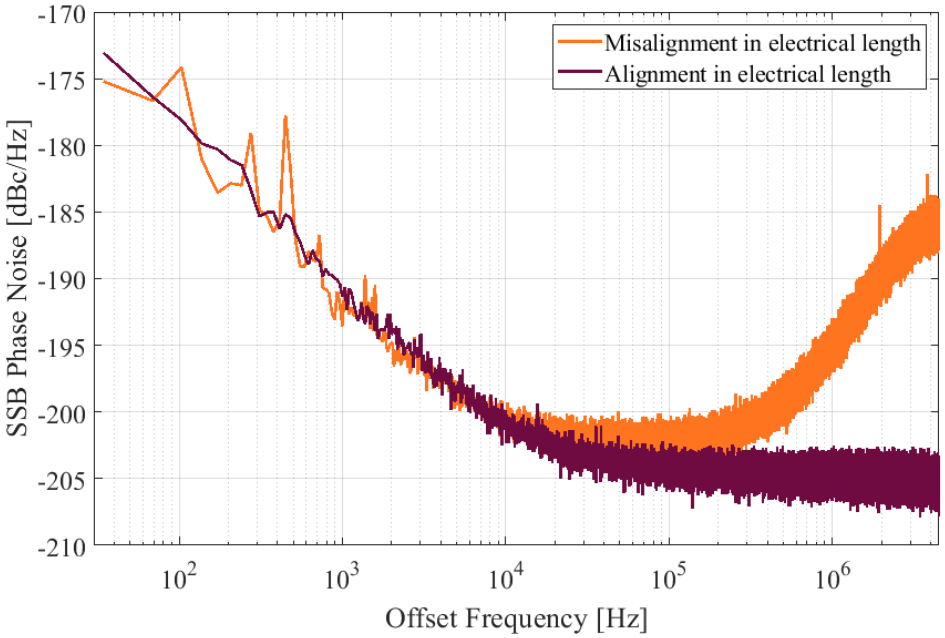

Figure 3.28: Change of spectrum depending on the mismatch of the electrical length inside of the suppression paths.

4 Applications of the Carrier Suppression Interferometer

Comparing the achievements reported so far with the initial motivation and intention for this project for DESY, one aspect is yet missing: the application of the CSI in an actual accelerator facility. For the presented setup, the most compatible actuator devices are required to accomplish the suppression in an automated manner. In order to find such components, the CSI is of great help to characterize possible suitable modules, that fit to the demanding low-noise performance requirements and was extensively used for this purpose. This investigation itself was extremely engaging and even sparked much interest to understand more how to improve commercial actuators and explore noise differences from varying materials and device function mechanisms. Applications of the CSI therefore cover two fields: in Section 4.1 the application of the CSI as a high precision phase- and amplitude-analyzer is discussed and ongoing in Section 4.2 the main results of a component and material research for future compact and automated actuators for the CSI are presented. Afterwards, Section 4.3 gives a brief overview on how to combine the presented laboratory setup with the control system of a real accelerator research facility at DESY.

4.1 Phase- and Amplitude-Noise Analyzer

Understanding noise and especially 1/f-noise in RF components and materials emerged as a highly active research field over the last century and still is one today. The most important terms in the context of this work are discussed in Section 2.1. W. Schottky published already in 1918 his work on spontaneous fluctuations in current signals, when passing materials and gas-filled components [66]. Multiple models on the emergence of 1/f-noise have been suggested, with more or less successful matching to measurement results. While its origin is still not fully understood, one can assume that it is to a large extent introduced by imperfections

in conducting materials and the charge carrier movements, either as effects inside of materials or on their surfaces [28], [67], [68].

To measure these noise effects high precision noise evaluation devices are available on the market. Most of the devices work similarly to the LLRF-system by means of downconverting the noisy signal to an intermediate or even baseband frequency. As these systems are limited in resolution due to the selected mixing structures inside the front-end, they often have the possibility to calculate cross-correlated output signals. The possibility of calculating cross-correlated results cancels those noise leftovers which are systemic [69].

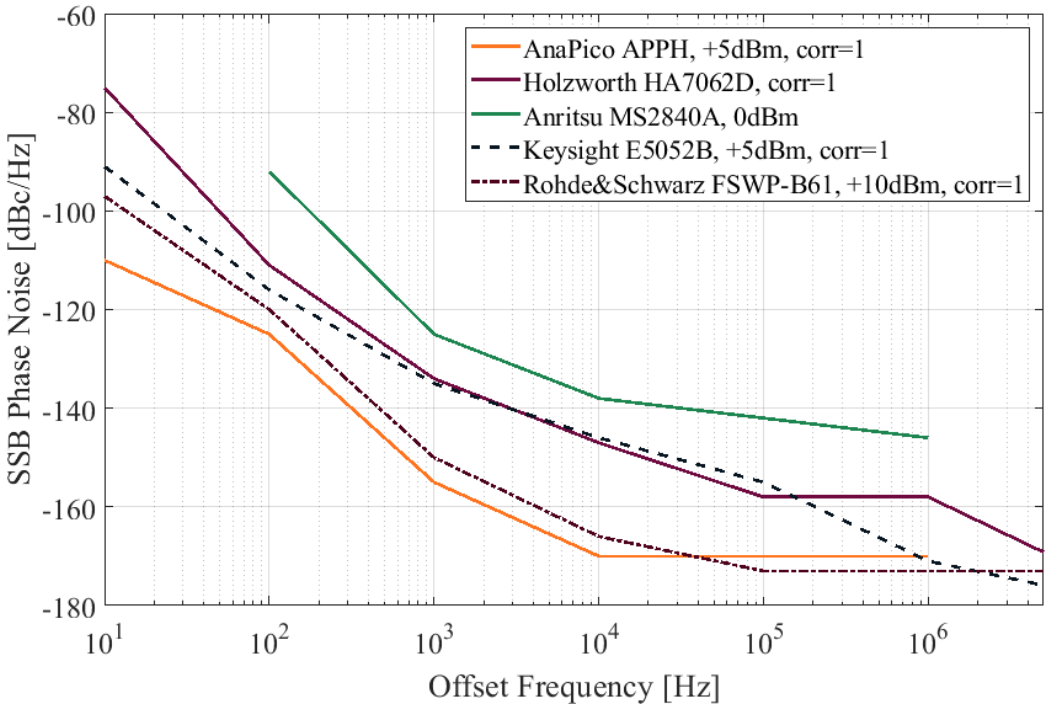

Figure 4.1: Comparison of commercial phase noise evaluation systems. The evaluated carrier frequency is 1 GHz. The signal power varies from 0 dBm to 10 dBm, as is noted in the legend, wherever the value was provided in the data sheet. Apart from the signal analyzer MS2804A from Anritsu, all devices calculate the correlation of two channels (with the correlation factor of one) and thus mitigate their system noise contributions.

Figure 4.1 shows a selection of the noise floors of different state-of-the-art commercial phase noise analyzers [60], [70]–[73]. The plotted data is taken from data sheets and is measured with a carrier frequency of 1 GHz, which is sufficiently close to the nominal operating frequency of the CSI of 1.3 GHz. Data of uncorrelated single-channel measurements is shown wherever possible. Where this is not possible, the smallest available correlation factor is chosen, which already reduces the system noise as this nevertheless implies a dual-channel mode. The given data is only available for certain power levels, which directly influences the spectral noise level. Adapting the data curves to equal input power levels, the APPH from AnaPico would be leading with the lowest noise floor. As the commercial phase noise detectors are designed for a higher bandwidth and include multiple operation modes, the resolution in the close-to-the-carrier region suffers often and noise detection within this area is strongly limited. The CSI however is designed with emphasis around the main operating frequency of interest for specific superconducting particle accelerator applications at 1.3 GHz, but at this frequency it offers a very high detection resolution, even close to the carrier and without the application of time consuming correlation techniques. Even without the usage of cross-correlation techniques, the CSI offers unrivaled noise resolutions and is therefore most suitable for the investigation and characterization of noisy components for later application in the accelerator's RF detector front-end [65].

4.2 Results of the Device Characterization

Downsizing the CSI without worsening its performance is necessary to enable automated operation at the DESY accelerator facilities. This requires the accurate identification of suitable components. Most of the commercial noise test system are not precise enough for this purpose, as can be seen in the comparison shown in Figure 4.1. Especially close to the carrier the spectral resolution is simply too low, while this area is of particular importance for our development purposes, such that the CSI becomes the measurement setup of choice.

In contrast to Section 3.4.3, where the DUT was replaced by a coaxial cable in order to identify the system noise performance itself, for the following results actual DUTs are measured and evaluated. As shown in Section 3.1 in Figure 3.4, the DUT is placed inside the coarse suppression circuit and before the signal is split into the paths with and without suppression. Thus, both signals should ideally include the same noise signal information from the DUT before the carrier signal is cancelled.

Within this section a selection of various RF components is introduced and characterized as DUTs. The presented components are typically used for the design of phase shifters and attenuators. The selection is accompanied with first hints to possible explanations found during the research. To measure and characterize likely suitable actuators, the CSI in its mechanical form is used as shown in Figure 4.2. The idea is, that over time the system characterizes components, which - if considered beneficial - replace current components that are not suitable for automated operation. This exchange of actuators is supported by the aluminum box in the center, which includes the signal splitting and combining circuitry. The DUT, which obviously is an outside component, is exemplarily shown in the marked area in Figure 4.2.

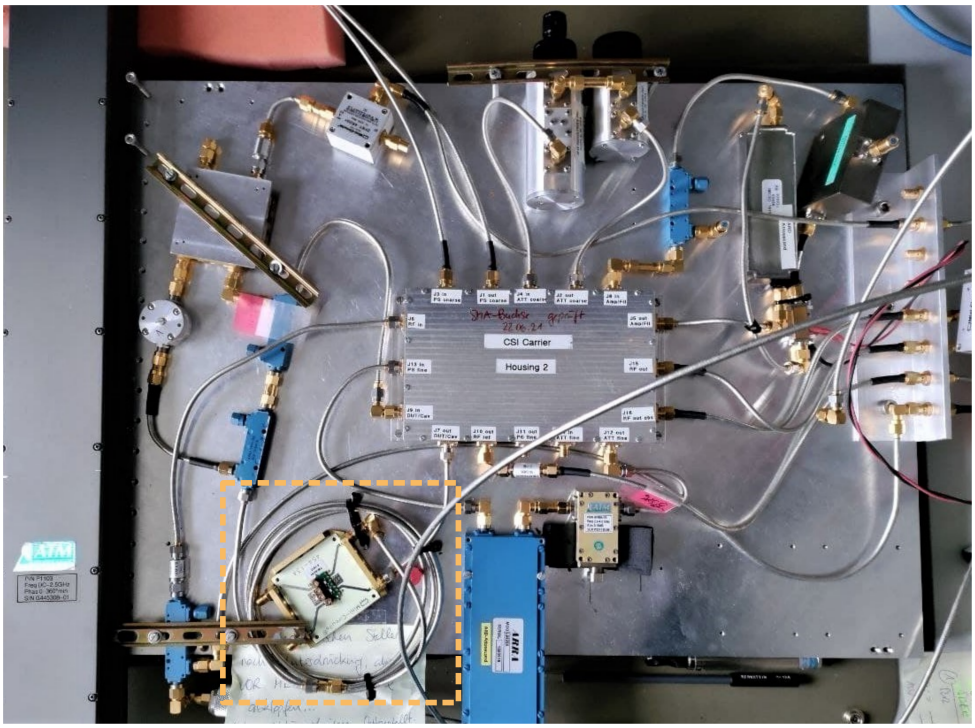

Figure 4.2: CSI setup configuration with mechanical components used for the presented device characterizations, with space left to place a DUT marked by the orange dashed square.

A variety of test boards and components has been measured with the CSI within the scope of this work. A few examples are shown in Figure 4.3. Starting with commercial devices, the research moved further and further towards own

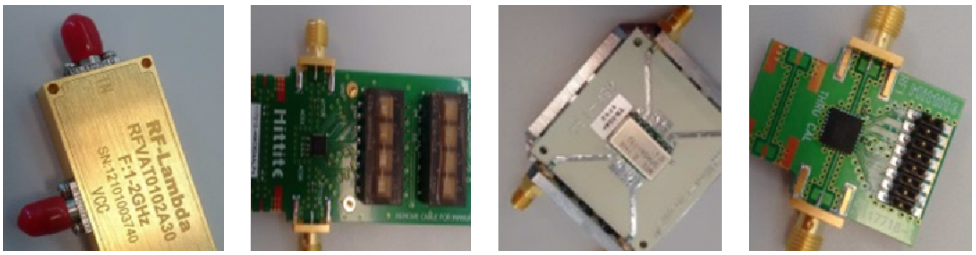

Figure 4.3: Examples of commercial phase shifters and attenuators.

and improved designs. After thorough analysis of state-of-the-art electric phase shifters, which are found to be not fully sufficient, it was decided to custom-build and optimize. As the characterization of such devices has shown certain technologies and types being generally promising, electric phase shifters were designed accordingly, combining suitable topologies and components, overall optimized for the applications of interest.

4.2.1 Voltage-Controlled Devices

One major concern connected to using voltage-controlled devices is the allocation of very low-noise bias voltages. In the case that the control voltage is in direct contact to, e.g., the semiconductor device, it is very likely that the voltage fluctuations of the power supply become visible in the resulting noise spectrum by up-conversion from baseband. For very low noise powers the noise introduced by the power supply even dominates. To overcome this issue, a battery voltage was supplied in order to provide clean as possible bias voltage [74]. Of course, not every DUT can be driven by a battery package and the discharging adds drifts to the CSI, but for low-powered devices this is a rather practical solution. For the compactification of the CSI setup the power supply is a problematic design aspect, requiring a careful trade-off between possible solutions, as for instance voltage filtering enables only slow voltage changes, but might be too slow to keep the carrier suppressed and stable within a control loop. Various power supplies have been used in the course of this investigation, but none of them was low-noise enough to bias the phase shifters during phase noise measurements without dominating them.

Varactor Diodes

Varactor diodes are some of the most commonly used semiconductor devices when designing phase shifters or attenuators. A varactor diode consists of a (most of the

time) reversely biased pn-semiconductor-junction and exhibits a changing junction capacitance C_j over the control voltage V_bias within the depletion region with

$$C_\mathrm{j}(V_\mathrm{bias}) = \frac{C_0}{\left(1 - \frac{V_\mathrm{bias}}{V_0}\right)^\gamma}. \tag{4.1}$$

C_0 is the junction capacitance without biasing voltage. V_0 depends on the diode material and is given by experiments with $V_0 \approx 0.5\,\mathrm{V}$ for silicon diodes, and $V_0 \approx 1.3\,\mathrm{V}$ for gallium-arsenide diodes. The exponent γ depends on the doping profile of the diode [46], [75]. The type of doping profile is split into two categories: abrupt junction and hyperabrupt junction, but in general the averaged value for γ lies between 0.47 to 0.5.

This C-V-relation enables compact designs of reflective voltage-controlled phase shifter or attenuators. It is therefore also advantageous for the overall objective of miniaturizing the CSI. On the other hand, the existence of intrinsic noise processes in semiconductors cannot be denied. Whenever a current passes materials or semiconductor barriers, there is necessarily also a noise contribution. Especially for semiconductor junctions as in diodes, the noise in low-frequency regimes is dominated by charge carrier mobility and recombination processes [34], [35], [67], [76]–[80]. This kind of noise follows a 1/f-behavior, as introduced in Section 2.1.

The major part of the investigated phase shifters are based on varactor diodes. Although Schottky diodes are predicted to have a lower intrinsic noise, only a few have been evaluated. Schottky diodes have a metal-semiconductor junction and by this a lower capacitance range for varying bias voltages. In comparison to pn-junctions, 1/f-noise in Schottky diodes is dominated by surface and edge effects, which can be reduced by proper design and manufacturing [37], [81]. There are many approaches to describe the low-frequency noise in Schottky diodes [82], [83], but as the junction capacitance is notably smaller compared to the one in varactor diodes it is not the first choice in diodes for actuator designs.

The main problem with varactor diodes is the increasing noise contribution for increasing bias voltages V_bias. Many phase shifters have been evaluated within the scope of this work, either off-the-shelf or self-designed. Still, as the diode's capacitance depends on the bias voltage, the phase shift depends on it, as well. A clear tendency to higher noise levels for higher biasing was observed for many of the evaluated phase shifters and diodes. A measurement series for an off-the-shelf phase shifter is shown in Figure 4.4. The bias voltage was supplied by a battery module and increased stepwise from 0 V to 15 V, which corresponds to the maximum allowed bias voltage. The noise from the battery module could be excluded from being

the trigger of the measured noise behavior. In comparison to the noise increase in Figure 4.4 for rising bias voltage, the measurement of different phase shifters of same technology biased by this battery module shows varying noise behaviors (cf. Figure 4.7).

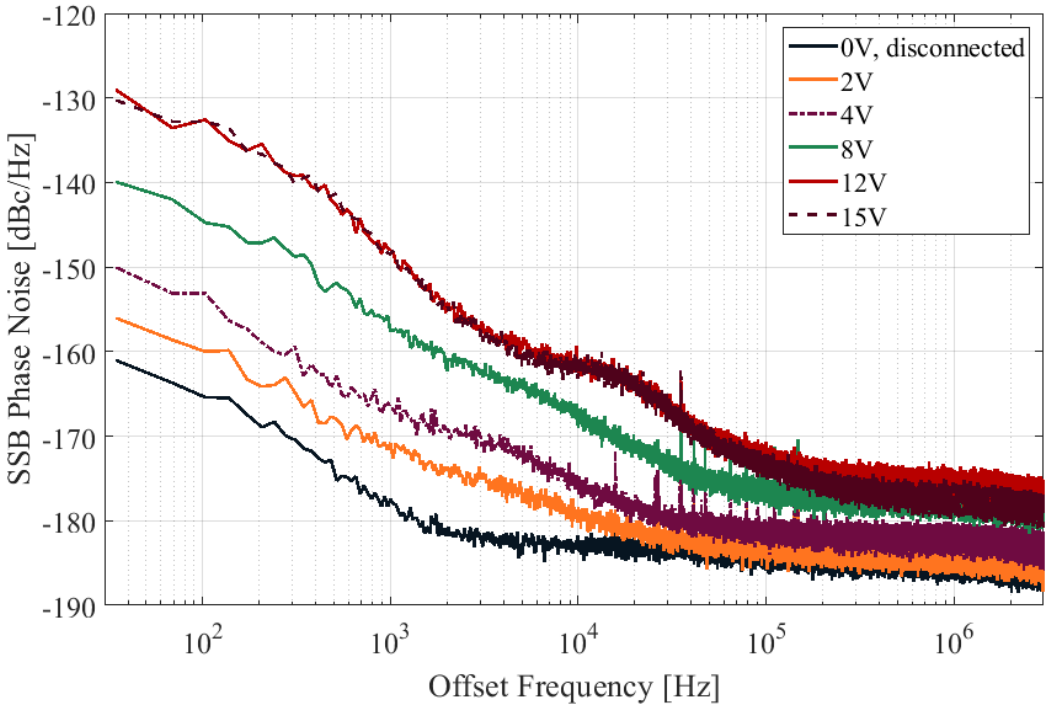

Figure 4.4: Exemplary study of the relationship between bias voltage and phase noise for a commercial diode-based phase shifter.

To see the actual noise performance of a certain varactor diode one has to measure it, as common datasheets do not offer sufficient information on the noise behavior. Only a few companies market their varactor diodes explicitly as "low-noise", and those that do are not giving appropriate numbers or measurement results in a way that is useful within the scope of this work. Common parameters to be found in the datasheet are the capacitance range or ratio, the maximum bias voltage, the package size, the temperature dependence, and sometimes the unspecified serial resistance. There is one factor regarding diodes, which combines main parameters given in data sheets: the quality factor Q. Still, regarding phase noise it is not clear, if the quality factor Q is a promising indicator for predicting whether the

diode is very noisy or as noise-less as it can be and may be used for further CSI developments. Since the quality factor is defined as

$$Q = \frac{f_0}{B_{3\,\mathrm{dB}}}, \tag{4.2}$$

Q describes the relation between the carrier frequency f_0 and the 3 dB-bandwidth $B_{3\,\mathrm{dB}}$, denoting where the power has dropped by 3 dB [84]. This can be seen as an estimate for the steepness of the slope around the carrier frequency. Not all companies offer the quality factor in the data sheet for their diodes.

The equivalent circuit for a varactor diode reversely biased for small-signal operation is given in Figure 4.5 [46]. The quality factor Q for such circuits can be

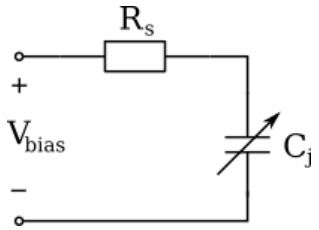

Figure 4.5: Simplified small-signal circuit for a varactor diode in reverse bias with the junction capacitance C_j and the series resistance R_s, which includes the bulk resistance of the pn-junction and resistances from the metal-semiconductor contact.

described by

$$Q = \frac{|\mathrm{Im}\{Z\}|}{\mathrm{Re}\{Z\}}, \tag{4.3}$$

with the impedance of the circuit Z [76]. For the circuit in Figure 4.5 the impedance is given by

$$Z_\mathrm{varactor} = R_\mathrm{s} + \frac{1}{j\omega_0 C_\mathrm{j}}. \tag{4.4}$$

Together with Equation 4.1 and $\omega_0 = 2\pi f_0$ this leads to a relationship for the varactor diode quality factor

$$Q_\mathrm{varactor} = \frac{1}{\omega_0 R_\mathrm{s} C_\mathrm{j}} = \frac{\left(1 - \frac{V_\mathrm{bias}}{V_0}\right)^\gamma}{2\pi f_0 R_\mathrm{s} C_0}. \tag{4.5}$$

This ideal definition includes the dependence of the varactor's behavior on the bias voltage, the material, and the internal resistances. Luckily, these are some of the standardized parameters regularly given in data sheets. Even if the parameters for the capacitance range might be evaluated at other frequencies than the operating frequency, one can co-opt this value, as the capacitance C_0 is nearly frequency-independent for low- and mid-range-frequencies [85].

Table 4.1 gives some examples of evaluated commercial varactor diodes [75], [86]. The quality factors are evaluated according to Equation 4.1 at a frequency of 1.3 GHz for different bias voltage levels. With Equation 4.1 and 4.5, Q_{min} and Q_{max} refer to the quality factor for the highest or lowest bias voltage, respectively, independent of design constraints of these provided voltages. For all calculated Q values only capacitances in the range between C_{min} and C_{max} given by the properties of the diode are considered. The table entry "Q at $V_{\text{bias, max}}$" shows the quality factor for the by design highest permitted voltage bias. Due to the requirement of clean bias voltages, a battery module limited to 17 V is used to provide the supply voltage. This causes the difference in the quality factors between the allowed maximum voltage from the data sheet and the actual applied maximum voltage. For further measurements, as the diodes have different fundamental capacitances C_0, the voltage bias is adjusted such that every diode has a junction capacitance of 5 pF.

Diode/Property	SMV1247	SMV1413	SMV2026	BB833
R_{s} in Ω	6	0.35	0.5	1.8
C_{min} in pF	0.64	1.77	3.01	0.75
C_{max} in pF	8.86	9.24	27.09	9.3
Q_{max}	32	198	81	90
Q at $V_{\text{bias, max}}$	32	160	81	75
Q_{min}	2	38	9	7
Q at $C = 5\,\text{pF}$	4	70	49	14

Table 4.1: Examples for commercial varactor diodes. R_{s}, C_{min}, and C_{max} taken from corresponding data sheets.

To be able to compare these diodes at high frequency operation, the diodes are implemented inside an - for all diodes identical - reflective phase shifter design as

outlined in the beginning of this chapter. For the sake of completeness, Figure 4.6 shows the used phase shifter design printed on RO4350B substrate [64].

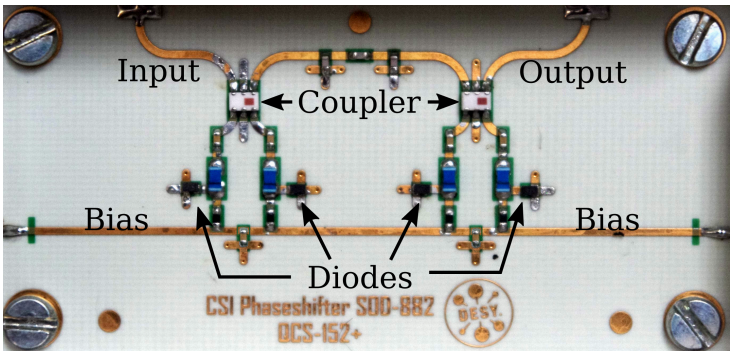

Figure 4.6: PCB of the reflective phase shifter design used for the diode investigation [65].

Based on the calculations and results in Table 4.1, a reasonable assumption is that the varactor diode SMV1413 should show the best result for any bias voltage.

The corresponding measurements for each diode type can be found in Figures 4.7(a), 4.7(b), and 4.7(c). Comparing the measurements for all three conditions, differences in the measured power levels are visible. These are mainly caused by network mismatches by changing the capacitance and resulting signal losses. Regarding the noise contributions, the diode BB833 shows a more or less constant noise behavior throughout the applied bias voltages. The diodes SMV1413 and SMV1247 are noisy for very low bias voltages V_{bias} and offset frequencies below 100 kHz. Fitting the curves in mind for compensation of the measured power levels and thereby power losses, the difference in the noise contribution is similar for the diodes BB833, SMV1247, and SMV1413. The lowest noise performances up to bias voltages of above 10 V are reported for diode SMV2026. Comparing the provided junction capacitance ranges of the mentioned diodes, the diode SMV1247 is leading, followed by BB833 and SMV2026. This is in agreement with the phase range measurements of each phase shifter based on the specific diode. Although, the quality factor of SMV1413 is the highest for maximum, medium, and lowest bias voltage, it has the weakest change in capacitance across the bias voltages. As this refers to the available phase shift range, this diode is less favorable for phase shifting. In addition, contrary to the promising high quality factor of this diode, it is far noisier than can be assumed from the low serial resistance.

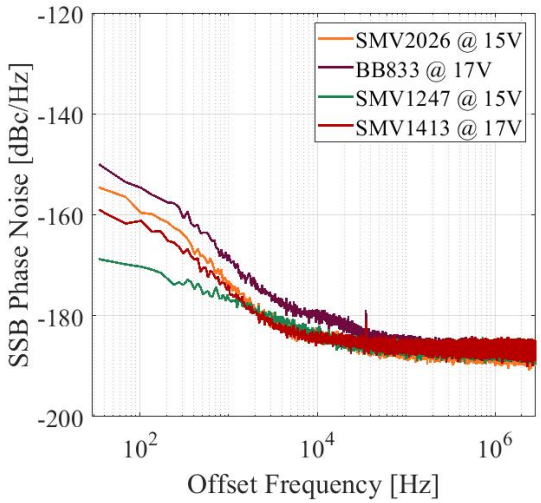

(a) Phase Noise Spectra for $V_{\text{bias}} = \max \triangleq Q_{\min}$.

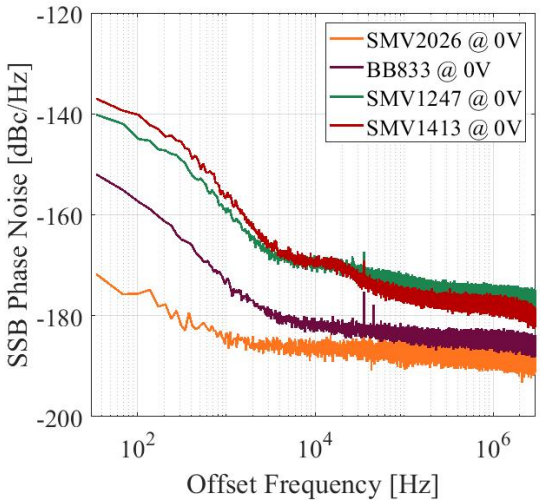

(b) Phase Noise Spectra for $V_{\text{bias}} = 0 \triangleq Q_{\max}$

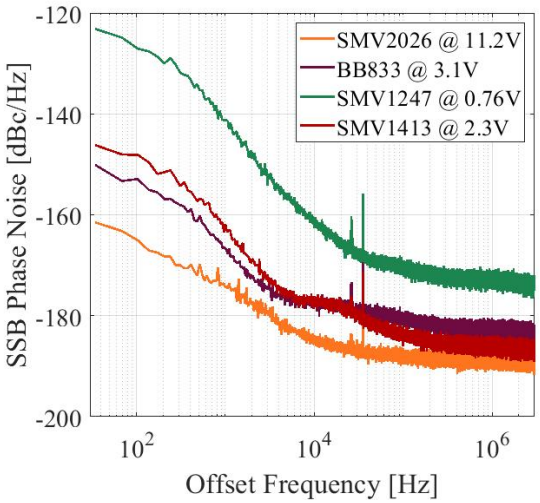

(c) Phase Noise Spectra for $V_{\text{bias}} \triangleq Q_{[5\,\text{pF}]}$

Figure 4.7: Evaluation of different diodes in terms of Q.

Even though the quality factor is a common parameter to represent the noise behavior for many components, e.g., oscillators, and it generally gives a reasonable idea of the quality of resonance, its informative value has shown to be limited in the context of noise contributions of varactor diodes at very low noise levels. When asking companies for low-noise diodes, they often refer to diodes with very small series resistances R_s, where R_s sums up the bulk resistance R_b and resistances from the metal-semiconductor contact. While this in general is not wrong, as the series resistance R_s directly contributes to thermal and excess noise, it does not seem to represent the dominant noise contributors when R_s is very small, and overall is too much of an integrated quantity to fulfill the specific needs of this investigation. Also, in the data sheets there is usually no reference given on the determination of the value R_s. It might be a simulation product, measurements under varying conditions, a different packaging type, or something entirely different, which leads to a rather ambiguous metric. As all common parameters given in typical commercial data sheets do not support reliable predictions, all the better the CSI exposes even the weakest noise signals to characterize these diodes.

Diode Selection

For the characterization of the varactor diodes in phase shifters one observation stands out: When exchanging the set of the required four varactor diodes in the phase shifter by another set of four diodes of the same type and the same packaging size, reproducible, but significantly differing phase noise curves are seen. Figure 4.8 shows the measurement of a phase shifter, identical except for the set of diodes, although they are from the same production charge. As previously discussed, this is a very low-noise diode model and the best type found during the investigations. While for many applications, this difference between both diodes sets is negligible, it is significant for the performance of the CSI. Nevertheless, it is a relevant issue that each diode shows individual properties caused by manufacturing, as soon as the interest breaks down to the design of actuators at attosecond level [87]. As a consequence, a precise selection of individual varactor diodes is unavoidable for future enhancements of receiver front-ends. If one wants to go one step further, one should also include resistors in the pre-selection, as they lack in manufacturing accuracy and therefore increase the excess noise as well [88]. Resistors are not only frequently used components for phase shifters and attenuators but also for signal splitting and coupling structures.

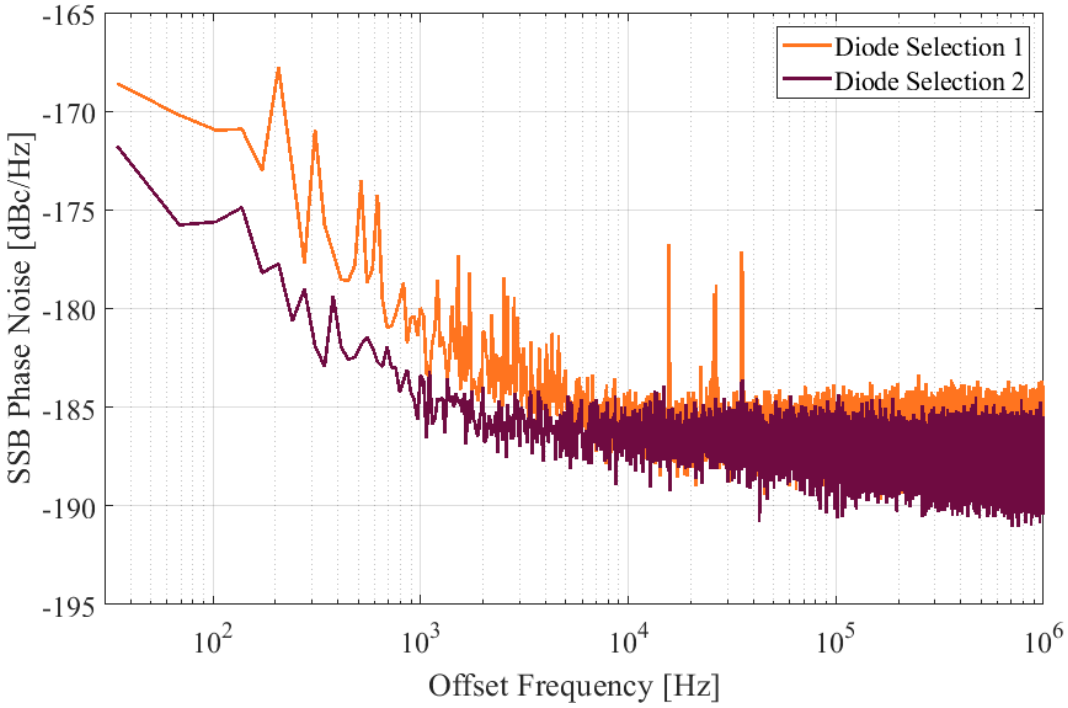

Figure 4.8: Phase noise measurement of two diode sets of four diodes each in identical phase shifter structures.

Barium Strontium Titanate Varactors

A second option for the design of a varactor is the usage of dielectric material instead of semiconductors. A material investigated in this work for dielectric varactors is barium strontium titanate (BST). In a semiconductor varactor the variable capacitance is formed by the change of the depletion region's width. For BST the capacitance is adjusted by a field strength and the polarizability of the dielectric material [89]–[91]. Very advantageous is the fact, that with BST material only a fraction of size is required to achieve similar capacitance ranges compared to semiconductor-based varactors. For the noise evaluation, commercial BST chips are used in a very similar phase shifter model as the varactor diodes [92], which can be seen in Figure 4.9. The phase noise characterizations of the tunable BST-capacitors are shown in Figure 4.10. Two chip types from the same company, but of differing capacitance ranges, are measured. The difference in the ranges influences the controllable phase range of the phase shifter. Both BST capacitors show less phase noise for higher bias voltages. According to the operation principle, a higher bias voltage results in a higher field strength on the polarizable BST lattice, so the

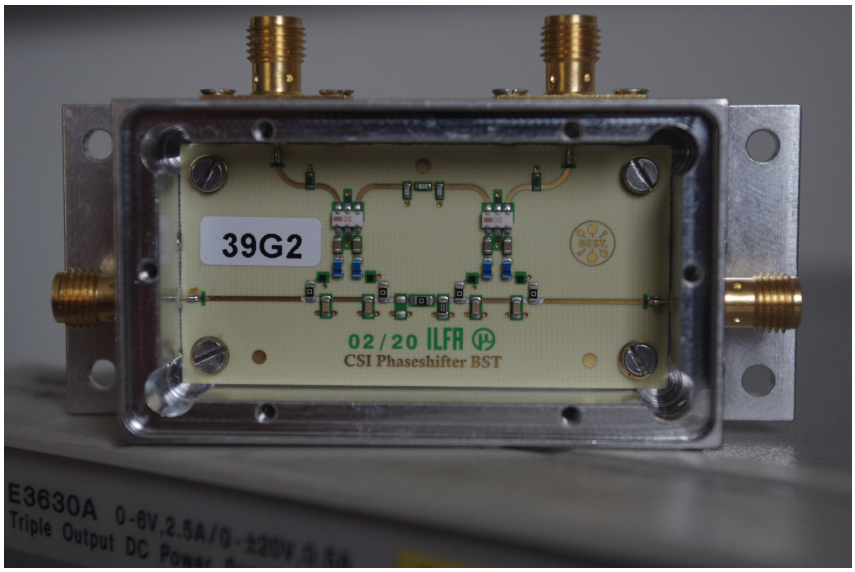

Figure 4.9: Photography of the BST-PCB.

dipoles should be orientated by a stronger force and keep their position more likely compared to lower field strengths. Referring to the measurement in Figure 4.10, there seems to exist a certain applied field strength, where the phase noise in the BST drops from higher phase noise states to lower ones. It is not clear, whether even higher bias voltages lead to the reverse behavior showing higher phase noise again. But as several measurements with the CSI have shown, the observed phase noise reduces as the field strength increases, as is shown in Figure 4.10. These curves show two different BST chips differing in the capacitance ranges for stepwise increasing bias voltages. Bias voltages of up to 17 V, provided by aforementioned battery modules, are applied at a signal power level of 20 dBm.

On the contrary, former investigations in the 2000s found a relation between quality factor Q and the phase noise contribution for voltage-controlled oscillators [89]. To have a valid comparison, the study considered two identically structured voltage-controlled oscillator (VCO), one based in a classical manner on varactor diodes, the other one using BST. For a biasing of 0 V, in agreement with the carried-out experiments, there is no current flow across the BST segment, thus resulting in no excess noise. This behavior is contrary to varactor diodes, whose undesired residue forward current stems from the RF signal swing in VCO applications. For higher voltages, the phase noise contribution is supported and increases by the degradation of the estimated decreased quality factor Q. Still, as their measurements show a different behavior than the one reported by the experimental data in this section, a revisit of the relations they found could be interesting.

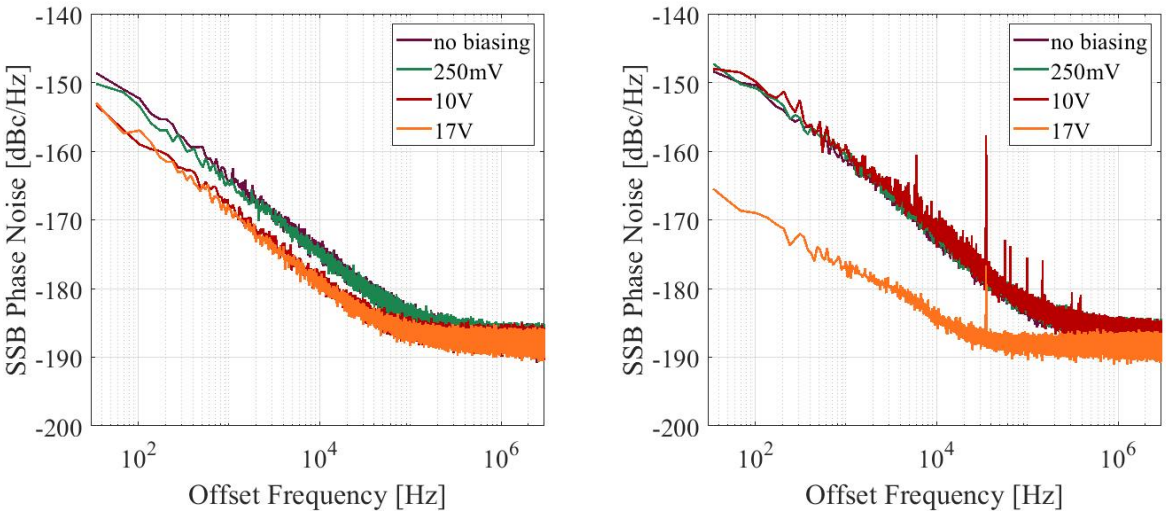

(a) BST-type: STPTIC-39. **(b)** BST-type: STPTIC-15.

Figure 4.10: Phase noise measurements of BST chips of different capacitive properties for varying bias voltages. The figures represent the results for the STPTIC-39 and the STPTIC-15 chip inside the reflective phase shifter structure.

Similar to BST in terms of being polarizable mediums are so-called liquid-crystals [91], [93]. The phase change in liquid-crystal phase shifters is related to molecular movement forced by an outer field strength. By this movement their dielectric constant is adjusted. However, liquid-crystal technology is not well suitable for applications in the CSI context. At the moment, the advantages of this technology can only be played out at higher frequencies of above 15 GHz, e.g., in the very steep gradient for phase shifts. Also, considering the high control voltage requirements at above 20 V and the high design efforts, the application of liquid-crystals for RF devices is still challenging and still under research.

RF-Switches

Another option for the design of phase shifters lies in switching from one transmission delay line to another and thereby changing the phase difference. The latest developments among industrial suppliers are miniature switches for high-power signals in the high-frequency range showing excellent isolation properties [94], [95]. As this reduction in space offers the possibility of compact phase shifter designs, the switches are characterized in terms of noise with the CSI.

For this investigation two different switch types are measured as a DUT: One switch type is based on a very small Micro-Electro-Mechanical System (MEMS) and counts as one of the first commercially available MEMS switches. The other switch type is a classical magnetic-latching relay and is one of the smallest relays currently available in this category.

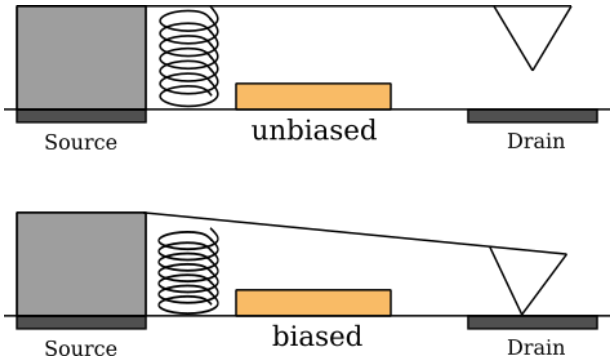

Figure 4.11: Symbolic inner structure of the MEMS inside of the ADGM1304 chip [95].

The switch type based on a MEMS is in this case a four-throw switch. The MEMS itself is a thin metal cantilever swinging above an electrode, as sketched in Figure 4.11. By activating the electrode, the cantilever is energized and closes an RF circuit [96], [97], [98]. If the gate voltage is sufficiently high (or low, depending on the design), the cantilever is pulled down, and the RF signal can pass from source to drain [99], [100]. The cantilever of this chip itself is no longer than 100 μm and not more than a half micrometer apart from the drain contact surface [99]. When the cantilever is in its resting state, several noise processes can occur [97].

In Figure 4.12 the phase noise curves for all four transmission paths of the MEMS switch are shown. The switch is inserted as a DUT into the CSI for this measurement series, as shown in Figure 3.4. A slight difference in noise between the four switching positions is visible. It seems there are two distinct states of noise contribution. As discussed in Section 3.4.3, it is not clear, whether the slight change in the noise behavior is introduced in the mechanical actuators, by contact noise or has its origin in the noise of the MEMS switches. But as the step actuators have not been adjusted between measuring the four switching positions, the difference is likely to be traced back to the switch. On the other hand, this result is not reproducible:

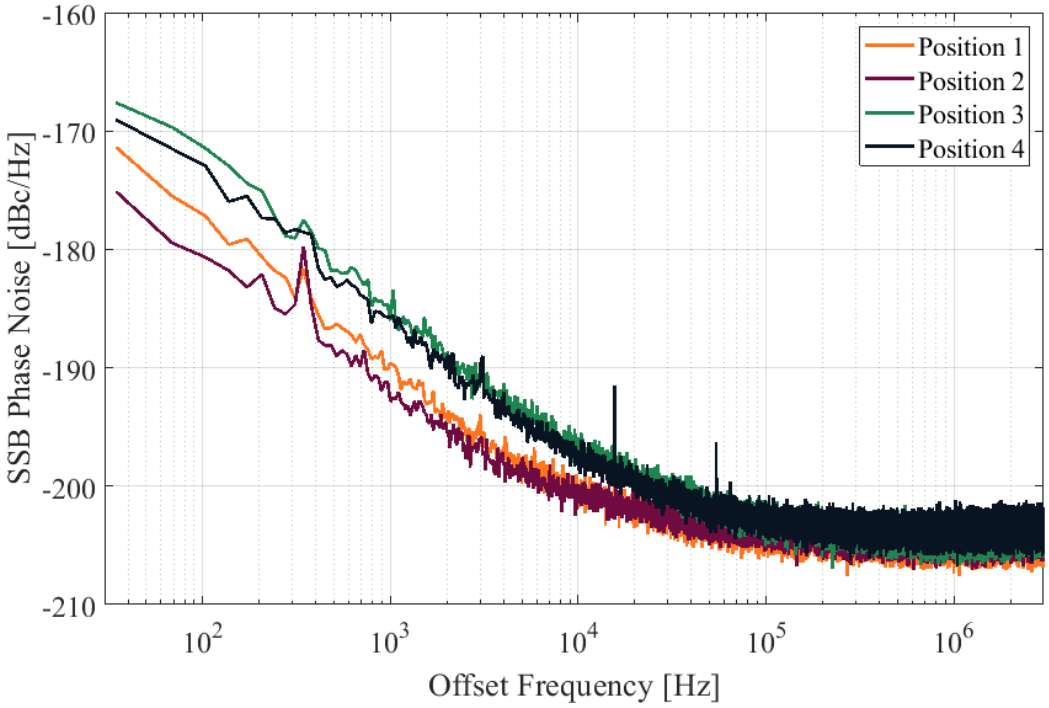

Figure 4.12: Phase noise measurement of a four-throw MEMS switch at 1.3 GHz for all four switching positions.

Neither for the same chip nor for other chips, but what remains is the split into these two states of noise contribution.

Together with Laurin AG [101], phase shifters based on both switch types were designed and realized. Figure 4.13 shows the phase shifter based on the ADGM1304-MEMS switches. Compared to only passing one switch, the signal passes eight switches in a row.

The phase noise measurement result of the MEMS phase shifter is shown in Figure 4.14. It shows a higher phase noise for passing the row of switches than for passing only one switch. According to earlier investigations on this matter [97], it is more likely to see the sum of the noise contributions of the row of switches, than the increased noise contribution by the remaining mechanical actuators inside the CSI.

From theory, the Brownian noise contribution dominates in MEMS and depends mainly on the spring constant, the damping factor and the quality factor [102]. Acoustic and acceleration noise influences may additionally be observed in this operation state. Looking into the model of the investigated MEMS chip ADGM1304, the cantilever drops in order to let the RF signal pass. Therefore, the switch is already in the lowest noise state referring to Brownian and acceleration noise. The

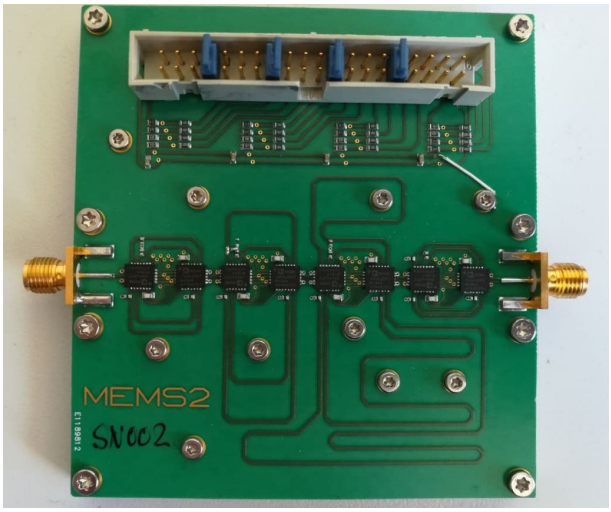

Figure 4.13: Photography of the designed MEMS-based phase shifter for 1.3 GHz [101].

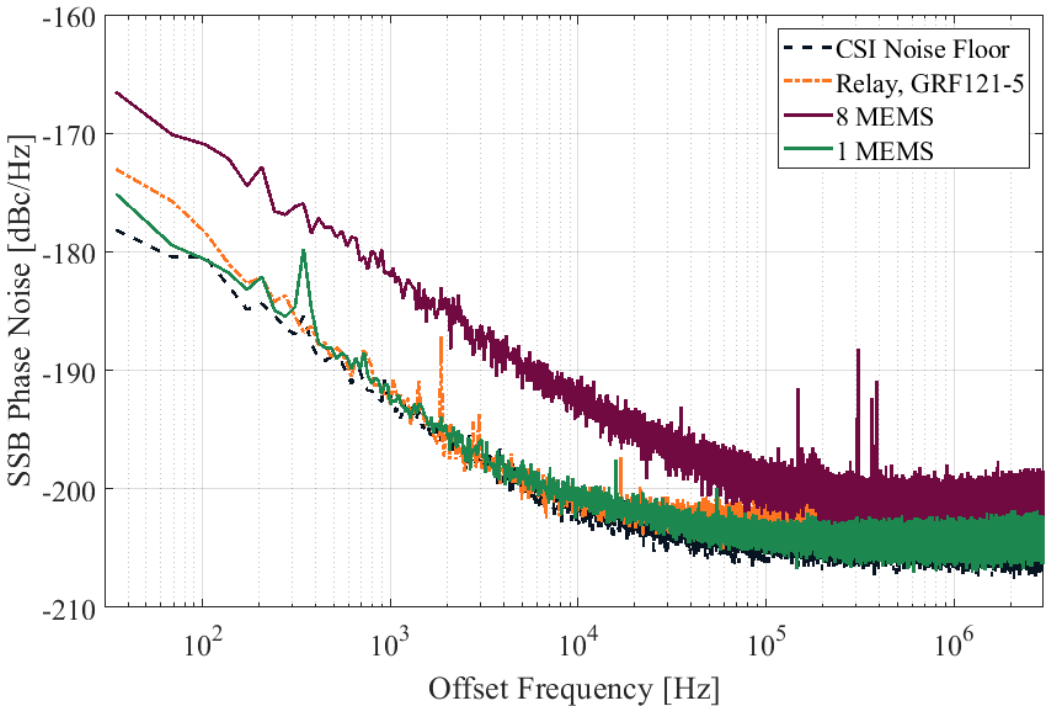

Figure 4.14: Phase noise measurements of the MEMS-based phase shifter with eight MEMS-chips in comparison to only one MEMS-chip (dashed). In addition, the measurement result of the miniature magnetic relay and the noise floor of the CSI are shown.

only section that might lead to the remaining noise deviation in Figure 4.12 is the contact area between the cantilever and the drain surface.

Figure 4.15(a) shows the cantilever ideally connecting source and drain via the applied gate voltage. Figure 4.15(b) shows a picture of the real cantilever area.

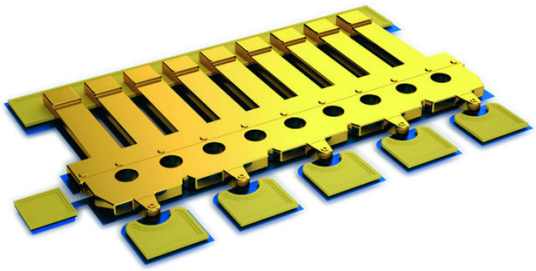

(a) Model of the MEMS cantilever (in courtesy of ©Analog Devices).

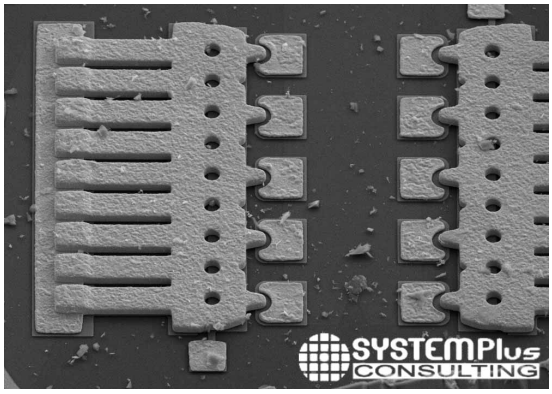

(b) Real photography of the MEMS cantilever (in courtesy of ©SystemPlus Consulting).

Figure 4.15: Visualization of the cantilever connecting source and drain contact.

The surface of the gold cantilever is not completely smooth. Additionally, a few grains around the critical drain area are visible as well. This is caused by two main reasons: The grain size for gold thin-films is limited to 25 μm to 50 μm, the roughness also plays a role [103]. Furthermore, the contact areas degrade for an increasing number of switching cycles [104]. The number of asperities on the contact surfaces increases with each cycle and causes contact noise. As mentioned before, contact noise appears wherever current density distributions are inhomogeneous, as is the case with inaccurate or changing contacts [29], [105], [106]. Considering the additional loose grains coming from the degradation or already from manufacturing processes, the likelihood of unplanned grain between the cantilever and the contact area increases. This combination of surface states and asperities is a possible explanation for the varying measurement results, even if at a very low level. On top of this, the spring force beneath the cantilever degrades with each switching cycle too, so that the end of the switch very likely is a steady contact.

The phase shifter with eight degrading switches in a row sums all these effects up. Additionally, if one switch has a defect from manufacturing, it is not easy to detect in series operation. Again, a preceding chip selection might by beneficial [65].

Compared to this MEMS switch investigation, the miniature magnetic latch showed no differing noise contribution in the measurements for both transmission ways at all. The measurement of this miniature RF switch GRF-151 [94] is shown in addition in Figure 4.14. Even a difference from the noise floor of the CSI could only barely be detected.

Commercial Phase Shifters

There is a variety of phase shifters commercially available for operation at L-band, most of them designed for a phase range of at least 180°. While the initial plan was to characterize off-the-shelf components to design low-noise actuators for the CSI, the investigations showed that they produce a variety of noise contributions, rendering them unsuitable in the scope of this work. Figure 4.16 shows measurement results for several commercial phase shifters biased to medium level operation. As the phase shifters are limited in signal input power large parts of the characteristic noise curves are hidden by the increased white noise level, caused by lowering the input power. An adjustment in power is chosen individually for each of the phase shifters.

Apart from the phase shifter type HMC936, the devices are biased with a battery module. For the HMC936 phase shifter a commercial low-noise power supply (Agilent E3620A) is used. Still, heavy disturbances are visible which could similarly be seen in other device measurements biased using the same power supply. Even if the single-sideband phase noise curves for the RVPT0302GBS and HMC936 are far away from optimal levels, the components are provisionally suitable for a conditioned CSI version to enhance the actual system performance of the LLRF-system. On the contrary, the noise from the phase shifter PA2141 is already detectable with the LLRF-system without improvements. Thereby this phase shifter is disadvantageous for the detector's further enhancement.

4.2.2 Mechanically-Controlled Devices

The main advantage of mechanically-controlled RF devices, e.g., trombone phase shifters, is that they do not require any bias voltage for operation, such that direct disturbances stemming from power supplies are barred from noise contribution. Nevertheless, the actuators have to be automatically adjusted in order to be suitable

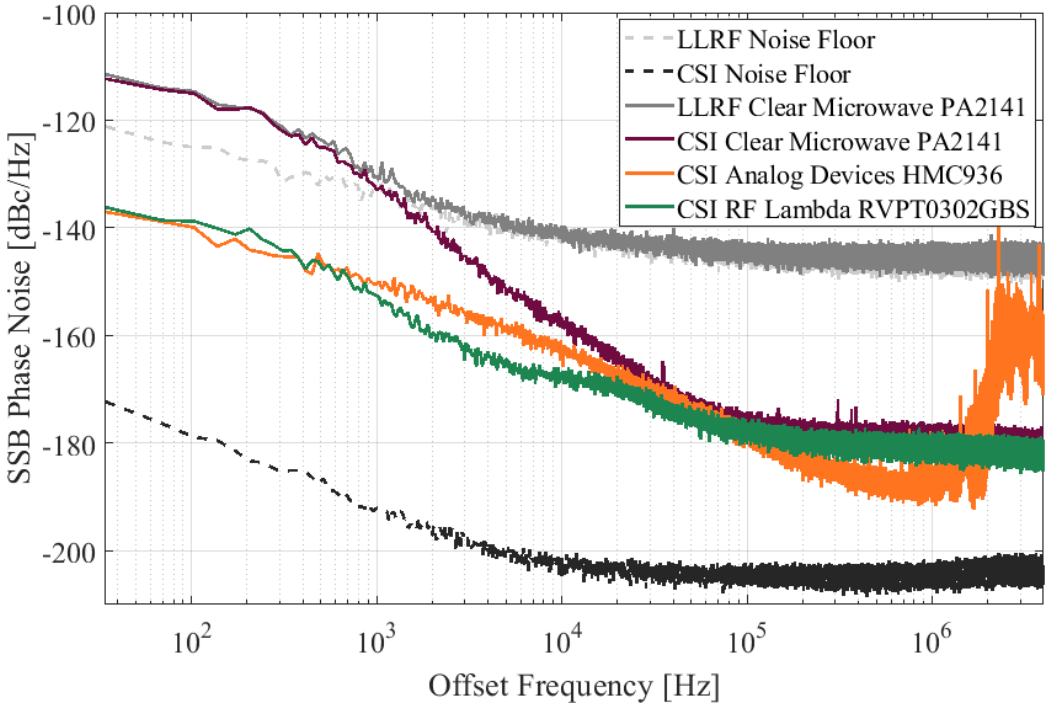

Figure 4.16: Phase Noise Measurement of different commercial phase shifters designed for operation at 1.3 GHz.

substitutions for the CSI's components. As one can only hardly steer every device manually inside a control loop, one needs to find an applicable control solution for phase or attenuation adjustment. Besides looking into the mechanical components in the CSI, this section considers different prototypes from research on assumed no-noise actuators. All of the presented devices require a sophisticated mechanical construction for their automated control, which in turn can lead to disturbances, for instance by vibrations or slippage of the servomotors. Again, one needs to make a trade-off between compact design and noise performance.

Mechanical Phase Shifters

A mechanical phase shifter is an RF device, which solely changes the signal phase by either manual length extension of the transmission line or distortion of the transmission itself. In this specific case, the length-extending so-called trombone phase shifter is in focus of the investigation.

Using only a plain cable instead of a real DUT the resulting noise spectra differ from measurement to measurement, when solely adjusting the carrier suppression

with the mechanical actuators. This, in connection with similar indications from literature [107], roused interest in the question, what exactly happens inside of these mechanical components leading to the slight variation in the measured noise spectra. It is observed that these components degrade significantly when used on a regular and intense basis as done in the CSI, and introduce increasing 1/f-noise while worn out.

Looking into the mechanical structure of such a phase shifter, one can see a bent tube sliding on a fixture, moved by an outer turning knob. The schematic of the phase shifter principle is shown in Figure 4.17. The sliding tube increases or decreases the length of the installed circular waveguide, accessible by RF connectors, and therefore changes the phase of the signal by adjusting the electrical length. While suppressing the carrier, one can knock, e.g., on the mechanical phase shifters

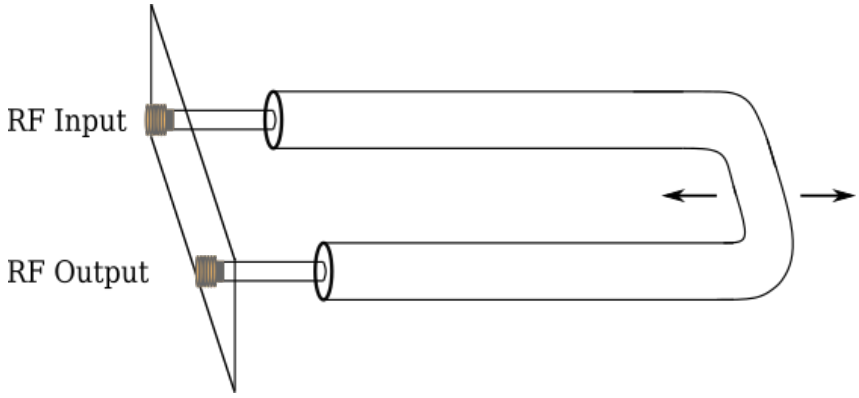

Figure 4.17: Sketch of the working principle of a typical trombone phase shifter.

and thereby change the internal phase, such that the suppression is clearly weaker or spoilt. An additionally observed effect is the decrease of 1/f-noise after knocking or slightly moving the adjustment knob on the phase shifter.

Based on these observations, one assumption regarding one possible origin of the contact noise contribution is that it emerges from inhomogeneous current flow and micro-tensions. The latter release when knocking on the component and establishes when using the device for carrier adjustment. This is well observable in the resulting time signal displayed on an oscilloscope, which jumps for each relaxation of a micro-tension and leads to voltage steps resulting in a new offset level, similar to the microphonic effects mentioned in Section 3.4. Here, the change in transmission path length when a mechanical micro-tension releases can handwavingly be expressed by

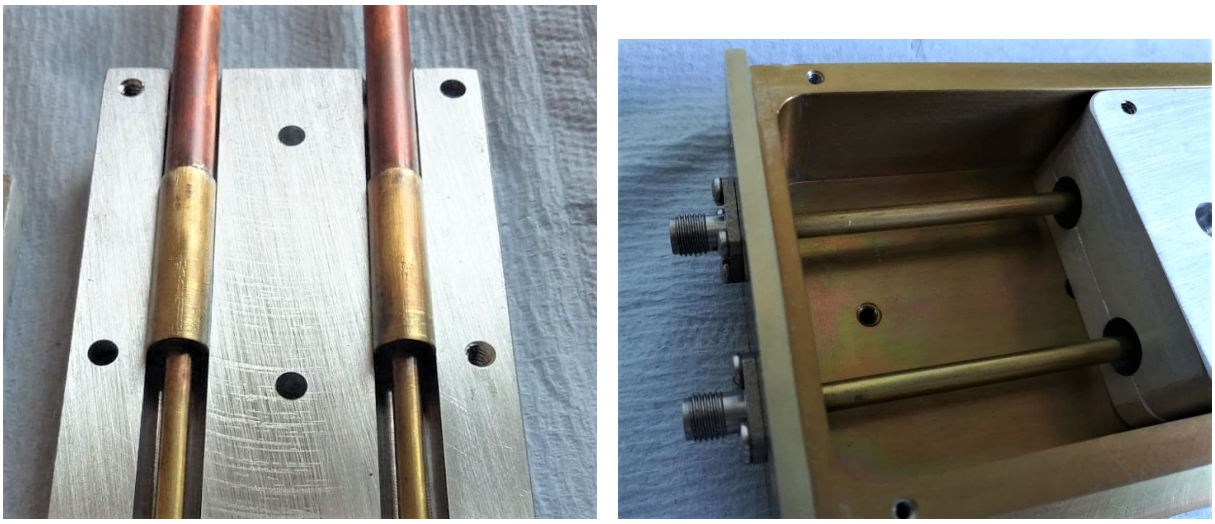

(a) Trombone section.

(b) Connection between waveguide and outer connectors.

Figure 4.18: Mechanical trombone phase shifter.

Young's modulus

$$E = \frac{\sigma}{\varepsilon} = \frac{F_m \cdot l_0}{\pi \cdot r^2 \cdot \Delta l}. \tag{4.6}$$

As shown in Equation 4.6, Young's modulus describes the relation of the tensile stress σ and the extensional strain ε [108]. Assuming a force of $F_m = 3\,\mathrm{N}$, a cross-section radius $r = 1.5\,\mathrm{mm}$, a Young modulus for brass (CuZn) of $E \approx 100\,\mathrm{GPa}$ and an original length of the rod of $l_0 = 20\,\mathrm{cm}$, the change in length is $\Delta l \approx 850\,\mathrm{nm}$, which is clearly detectable by the CSI .

The inhomogeneities in the contacts might for instance be introduced by surface imperfections. For moveable components within the attenuators or phase shifters these imperfections lead to abrasion and even more inhomogeneities and in consequence to higher contact noise [29].

Figure 4.18 shows the section in an exemplary mechanical phase shifter, where the adjustable bent tube enfolds the fixed circular waveguides. If the grease between the waveguides is deficient or due to other unwanted particles, abrasion between the pipes occurs. In this case, the surface roughens up more and more and the current distribution becomes inhomogeneous. Especially in a trombone phase shifter, the abrased particles lead to micro-tensions or retain the trombone, which was observed in measurements. Nevertheless, since the 1/f-noise is measured at high frequencies, additional nonlinearities must be present to modulate the contact noise from the baseband to the high-frequency band.

Mechanical Attenuator

Similarly to the mechanical trombone phase shifter, the functional principle of the mechanical step attenuator is of high interest. Figure 4.19(a) shows a picture of a

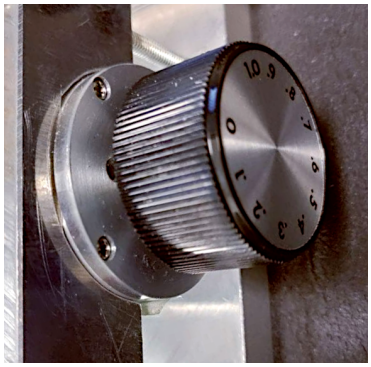

(a) Turning knob of a step attenuator with discrete steps from 0.1 dB to 1 dB.

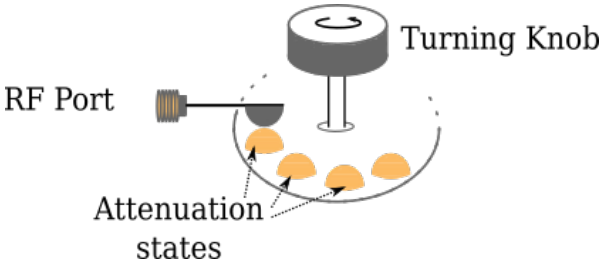

(b) Visualization of the inside of a step attenuator.

Figure 4.19: A step attenuator.

circular attenuator's discrete turning knob. Figure 4.19(b) shows the corresponding inside structure of the attenuator's discrete state selection mechanism schematically. One of the RF ports is visible on the left-hand side, the other RF port is not shown and is located below the switching mechanism. A metal "tongue" connects the inner conductor of the coaxial connector with a contact disc. The contacts on the disc are small metallic spheres and connected below to resistors, forming the specific signal attenuation. When rotating the disc by turning the adjustment knob, another resistive attenuation stage is selected.

With support from the DESY NanoLab and one of their scanning electron microscopes [109], Figure 4.20 presents the surface of one of the contact spheres with increasing magnification. Already on the lowest magnification stage dents, grooves, and polished areas are visible. For higher magnification it gets even worse as single chunks and layers are displayed. All these irregularities lead to instabilities in the current distribution and in consequence to increased contact noise. The question is not whether there is a contact between the surfaces, but rather how this contact is conditioned and how strongly the current flow is disturbed, as contact noise is a process at the atomic level [29], [110].

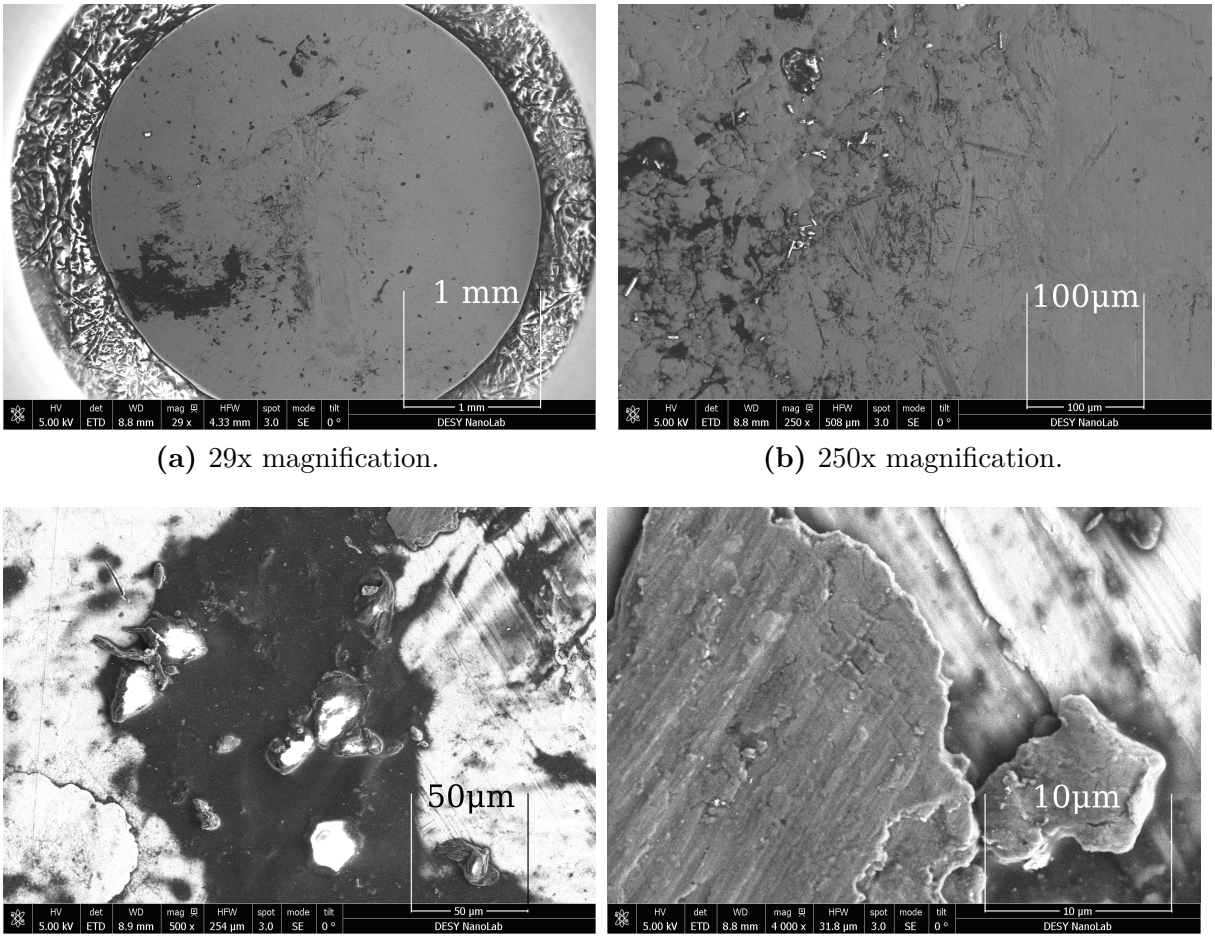

(a) 29x magnification. **(b)** 250x magnification.

(c) 500x magnification. **(d)** 4000x magnification.

Figure 4.20: Pictures of a step attenuator's contact sphere in different magnification stages.

Phase Shifter with Mechanically Variable Capacitors

To mitigate the aforementioned noise from varactor diodes, a reflective phase shifter assembled with four mechanically variable capacitors instead of semiconductor-based components is considered. A picture of the test board is shown in Figure 4.21(a). The housing of the commercial MiniCircuit SPHSA-152+ [111] was opened and the diodes on the PCB beneath substituted with tuning capacitors matching the required capacitances. In order to adjust the phase shift, one needs to adjust

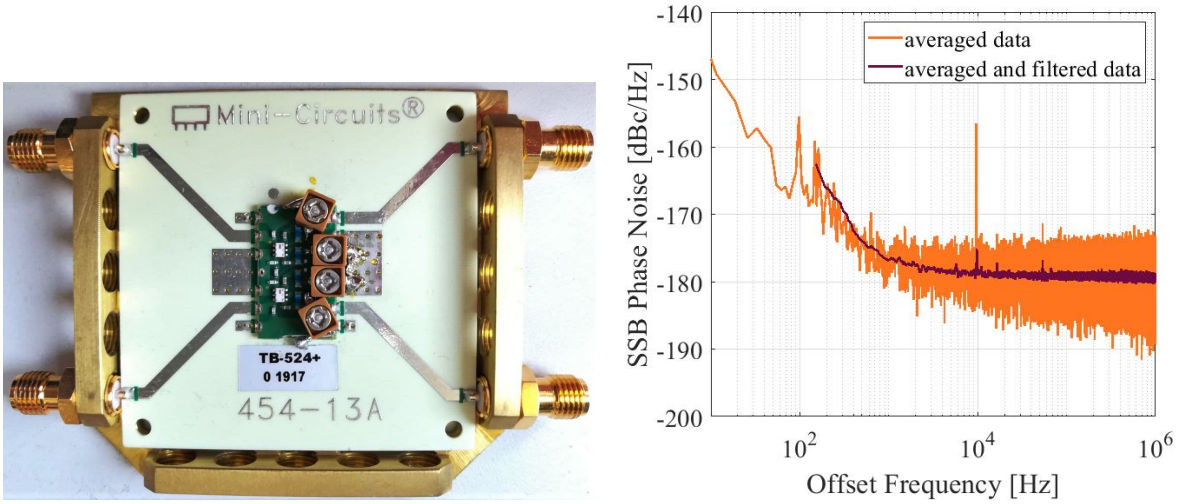

(a) Photograph. **(b)** Phase noise measurement.

Figure 4.21: A reflective phase shifter design with four variable capacitors.

the capacitive plates within each capacitor to meet the same capacitance value. For these measurements, the capacitors are adjusted in the most accurate way, manually, prior to assembly. For automatic and parallel phase adjustment, a small, sophisticated and very precise adjustment apparatus would be required, which is to be developed. The measurement results, as reported in Figure 4.21(b), show a few distortions in the lower 100 Hz range, which might be introduced by mechanical vibrations by imperfect fixing onto the optical ground plate of the CSI. The spur at 10 kHz offset frequency corresponds to the calibration modulation frequency and is a leakage from the connected frequency generator.

Meander Microstrip Phase Shifter

The next phase shifter is based on a simple microstrip transmission printed on a PCB, which is overlaid by an alumina plate at a distance of few millimeters to the line. The distance can be varied by a micrometer screw. Figures 4.22(a) and 4.22(b) show the meander microstrip transmission line without and with the lid. The idea is to either steer the phase shift by influencing it with the alumina surface of the lid or to use a thin ferrite sheet glued onto the bottom side to change the capacitive portion of the transmission line.

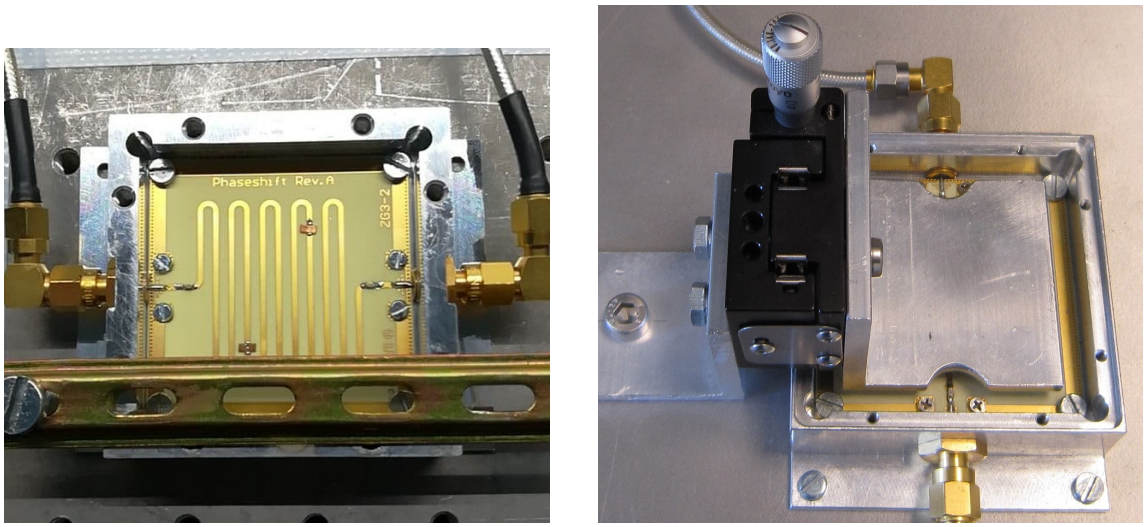

(a) Raw meander stripline with copper stubs for matching inside the CSI.

(b) Meander stripline covered by an alumina surface. The influence on the phase is adjusted via a micrometer screw on top.

Figure 4.22: Pictures of the meander stripline phase shifter.

The phase noise measurement of this aperture is shown in Figure 4.23. In terms of transmission and phase shift, the phase shifter works well, but as the alumina plane is only fixed in one direction it allows for physical oscillations. A strong disturbance in the noise spectrum below 200 Hz is visible, which most likely stems from the oscillating lid. For comparison, the phase noise measurements of the meander microstrip transmission line as shown in Figure 4.22(a) without any lid on top are presented in Figure 4.23 as well. The spectrum obtained for the pure transmission line matches the system's noise floor, which means that no noise

contribution is visible. Of course, without lid, the phase shifter is only a delay line

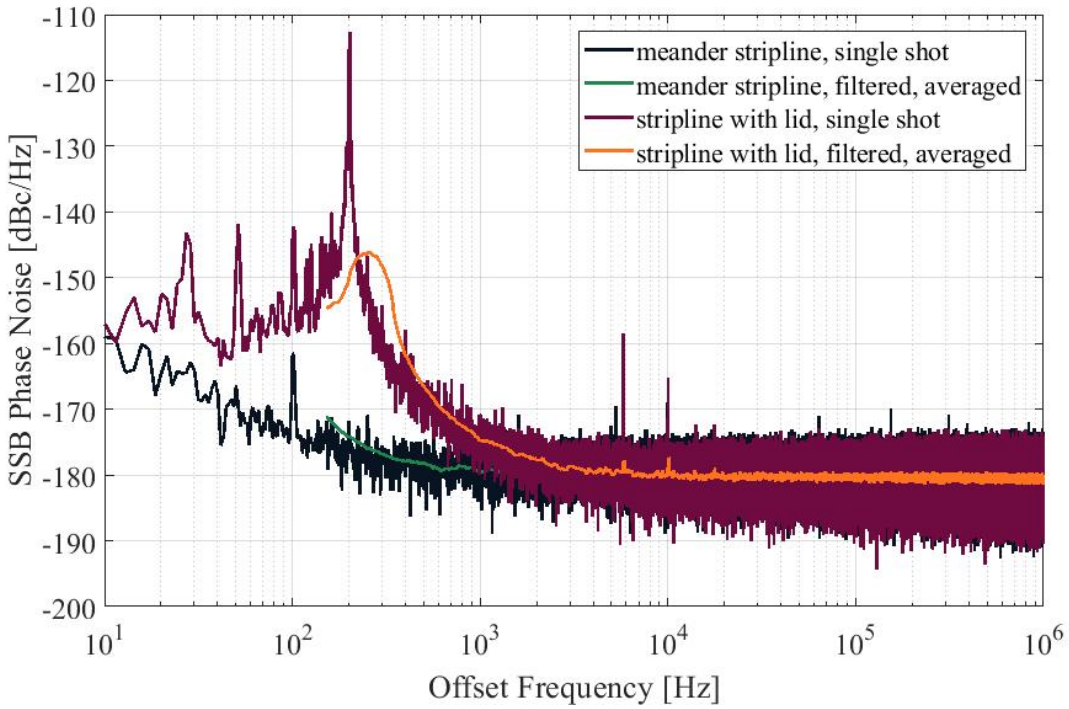

Figure 4.23: Phase noise measurement of the meander-stripline phase shifter with micrometer-aperture.

with a fixed delay and the measured curve follows the same behavior as the system noise with a difference of 1 dB introduced by insertion loss.

A second application of this meander stripline is in the investigation of the noise changes for the field interaction with ferrite sheets, as used in phase shifters, isolators, and other microwave components. This is important for future designs and component selection. For this experiment, solid copper lids were manufactured for varying distances between the elevated surface of the copper lid and the transmission line. A picture of one of the lids is shown in Figure 4.24. The elevated area is designed for full coverage of the meander stripline and fits the size of commercial ferrite sheets.

As this experiment targets only the noise behavior of a signal partially passing a ferrite material, there is no adjustment designed to change the phase shift. Eight

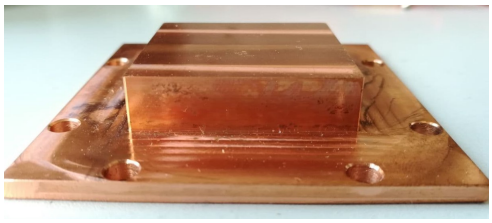

Figure 4.24: Copper lid for the meander transmission line.

appropriate screws fix the lid to the housing of the transmission line, so that no vibrations disturb the performance.

Magnetic Phase Shifter

As another option for low-noise phase shifters, the interest was to measure a magnetic phase shifter prototype design from an industrial partner [101]. A photograph of this phase shifter is shown in Figure 4.25(a). It is about 20 cm high and rather bulky in design. In the front, classical sub-miniature version A (SMA)-connectors are assembled. Inside of the iron housing, a commercial RF isolator is placed, connected by semi-rigid RF cables. On the tip of the adjustment screw a strong magnet is fixed. The magnet distorts the field on the inside of the isolator, such that a phase shift occurs. The maximum limit of adjustment is given by the nut. When changing the magnetic field, the transmission of the RF signal is affected by a movement in phase.

In the phase noise measurement spectrum shown in Figure 4.25(b) a plateau from the kHz-range to approximately 50 Hz can be observed. This might be introduced by the material of the isolator, which the signal passes. In the lower frequency range a few peaks are visible, which based on prior experience can again be explained by small vibrations and oscillations as well as by a neighboring noise source.

4.2.3 Outcome of the Investigation for Future CSI Components

A future CSI setup is ideally free from bulky, manually adjustable components, is able to automatically keep the carrier suppression at a sufficient high level, performs at a very low noise floor and high spectral purity, and is capable of high signal power levels. This investigation of components was initially planned to evaluate commercial devices and substitute them in the CSI with ease. The characterization of the commercial components very quickly showed that these are unsuitable if

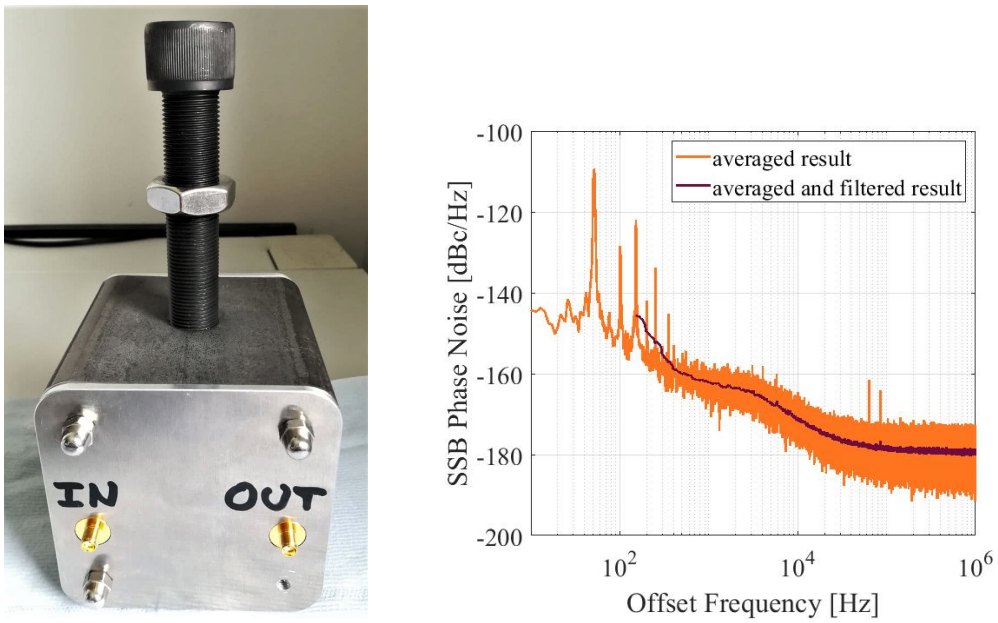

(a) Photograph. **(b)** Phase noise measurement.

Figure 4.25: A magnetic cavity phase-shifter.

the CSI is to continue to operate with as little noise as possible, and therefore very quickly aimed at investigating the largest noise sources in the individual components and developing new ones.

Starting with the active components, diodes still are the most promising candidates for uncomplicated and simple designs. A low-noise biasing structure of up to 20 V is in most of the cases enough. Nevertheless, the investigation shows that there is still no clear solution for the reliable prediction of phase noise in classical varactor diodes and the selection parameters are manifold, such that distinct phase noise measurements are necessary for every single diode.

Barium strontium titanate as another varactor type is very attractive for very compact designs due to the achievable packaging size. Two BST chips from the same company have been measured. Both show in the measured spectra a steep phase noise increase to the close-in frequencies with a tendency to lower noise for higher bias voltages. The maximum design voltage is 30 V, which becomes more challenging to provide in a very clean manner. For an active varactor, the measurement results are fair, but in combination with the drawback of the high bias voltage, the chips become unsuitable for CSI devices.

For discrete phase or attenuation steps, the switch types were evaluated. While the MEMS show some variation in noise at a very low level, the miniature magnetic latch seems more reliable in its performance. Of high interest is the capability of

high signal power levels as the step components are used in the CSI region, where the signals are still in full power. The magnetic latch exceeds the MEMS switch in the power handling, but is at the same time rather large in size compared to the MEMS.

The passive components are all together not electronically steerable without the design of a sophisticated controllable actuation. The noises stemming from the mechanical devices are not proven in detail, but there are reasonable assumptions and indications from the literature. This noise builds for now the close-in noise floor limit of the CSI. Increasing the system power would likely lead to a lower noise floor for offset frequencies above 20 kHz, but the characteristic for the lower offset frequencies will remain. Very careful selection and further development of the actuators is mandatory to be able to replace the mechanical components in a suitable manner. The lower the requirements for the desired system performance and signal power, the more choice of components there is.

4.3 Detector Front-End in Accelerators

As mentioned before, the intended overall aim of the presented setup for DESY is the improvement of the field detection system for the control system of the superconducting accelerator cavities. The detector front-end receives the output RF signal of the accelerator cavity. This signal is picked up by an antenna in the last cavity cell. At the time of this work, the detector front-end is limited to a white noise floor of $-146\,\mathrm{dBc/Hz}$, resulting in several femtoseconds of integrated timing jitter. The corresponding measured spectrum is shown in Figure 4.26 including the cumulative jitter. The most significant noise contribution originates in the

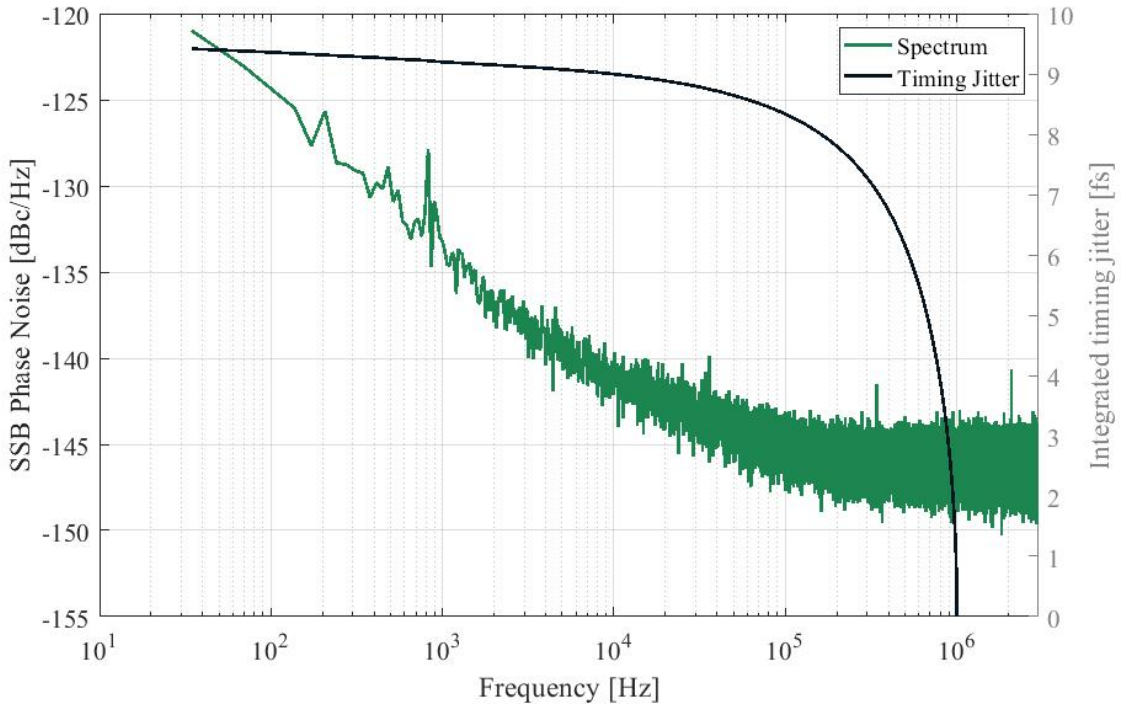

Figure 4.26: Standard single side-band phase noise performance of the current LLRF-systems detector typically used for linear accelerators at DESY.

downconverter and ADC section as discussed previously. This system component is not only a limiting factor for the close-to-the-carrier noise detection, but also for the allowed incident RF signal power at the input of the downconverter and thereby a limiter to the detectable white noise level. Similar LLRF-systems at

other accelerator research centers reach comparable results, although partially at differing conditions [112], [113]. The common alternative to downconversion and thus avoiding the mixer's noise is the direct sampling of the measurement signal. Here, the limiting factor for noise is the ADC.

The current dynamics of the CSI, i.e., measurement and processing time, more favorably support the application in continuous-wave (CW) machines, although large efforts are established to mitigate these time constraints.

Nevertheless, as the next generation of linear accelerators is in large parts centered on CW or long-pulse operation, the CSI's principles continue to be of high relevance. This is due to the fact that the constantly changing requirements for structural investigations performed with the resulting photon beams tend to move to longer photon bunch durations or continuous light sources [114].

4.3.1 Application of the CSI to RF Control Systems

When preparing the measurements with the CSI under real accelerator conditions, it is crucial to understand the difference compared to the existing LLRF-system used for EuXFEL and FLASH at DESY. To use the CSI as part of the LLRF control system, a few changes to the system and the measurement setup are required. Starting with the hardware of the overall setup, the CSI needs to be implemented within the control loop as shown in Figure 4.27 between the signal pick-up and the LLRF-system. Figure 4.27 presents the setup for the CSI as a receiver front-end to the common LLRF-system structure. This block diagram is a proposal for the future accelerator application of the CSI at the CW-test facility Cryo Module Test Bench (CMTB) at DESY and has not been proven in practice at the time of writing.

The proposed setup is designed such that it offers the possibility to make use of the CSI while the previous control structure remains almost unchanged. Referring to Figure 4.27, the signal coming from the cavity pick-up antenna is fed into the CSI instead of a DUT. A splitting section enables to either apply the carrier suppression or to rely on the well-established control system. Following both possible signal paths in Figure 4.27, the first stage after passing the CSI within the post-processing system is the downconverter module for down-mixing to an IF below 100 MHz. Afterwards the signals pass a software- and field programmable gate array (FPGA)-section, where the signals are demodulated to baseband I and Q, then rotated in phase and scaled in amplitude. The controller then adjusts the difference between the set point and the obtained signal to a minimum for each signal channel. Both resulting data sets are then finally adjusted in amplitude to

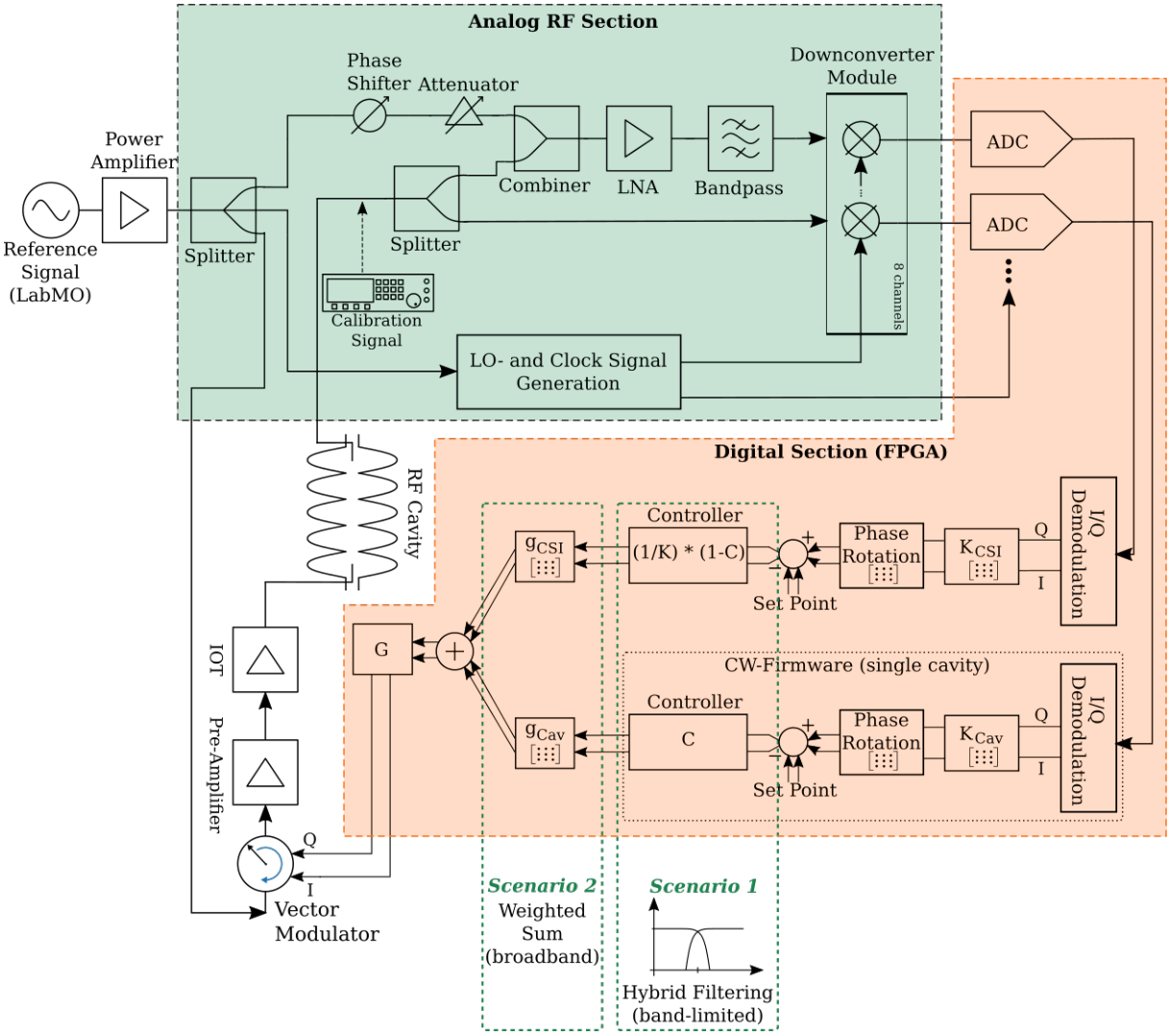

Figure 4.27: Schematic of the CMTB facility [115] including the CSI.

match and be combined before an overall gain adjustment follows. The ensuing I and Q data coming from the controller with gain (G) is then inserted into a vector modulator to adjust the signal according to the measured values. The resulting RF signal subsequently passes a high-power amplifier, before entering the inductive output tube (IOT) or more commonly a klystron. The modulated and amplified RF signal then excites the beam-accelerating field inside the accelerator cavity. The lower the noise contribution of the RF receiver itself is, the lower the deviation of the RF cavity field's phase from the RF reference signal [116].

There are two possible scenarios for the combination of the CSI data and the data of the standard LLRF signals. Since the CSI is at the moment only manually adjustable and primarily designed for phase noise characterization, it is not able

to cover the full field-control characteristics. In order to still have the full carrier information, one has to combine the standard LLRF-system for the close-to-the-carrier frequency section and the CSI for the higher offset frequencies, as it is roughly outlined in Figure 4.28 [8] and denoted as *Scenario 1* in Figure 4.27.

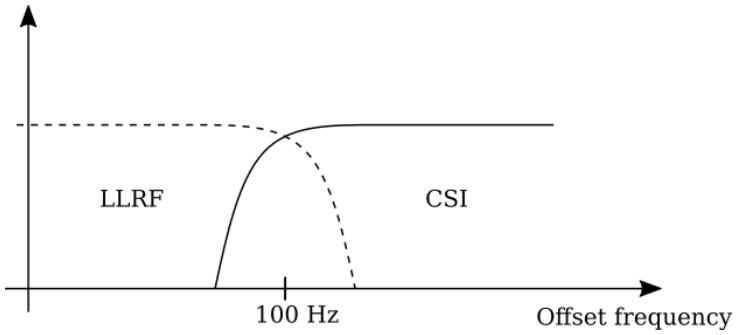

Figure 4.28: Sketch of the spectral coverage of a hybrid system approach connecting the noise spectra in both the LLRF-system and the CSI.

The combination would enable fast reactions for the most critical low-frequency phenomena and allows for a higher resolution at higher offset frequencies. A drawback would be the trade-off between high detection resolution for offset frequencies close to the carrier and the data-processing and control speed. Technically, such a combination can be implemented by signal low- and high-pass filtering with a cut-off frequency of, e.g., 100 Hz. When choosing *Scenario 1*, *Scenario 2* will be bypassed.

The second approach is the weighted combination of both signal channels, as depicted by *Scenario 2* in Figure 4.27. The translation of the well-known control signal to the CSI control signal can be performed in a defined manner and the possible change in the result can be monitored directly. The aim is to slowly increase the influence of the CSI data by adjusting g_{CSI} and g_{CAV}. In this case, the controller C will be bypassed and a feed-forward has to be introduced. In both approaches, an ideal controller would show no improvement in the error, as its only task would be to keep the error at a minimum.

For reliable measurement results, the CSI system calibration factor (K_{CSI}) must be determined regularly as explained in Section 3.3, whenever the actuators have been adjusted to follow the carrier suppression. Several monitoring systems help to ensure the correct functioning of the combined system. The calibration of the

presented hybrid LLRF-system could be done by first determining the calibration factors of the CSI, which are decisive for the fit of the measured noise power levels, and then tuning the phase of both systems with the help of a distinguishable single tone through the cavity. The calibration results would be applied in form of parameter sets, which are written into the FPGA registers.

4.3.2 The CSI for CMTB at DESY

A few CW research machines are spread around the globe and one of them is located in Hamburg: the so-called CMTB. This facility was originally designed to test the serviceability of single superconducting cavity modules before using them in the EuXFEL. Besides these functionality tests, the facility is used for research and development in linear CW acceleration [117] and it is depicted in Figure 4.29.

Figure 4.29: Top view of a cryo module under test at CMTB.

To give an overview about the systematic structure, Figure 4.30 shows the block diagram for the proposed LLRF-crate combined with the CSI for the CMTB application. The crate consists of several sub-systems (e.g., signal generation).

The central component is the MicroTCA.4 system [118], which combines for this application the RF receiver with the downconverter section and IQ-modulation (DWC8VM1), the clock signal generation and timing section (μLOG), the signal post-processing, and the controller [119]. The CSI will have direct interfaces with the μLOG and the DWC8VM1 to which it delivers two signal channels (CSI and REF). In addition to the previous standard crate configuration, space for further high-power amplifiers, the calibration signal generation and optional control voltages for actuators in the CSI must be considered.

As shown in Figure 4.27 in detail, the incoming cavity signal is split into two paths inside of the CSI. One passes the CSI without any changes, the other one passes the carrier suppression. The cavity pick-up signal is in this scenario the DUT output.

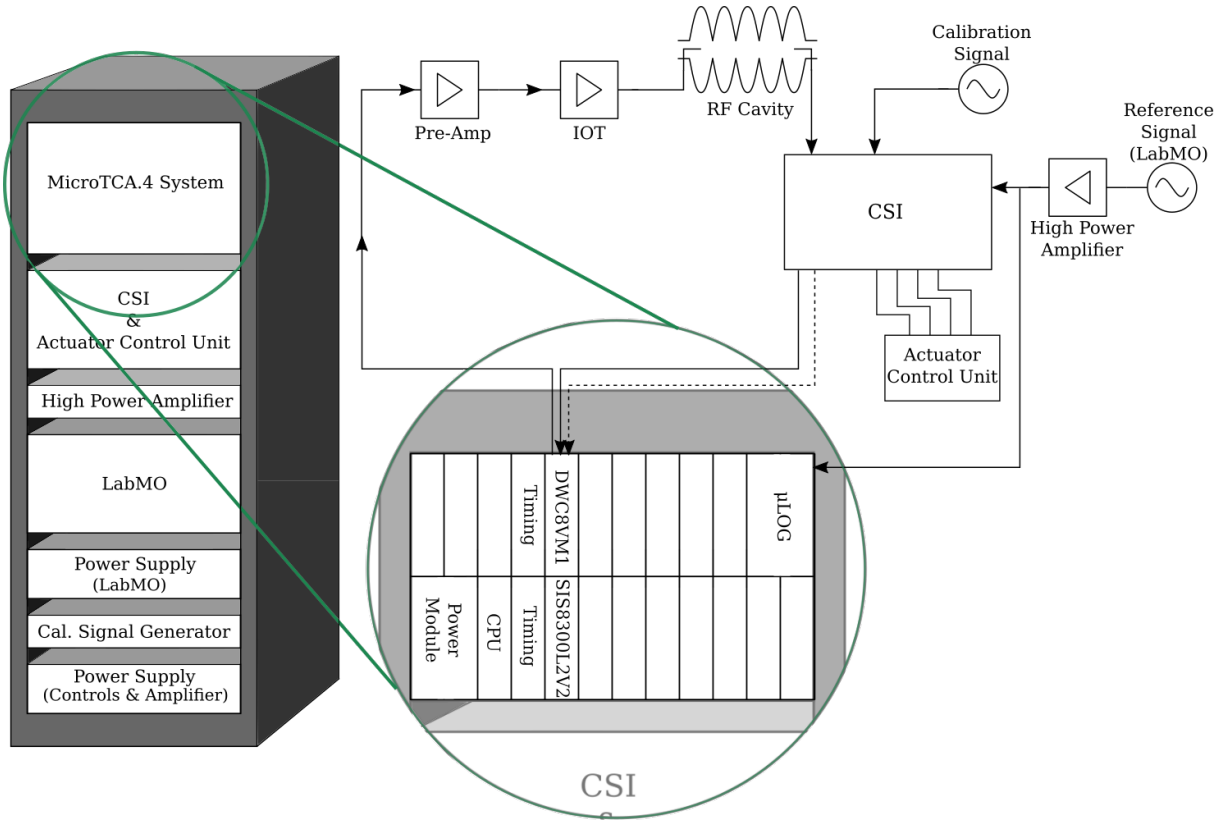

Figure 4.30: The CSI setup in accelerator configuration.

The heaviest requirement for the CSI to operate in a control loop is the automated carrier suppression. Approaches have been demonstrated in earlier literature [120].

At the moment of writing there is no automated carrier suppression in use. An automated carrier suppression requires highly sensitive, electronically steerable phase shifters and attenuators. One focus within this work is the investigation of different types of phase shifters that would be suitable for this challenge, as discussed in Section 4.1.

Specific investigations of phase noise components in a closed-loop scenario have been shown in literature [7], [8], [50]. It has been demonstrated, that in feedback configuration mainly the receiver noise sources and the signal source noise contribute to the cavity's output signal, whereas other noise sources are strongly reduced. There are different types of measurements to be carried out in order to establish the performance of the control loop and its components. First of all, one can distinguish between open- and closed-loop measurements, which refer to the control-loop quality, and between in-loop and out-of-loop measurements, which represent the performance of single components within the control chain. As the interest is in the performance of the receiver front-end, open- and closed-loop measurements of the full system are not helpful, as they always include the noise from the downconverter section next to all other noise sources from the high-power components, e.g., the power amplifier and the IOT.

Closed-loop measurements correspond to in-loop measurements on the component side, including all actuators. An out-of-loop measurement is necessary to be able to characterize single components within the control chain [7], [121]. For this type of measurement, a parallel watch-dog receiver front-end is required. Assuming both receiver front-ends contribute with the same noise, one can evaluate the field quality by means of correlating the measured signals. As the CSI setup is planned to be a front-end to the downconverter section and is thereby a new component of the field receiver, two CSI setups are required for characterizing the field receiver during operation in the accelerator control loop. Without automation of the setup this measurement is not possible and thus still requires significant future work. At the Elektronen Linearbeschleuniger für Strahlen hoher Brillanz und niedriger Emittanz (ELBE), a similar configuration of a CW research facility is located, called Tera-Hertz at ELBE (TELBE). It is part of the Helmholtz-Zentrum Dresden-Rossendorf (HZDR). There, to characterize the cavity field without the contribution of the field receiver, a commercial phase noise analyzer was used as a parallel watch-dog detector [8]. The correlated measurements clearly show the cavity filter function and strong noise ripples coming from the high-power components.

For the CMTB in Hamburg, Figure 4.31 shows an open-loop measurement including the pre-amplifier, the IOT, the cavity and the receiver noise. The recorded signal

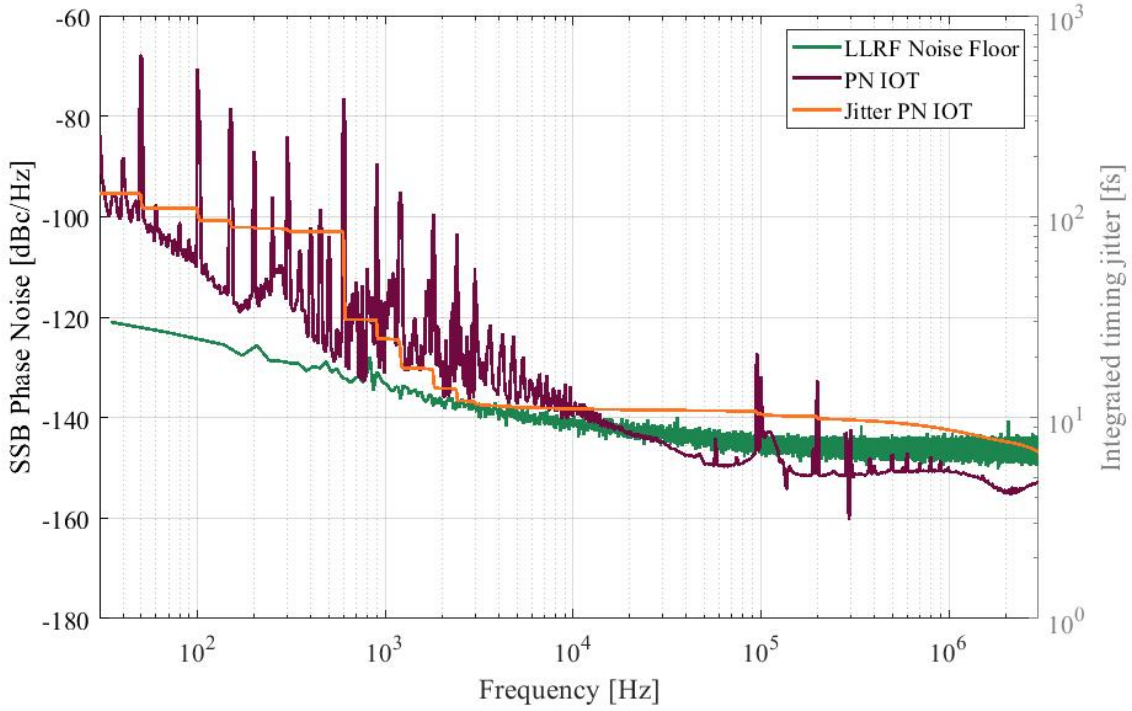

Figure 4.31: Open-loop measurement of the incoming signal to the LLRF-crate at CMTB.

is comparable to the incident signal of the receiver front-end and the subsequent control system under typical operating conditions. Thorough investigations at FLASH have shown that the RF receiver is the noise-dominating part in the control loop, when the control chain is closed [121].

Reducing the influence of the downconverter with the CSI as a receiver front-end leads consequently to a lower noise floor of the LLRF-system and therefore to a higher detection resolution, depending on the possible control loop gain [8]. For the control loop itself, a higher detection sensitivity does not necessarily lead to a smaller error as the computing structure might be limited in bit-resolution. Referring to the out-of-loop measurements at TELBE, the noise from the high-power actuators is strong, such that an even more sensitive LLRF-receiver would not necessarily be more profitable.

At the time of writing the CSI is capable of residual phase and amplitude noise measurements. For the accelerator application it is furthermore necessary to identify absolute amplitude noise sources, which have to be investigated further with the CSI. Current efforts regarding the application of the CSI to the control system include soft- and firmware preparations for the LLRF-crate in the laboratory environment

that can in a later step be transferred to the crate at the CMTB at DESY, as the hardware is identical, to enable investigating the proposed hybrid approach.

5 Conclusions and Future Work

This thesis investigates the development and application of an amplitude and phase noise detection and measurement setup based on the suppression of the carrier frequency. On the one hand, this setup enables the characterization of RF components with highest resolution, on the other hand, the setup is a future enhancement of the detector's receiver front-end for field control in CW accelerator facilities. The strong interest in understanding the origin of the noise contributions from various RF components and technologies forms, together with the measurement setup, the heart of this work, with the overall goal to improve the RF field's detection resolution in the context of accelerator control.

5.1 Conclusions

After a brief introduction to the scope and motivation of this thesis, Chapter 2 covers the fundamental physical relations and quantities related to the topic of noise measurements and is substantial for the further field detector development. Noise measurement methods are compared and the carrier-less noise measurement is introduced. Afterwards, Chapter 3 describes the carrier-less measurement setup, the CSI, in the laboratory. The development process of the setup is shown and challenges during the setup's advancement, such as the sensitivity against changes in the environmental conditions and vibrations, are discussed. The major factors are identified and reduced, e.g., by damping the setup's ground plate, component fastening and packaging and keeping the air conditions stable. These enhancements in stability, reliability and functionality enable achieving near-undisturbed measurements and spur-less results of highest accuracy with the single-channel CSI. The measurement setup and its evolution are outlined and followed by the presentation of the latest noise performance measurements of the setup itself. The steady optimization of the CSI setup yielded a white phase noise floor of $-205\,\mathrm{dBc/Hz}$ for the CSI system at an operation frequency of $1.3\,\mathrm{GHz}$ without the usage of correlation techniques. The corresponding integrated timing jitter of $10.76\,\mathrm{as}$ was measured for the bandwidth of interest in the accelerator environment, in the band from

40 Hz to 1 MHz from the carrier. Amplitude noise measurements with the CSI were investigated, resulting in similar spectral purity and noise floor levels as for phase noise measurements.

The CSI setup combines the common heterodyne receivers with carrier suppression and builds thereby a front-end to existing RF noise receivers. To achieve a more compact and automated design, as is required for productive operation in an accelerator facility, several phase shifter and attenuator types and designs in different technologies have been investigated in terms of their noise contributions and their possible influence on the total system performance. Therefore, Chapter 4 discusses the application of the CSI in two fields: First, the CSI is applied and presented as a noise analyzer for lowest noise powers and suitable to identify actuators for the future automated CSI setup. Second, the application in the accelerator environment is discussed.

As a noise analyzer, the main focus was on the selection of suitable phase shifters and attenuators for the setup's further improvement. In comparison to commercial phase noise measurement devices, the CSI provides an outstanding near-carrier noise performance, which enables close-to-the-carrier noise evaluations of DUTs. Several off-the-shelf products were characterized with the CSI and identified as not suitable, such that the design of custom-made actuators is prioritized. Next to modern materials like BST, mainly classical varactor diodes were in the focus of the presented evaluation. As a valuable alternative to varactor components, RF switching devices like, e.g., MEMS or relays, are discussed. All presented technologies and topologies are investigated in terms of possible noise sources inside their respective structures. For varactor diodes, the most concerning effect is the noise increase with increasing bias voltage. The bias voltage is unavoidable for modifying the junction capacitance and thus required for the functionality of the phase shifter or attenuator. Even with cleanest voltages from batteries, this noise increase is crucial. RF switches and passive mechanical devices have shown to suffer from increasing contact noise, as measurements indicate. Concatenating switching components on a PCB to adjust for phase or attenuation ranges have shown to even increase the observable noise contributions. In addition, passive phase shifters and attenuators suffer from several mechanical issues, such as oscillations and abrasion.

Following these investigations on devices for increasing the maturity of the concept, further considerations on the application of the CSI as a module in the accelerator control cover the actual detector performance and outline the required tests. As the manual suppression routine and the processing of the measurement require some time, the first approach to accelerator conditions is the application of

the CSI to the CW accelerator research facility CMTB. At the end, the challenges and necessary modifications of the CSI are briefly presented.

5.2 Future Work

The presented measurements and results open the way to several potential follow-up projects. One of the next steps for the CSI is to prove its ability to operate reliably at the accelerator test facility CMTB, which requires thorough preparation and further design decisions. In addition to this, there are many topics left to be investigated in future work: In order to make the device characterization more efficient for the user, the post-processing time needs to be reduced significantly. This will enable to track even the smallest changes on-line, like it is supported by common commercial phase noise analyzers, and simultaneously limit the influence of drift effects. Additionally, when thinking about the application of the CSI in accelerator control loops, the system has to be controllable remotely and biased with extremely clean control voltages. The development of such a low-noise voltage distribution requires further efforts. A benefit and complement would be the ability of switching between phase and amplitude noise measurements without the re-configuration of the setup, or ideally even of doing simultaneous measurements. While amplitude noise measurements have been carried out and validated against commercial analyzers, especially in the extremely low noise floor levels, open questions remain.

As the CSI right now is a single-channel setup, one cannot take advantage of cross-correlation calculations. Using cross-correlation techniques would reduce the uncorrelated noise sources in the CSI. Depending on the number of taken correlations, the noise floor of the CSI might be reduced by up to 20 dB in exchange for processing time. For operation in the accelerator this development would be of limited benefit, due to the increase in processing time and control complexity. Nevertheless, especially for materials characterization purposes and the development of RF devices matching the accelerator requirements, such an extension would be crucial, as it would allow to increase the detection resolution even further and thereby open the way to the investigation of the smallest electrical processes within devices and materials.

Within the scope of developing new field detection receivers with increased resolution, there are several possibilities next to the enhancement of the CSI itself: As a limiting factor of the current LLRF-system for EuXFEL at the moment is the RF mixer in the field detector, an updated version of a high-level mixer topology with a CSI-based pre-selection of low-noise diodes could potentially offer relevant gains.

Currently, the second largest noise limiting factor is the noise of the processing ADCs. This requires the precise characterization of state-of-the-art ADCs. Another possible task is to parallelize the ADC either on PCB or, even more sophisticatedly, at the chip level. Also a parallelization within the diode-based phase shifter and attenuators structures might introduce signal power distributions, which are easier to handle.

Especially for linear particle accelerators an additional field of research is to increase the quality factor of the accelerating cavities, such that the bandwidth of interest and, in consequence, the control bandwidth are reduced and the spectral requirements are limited.

Overall, one can summarize that the research of highly sensitive detection of phase and amplitude noise offers a lot of potential for the improvement of RF field controls for CW accelerator facilities and new approaches for RF material and device characterization. This is highly relevant in order to address the ever rising demands from the accelerator research and development community, enabling highly sophisticated experiments addressing the grand challenges of science and the society.

A Supplementary Information on Amplitude- and Phase Noise

A.1 Historic Definition

Phase noise was traditionally defined as the relation between the noise over a 1 Hz bandwidth at a certain defined frequency offset and the amplitude of the carrier signal at the fundamental frequency f_0, as depicted in Figure A.1. This historic definition nowadays is obsolete as it does not define, whether the noise is an amplitude or phase noise, whether it represents only one or two sidebands and if it still is valid for very high noise levels [27], [122].

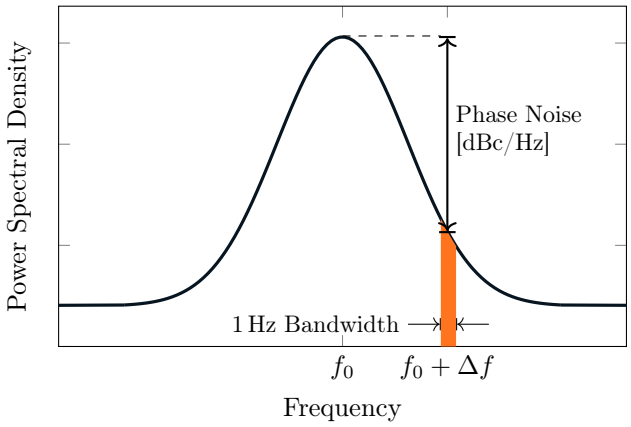

Figure A.1: Illustration of the nowadays obsolete definition of phase noise in dependence of the carrier signal power at f_0.

A.2 Time Domain Derivative of Frequency and Phase Noise

In addition to equation (2.13), the power spectral density can also be determined for the spectrum with the phase fluctuations with respect to time expressed via

$$S_x(f) = \frac{1}{\omega_0^2} S_\varphi(f), \tag{A.1}$$

given in s^2/Hz [27].

Analogously to the earlier defined phase noise and considering Equation (2.14), frequency noise is defined with

$$S_y(f) = \frac{f^2}{f_0^2} S_\varphi(f) \left[\frac{1}{\text{Hz}}\right]. \tag{A.2}$$

The relationship between the spectral quantities $S_\varphi(f)$ and $S_y(f)$ is complementarily displayed in Figures A.2(a) and A.2(b).

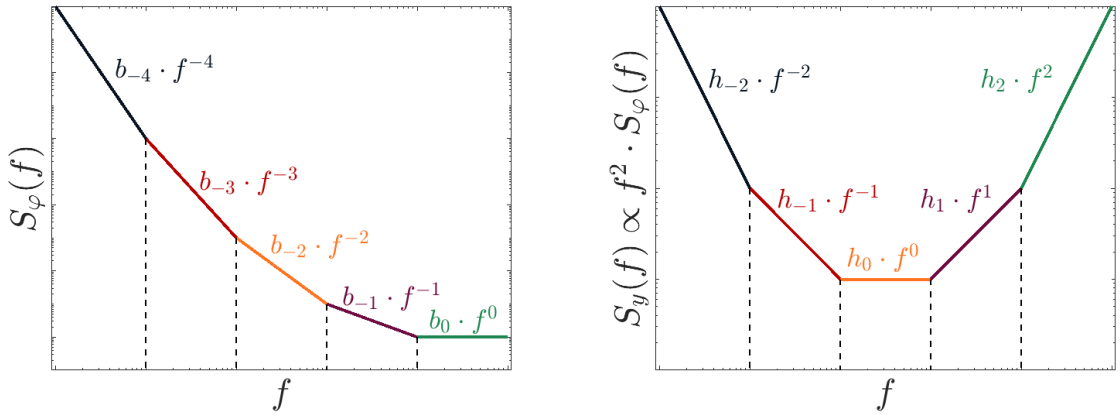

(a) Phase noise. **(b)** Frequency noise.

Figure A.2: Illustration of the power laws of phase and frequency noise over frequency.

A.3 Allan Variance

The Allan variance describes the noise analysis of the measured time signal. The focus here is on the evaluation of the variance of the measured signal for N samples. The detected signal, representing a time average of $f(t)$, is

$$\overline{f}_k(\tau) = \frac{1}{\tau} \int_{k\tau}^{(k+1)\tau} f(t)\,\mathrm{d}t \tag{A.3}$$

with a time interval τ starting at $k\tau$. With the normalization

$$\overline{y}_k(t) = \frac{\left(\overline{f}_k - f_0\right)}{f_0}, \tag{A.4}$$

where f_0 is the fundamental frequency, the measured signal follows as

$$\overline{y}_k(\tau) = \frac{1}{\tau} \int_{k\tau}^{(k+1)\tau} y(t)\,\mathrm{d}t. \tag{A.5}$$

The variance of $\overline{y}_k(\tau)$ for N samples is defined as

$$\sigma_y^2 = \frac{1}{N-1} \sum_{k=1}^{N} \left[\overline{y}_k - \langle \overline{y} \rangle_N\right]^2, \tag{A.6}$$

where $\langle \overline{y} \rangle_N$ is the average of $\overline{y}$ over N samples. As the classical variance degrades for long measurement durations, the so-called Allan variance was introduced for noise measurements [42], [123], [124]. The Allan variance, named after David W. Allan, is the expected value of the classical variance reduced to two samples under the condition that the samples are consecutive. It follows as

$$\sigma_y^2(\tau) = \mathbb{E}\left\{\frac{1}{2}\left[\overline{y}_{k+1} - \overline{y}_k\right]^2\right\}, \tag{A.7}$$

with the Allan deviation

$$\sigma_y(\tau) = \sqrt{\sigma_y^2(\tau)}. \tag{A.8}$$

The Allan variance is tightly interwoven with the power spectrum density in frequency domain, as illustrated in Figure A.3.

For time domain measurements the Allan variance enables the easy differentiation between the noise types. Modern noise measurement systems already have the option to show the Allan variance of a measurement signal. A conversion from the frequency spectrum to the Allan variance can be derived easily, but as the Allan variance is only the mathematical expectation - and therefore an approximation - a

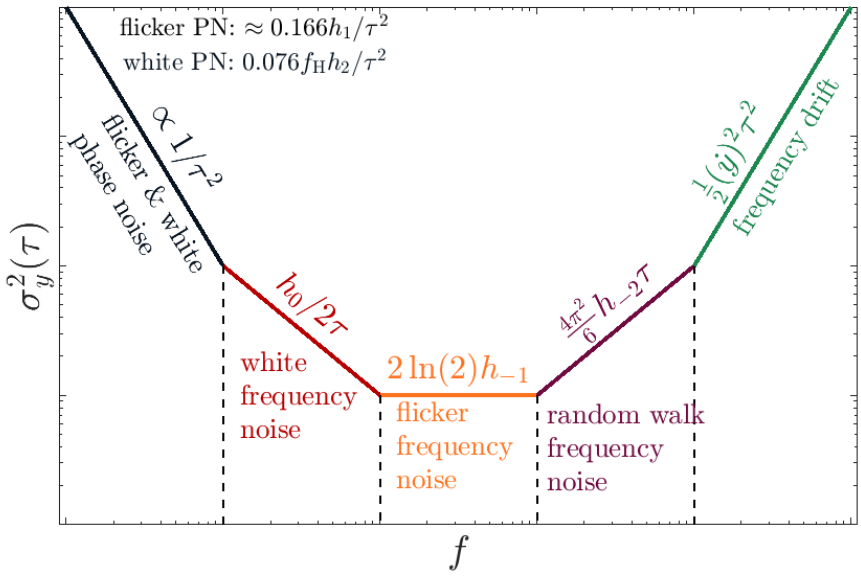

Figure A.3: Relation between the power spectrum density and the Allan variance in accordance to Table A.1.

backwards derivation is not possible without errors. The factors to be applied for conversion are listed in Table A.1 with cut-off frequency f_H.

In literature one can find modified versions of the Allan variance definition to accommodate for specific noise processes and discriminate between white and flicker noise [27].

Noise Type	$S_\varphi(f)$	$S_y(f)$	Allan Variance $\sigma_y^2(\tau)$
White phase noise	b_0	$h_2 f^2$	$\frac{3 f_\mathrm{H} h_2}{4\pi^2\tau^2}$
Flicker phase noise	$b_{-1} f^{-1}$	$h_1 f$	$\frac{3\gamma - \ln(2) + 3\ln(2\pi f_c \tau) h_1}{4\pi^2\tau^2}$
White frequency noise	$b_{-2} f^{-2}$	h_0	$\frac{h_0}{2\tau}$
Flicker frequency noise	$b_{-3} f^{-3}$	$h_{-1} f^{-1}$	$2\ln(2) h_{-1}$
Random walk of frequency	$b_{-4} f^{-4}$	$h_{-2} f^{-2}$	$\frac{2\pi^2 h_{-2}\tau}{3}$

Table A.1: Conversion factors for the translation of frequency spectra to time domain processes using the Allan variance.

Acronyms

ADC analog-to-digital converter . . . 3
AN amplitude noise . . . 15
BST barium strontium titanate . . . 73
CMTB Cryo Module Test Bench . . . 93
CSI Carrier Suppression Interferometer . . . 24
CW continuous-wave . . . 93
DC direct current . . . 16
DESY Deutsches Elektronen-Synchrotron . . . 1
DUT device under test . . . 15
ELBE Elektronen Linearbeschleuniger für Strahlen hoher Brillanz und niedriger Emittanz . . . 98
EuXFEL European X-Ray Free-Electron Laser . . . 1
FFT Fast Fourier Transform . . . 21
FLASH Free-Electron Laser Hamburg . . . 1
FPGA field programmable gate array . . . 93
HZDR Helmholtz-Zentrum Dresden-Rossendorf . . . 98
I in-phase . . . 17
IF intermediate frequency . . . 3
IOT inductive output tube . . . 94
IQ in-phase/quadrature . . . 17
LINAC linear accelerator . . . 1
LLRF Low-Level RF . . . 2
LNA low noise amplifier . . . 16
LO local oscillator . . . 15
MEMS Micro-Electro-Mechanical System . . . 76
PCB printed circuit board . . . 47
PETRA III Positron-Elektron-Tandem-Ring-Anlage, engl. positron-electron tandem-ring facility, currently PETRA III
PN phase noise . . . 15
PLL phase-locked loop . . . 17

Q quadrature . . . 17
REF reference . . . 25
RF radio-frequency . . . 3
RMS root mean square . . . 13
SMA sub-miniature version A . . . 89
SNR signal-to-noise ratio . . . 5
SSA signal source analyzer . . . 39
SSB single sideband . . . 35
TELBE Tera-Hertz at ELBE . . . 98
VCO voltage-controlled oscillator . . . 74
VM vector modulator . . . 39

Definitions

A, A_0	amplitudes of signals
$\alpha\,(t)$	time varying amplitude component
$\alpha_{\mathrm{src}}(t), \alpha_{\mathrm{src2}(t)}$	source signal's amplitude noises
b_i	weighting coefficient
B	bandwidth
$B_{3\,\mathrm{dB}}$	3 dB-bandwidth
C	carrier vector
C_0	fundamental capacitance
C_{j}	junction capacitance
C_{CSI}	spectral density of the CSI
C_{max}	maximum capacitance
C_{min}	minimum capacitance
C_{REF}	spectral density of the REF
$\delta(f_m)$	Dirac pulse at frequency f_m
e	Euler's number
E	Young's modulus
$\mathbb{E}\{\cdot\}$	expected value, expectation
ε	extensional strain
f	frequency
$f(t)$	measured time signal
f_0	fundamental frequency
f^i	frequency characteristic
f_{c}	carrier frequency
f_{H}	cut-off frequency

f_{IF}	intermediate frequency
f_{LO}	local oscillator frequency
f_m	main frequency, similar to f_0
f_{mod}	modulation frequency
f_{RF}	radio frequency
f_{sampling}	sampling frequency
F	noise figure
F_m	force
F_{FD}	calibration factor in frequency domain
F_k	noise factor
F_{TD}	calibration factor in time domain
$\mathcal{F}\{v(t)\}$	Fourier transform of $v(t)$
$g_{\mathrm{CAV}}, g_{\mathrm{CSI}}$	gain matrices
g_{LNA}	gain of a low-noise amplifier
γ	indicator for doping profile
G	dynamic conductance
G_k	power gain
h	Planck's constant
h_i	weighting coefficient
$i_{\mathrm{mix,\ out}}(t)$	mixer current
j	imaginary unit
k_B	Boltzmann's constant
k_α	conversion factor for amplitude noise
k_φ	conversion factor for phase noise
l, l_0	lengths
l_{M}	losses in a frequency mixer
l_{s}	systematic losses
$\mathcal{L}(f)$	power density spectrum
λ	wavelength

$n(t)$	noisy time signal
$n_\alpha(t), n_\varphi(t)$	substituted noise components
N	number of samples
$N_\alpha(f), N_\varphi(f)$	spectral densities of $n_\alpha(t), n_\varphi(t)$
N_e	equivalent noise spectrum
N_T	noise spectral density in black-body radiation
O^n	complexity factor, Landau notation
p, q	suppression factors
P_loss	power loss
P_tot	total system power
φ	phase term
φ_0	arbitrary phase value
φ_e	angle of phase error
$\varphi\,(t)$	time varying phase component
$\varphi_\mathrm{src}(t), \varphi_{\mathrm{src1}(t)}, \varphi_{\mathrm{src2}(t)}$	signal source's phase noise terms
ϕ_REF	phase angle
Q	quality factor
Q_max	maximum quality factor
Q_min	minimum quality factor
Q_varactor	varactor's quality factor
r	radius
r_CSI	CSI calibration radius
r_REF	reference calibration radius
R_0	termination resistance
R_b	bulk resistance
R_s	series resistance
$S_\alpha(f)$	amplitude noise spectrum
$S^\alpha_\mathrm{out}(f)$	output amplitude noise spectrum
$S_{\mathrm{out,\ P}}(f)$	output power spectrum

$S^{\varphi}_{\text{out}}(f)$	output phase noise spectrum
$S_{\text{out, V}}(f)$	output voltage spectrum
$S_{\varphi}(f)$	phase noise spectrum
$S_{\text{sup}}(f)$	spectral density of $v_{\text{sup}}(t)$
$S_v(f)$	spectral density of $v(t)$
$S_V(f)$	voltage noise spectrum
$S_x(f)$	spectral density of $x(t)$
$S_y(f)$	frequency noise spectrum
S_{zz}	autocorrelation function of z(t)
σ	tensile stress
$\sigma_y(\tau)$	Allan deviation
$\sigma_y^2(\tau)$	Allan variance
t	time
t_{RMS}	RMS time jitter
T	period
T, T_0	temperature, noise temperature
τ	time interval
τ_d	time delay
$v(t)$	voltage signal
$v_{\text{DUT}}(t)$	output voltage signal of the DUT
$v_{\text{LO},90^\circ}$	conditioned voltage signal
$v_{\text{out}}(t)$	final output signal
$v_{\text{out},q}(t), v_{\text{out},r}(t)$	conditioned output signals
v_{RF}	mixer input signal
$v_{\text{src}}(t), v_{\text{src2}}(t)$	source signals
$v_{\text{sup}}(t)$	suppressed carrier signal
$\underline{v}_{\text{ideal}}$	ideal source signal
V_0	amplitude of $v(t)$
V_0	diode material specific voltage

V_1, V_2	amplitudes of signals
V_{bias}	bias voltage
V_{DUT}	amplitude of the DUT signal
ω	angular frequency
ω_0	fundamental angular frequency
W_{el}	electric energy
W_{mag}	magnetic energy
$x(t)$	time-based fluctuation of phase
$y(t)$	time-based fluctuation of frequency
$y_{\text{IQ}}(t)$	sinusoidal time signal
$\overline{y}_k(\tau)$	normalized measured time signal
$z(t)$	noisy signal

List of Figures

List of Tables

Bibliography

[1] K. Balewski, W. Brefeld, W. Decking, H. Franz, R. Röhlsberger, and E. Weckert, "PETRA III: A low emittance synchrotron radiation source (Technical design report)", Deutsches Elektronen-Synchrotron, DESY, Hamburg, 2004, 558 pp. DOI: 10.3204/PUBDB-2017-10776.

[2] M. Altarelli, R. Brinkmann, M. Chergui, W. Decking, B. Dobson, S. Düsterer, G. Grübel, W. Graeff, H. Graafsma, J. Hajdu, J. Marangos, J. Pflüger, H. Redlin, D. Riley, I. Robinson, J. Rossbach, A. Schwarz, K. Tiedtke, T. Tschentscher, I. Vartaniants, H. Wabnitz, H. Weise, R. Wichmann, K. Witte, A. Wolf, M. Wulff, and M. Yurkov, "XFEL, the European X-ray Free-Electron Laser: Technical Design Report", 2006.

[3] W. Ackermann, G. Asova, V. Ayvazyan, A. Azima, N. Baboi, J. Bähr, V. Balandin, B. Beutner, A. Brandt, A. Bolzmann, R. Brinkmann, O. I. Brovko, M. Castellano, P. Castro, L. Catani, E. Chiadroni, S. Choroba, A. Cianchi, J. T. Costello, D. Cubaynes, J. Dardis, W. Decking, H. Delsim-Hashemi, A. Delserieys, G. Di Pirro, M. Dohlus, S. Düsterer, A. Eckhardt, H. T. Edwards, B. Faatz, J. Feldhaus, K. Flöttmann, J. Frisch, L. Fröhlich, T. Garvey, U. Gensch, C. Gerth, M. Görler, N. Golubeva, H.-J. Grabosch, M. Grecki, O. Grimm, K. Hacker, U. Hahn, J. H. Han, K. Honkavaara, T. Hott, M. Hüning, Y. Ivanisenko, E. Jaeschke, W. Jalmuzna, T. Jezynski, R. Kammering, V. Katalev, K. Kavanagh, E. T. Kennedy, S. Khodyachykh, K. Klose, V. Kocharyan, M. Körfer, M. Kollewe, W. Koprek, S. Korepanov, D. Kostin, M. Krassilnikov, G. Kube, M. Kuhlmann, C. L. S. Lewis, L. Lilje, T. Limberg, D. Lipka, F. Löhl, H. Luna, M. Luong, M. Martins, M. Meyer, P. Michelato, V. Miltchev, W. D. Möller, L. Monaco, W. F. O. Müller, O. Napieralski, O. Napoly, P. Nicolosi, D. Nölle, T. Nuñez, A. Oppelt, C. Pagani, R. Paparella, N. Pchalek, J. Pedregosa-Gutierrez, B. Petersen, B. Petrosyan, G. Petrosyan, L. Petrosyan, J. Pflüger, E. Plönjes, L. Poletto, K. Pozniak, E. Prat, D. Proch, P. Pucyk, P. Radcliffe, H. Redlin, K. Rehlich, M. Richter, M. Roehrs, J. Roensch, R. Romaniuk, M. Ross, J. Rossbach, V. Rybnikov, M. Sachwitz, E. L. Saldin, W. Sandner, H. Schlarb, B. Schmidt,

M. Schmitz, P. Schmüser, J. R. Schneider, E. A. Schneidmiller, S. Schnepp, S. Schreiber, M. Seidel, D. Sertore, A. V. Shabunov, C. Simon, S. Simrock, E. Sombrowski, A. A. Sorokin, P. Spanknebel, R. Spesyvtsev, L. Staykov, B. Steffen, F. Stephan, F. Stulle, H. Thom, K. Tiedtke, M. Tischer, S. Toleikis, R. Treusch, D. Trines, I. Tsakov, E. Vogel, T. Weiland, H. Weise, M. Wellhöfer, M. Wendt, I. Will, A. Winter, K. Wittenburg, W. Wurth, P. Yeates, M. V. Yurkov, I. Zagorodnov, and K. Zapfe, "Operation of a free-electron laser from the extreme ultraviolet to the water window", *Nature Photonics*, vol. 1, no. 6, pp. 336–342, Jun. 2007, ISSN: 1749-4885, 1749-4893. DOI: 10.1038/nphoton.2007.76.

[4] H. Weise, "The TESLA XFEL Project", presented at the EPAC 2004, MOYCH01, Lucerne, Switzerland. [Online]. Available: https://accelconf.web.cern.ch/e04/TALKS/MOYCH01.PDF (visited on 04/05/2022).

[5] W. Decking and H. Weise, "Commissioning of the European XFEL Accelerator", in *Proc. 8th Int. Particle Accelerator Conf. (IPAC'17)*, Copenhagen, Denmark, May 2017. DOI: https://doi.org/10.18429/JACoW-IPAC2017-MOXAA1.

[6] H. Schlarb, V. Ayvazyan, F. Ludwig, D. Nölle, B. Schmidt, and S. Simrock, "Next Generation Synchronization System for the VUV-FEL at DESY", presented at the 27th International Conference on Free Electron Lasers, Palo Alto, USA, 2005, pp.118. [Online]. Available: https://www.researchgate.net/publication/228749500_Next_Generation_Synchronization_System_for_the_VUV-FEL_at_DESY (visited on 11/21/2021).

[7] F. Ludwig, M. Hoffmann, H. Schlarb, and S. Simrock, "Phase Stability of the Next Generation RF Field Control for VUV- and X-Ray Free Electron Laser", presented at the EPAC 2006, Edinburgh. [Online]. Available: https://accelconf.web.cern.ch/e06/PAPERS/TUPCH188.PDF (visited on 01/23/2022).

[8] F. Ludwig, J. Branlard, Ł. Butkowski, M. Czwalinna, M. Hierholzer, M. Hoffmann, M. Killenberg, M. Kuntzsch, T. Lamb, J. Marjanovic, U. Mavrič, J. Müller, S. Pfeiffer, H. Schlarb, C. Schmidt, L. Springer, and K. Zenker, "RF Controls Towards Femtosecond and Attosecond Precision", *Proceedings of the 10th Int. Particle Accelerator Conf.*, vol. IPAC2019, 5 pages, 2019. DOI: 10.18429/JACOW-IPAC2019-THYPLS1.

[9] P. Grychtol, D. E. Rivas, T. M. Baumann, R. Boll, A. De Fanis, B. Erk, M. Ilchen, J. Liu, T. Mazza, J. Montaño, J. Müller, V. Music, Y. Ovcharenko, N. Rennhack, A. Rouzé, P. Schmidt, S. Schulz, S. Usenko, R. Wagner, P. Ziołkowski, H. Schlarb, J. Grünert, N. Kabachnik, and M. Meyer, "Timing and X-ray pulse characterization at the Small Quantum Systems instrument of the European X-ray Free Electron Laser", *Optics Express*, vol. 29, no. 23, p. 37 429, Nov. 8, 2021. DOI: 10.1364/OE.440718.

[10] T. Schilcher, "Vector Sum Control of Pulsed Accelerating Fields in Lorentz Force Detuned Superconducting Cavities", PhD thesis, Universität Hamburg, 1998.

[11] M. Hoffmann, "Development of a multichannel RF field detector for the Low-Level RF control of the Free-Electron Laser at Hamburg", PhD thesis, Technische Universität Hamburg, Hamburg, 2008.

[12] H. T. Friis, "Noise Figures of Radio Receivers", *Proceedings of the IRE*, vol. 32, 1944. DOI: 10.1109/JRPROC.1944.232049.

[13] "SACLA at RIKEN", RIKEN Center, Japan. [Online]. Available: https://www.riken.jp/en/collab/resources/sacla/ (visited on 11/25/2021).

[14] "SwissFEL at PSI", Paul Scherrer Institut, Switzerland. [Online]. Available: https://www.psi.ch/en/swissfel (visited on 11/25/2021).

[15] "LCLS at SLAC", SLAC National Accelerator Laboratory, US. [Online]. Available: https://lcls.slac.stanford.edu/ (visited on 11/25/2021).

[16] C. Horn, "A Carrier Suppression Technique for Measuring S/N and Carrier/Sideband Ratios Greater Than 120 dB", in *23rd Annual Symposium on Frequency Control*, Atlantic City, USA: IEEE, 1969, pp. 223–235. DOI: 10.1109/FREQ.1969.199765.

[17] K. Sann, "The Measurement of Near-Carrier Noise in Microwave Amplifiers", *IEEE Transactions on Microwave Theory and Techniques*, vol. 16, no. 9, pp. 761–766, Sep. 1968, ISSN: 0018-9480. DOI: 10.1109/TMTT.1968.1126783.

[18] F. Labaar, "New Discriminator Boosts Phase-Noise Testing", *Microwaves*, vol. 21, no. 3, 1982.

[19] E. Rubiola and V. Giordano, "A Low-Flicker Scheme for the Real-Time Measurement of Phase Noise", *IEEE Transactions on Ultrasonics, Ferroelectrics and Frequency Control*, vol. 49, no. 4, pp. 501–507, 2002. DOI: 10.1109/58.996569.

[20] E. Rubiola and V. Giordano, "Advanced interferometric phase and amplitude noise measurements", *Review of Scientific Instruments*, vol. 73, no. 6, pp. 2445–2457, Jun. 2002. DOI: 10.1063/1.1480458.

[21] E. Rubiola, V. Giordano, and J. Groslambert, "Very high frequency and microwave interferometric phase and amplitude noise measurements", *Review of Scientific Instruments*, vol. 70, no. 1, pp. 220–225, Jan. 1999. DOI: 10.1063/1.1149351.

[22] E. Ivanov, M. Tobar, and R. Woode, "Microwave Interferometry: Application to Precision Measurements and Noise Reduction Techniques", *IEEE Transactions on Ultrasonics, Ferroelectrics and Frequency Control*, vol. 45, no. 6, pp. 1526–1536, Nov. 1998. DOI: 10.1109/58.738292.

[23] "Argonne National Laboratory", US. [Online]. Available: https://www.anl.gov/ (visited on 11/25/2021).

[24] P. Buabthong and T. Berenc, "Interferometric Residual Phase Noise Measurement System", 2013. [Online]. Available: https://indico.fnal.gov/event/7241/contributions/101101/attachments/65910/79076/FinalPaper_InterferometricSystem.pdf (visited on 03/22/2021).

[25] L. Springer, "Untersuchung von Hochfrequenzdetektoren mit Trägerunterdrückung für die Regelung von Beschleunigerkavitäten im Attosekundenbereich", Master's thesis, Hamburg University of Technology, 2018.

[26] M. Thumm, W. Wiesbeck, and S. Kern, *Hochfrequenzmesstechnik*. Vieweg+Teubner, 1998, ISBN: 978-3-663-01599-4.

[27] E. Rubiola, *Phase Noise and Frequency Stability in Oscillators*. Cambridge University Press, 2009, ISBN: 978-0-521-15328-7.

[28] D. M. Fleetwood, "Origins of 1/f Noise in Electronic Materials and Devices: A Historical Perspective", in *Noise in Nanoscale Semiconductor Devices*, Springer International Publishing, 2020, pp. 1–31. DOI: 10.1007/978-3-030-37500-3_1.

[29] F. Hooge and A. Hoppenbrouwers, "Contact Noise", *Physics Letters A*, vol. 29, no. 11, pp. 642–643, Aug. 1969. DOI: 10.1016/0375-9601(69)90175-3.

[30] G. G. MacFarlane, "A Theory of Flicker Noise in Valves and Impurity Semi-Conductors", *Proceedings of the Physical Society*, vol. 59, no. 3, pp. 366–375, May 1, 1947. DOI: 10.1088/0959-5309/59/3/303.

[31] ——, "A Theory of Contact Noise in Semiconductors", *Proceedings of the Physical Society. Section B*, vol. 63, no. 10, pp. 807–814, Oct. 1, 1950. DOI: 10.1088/0370-1301/63/10/308.

[32] P. Dutta and P. M. Horn, "Low-frequency fluctuations in solids: 1/f noise", *Reviews of Modern Physics*, vol. 53, no. 3, pp. 497–516, Jul. 1, 1981. DOI: 10.1103/RevModPhys.53.497.

[33] J. Cohen, "Three Guises of Generation-Recombination Noise", 1983, NBS technical note. [Online]. Available: https://nvlpubs.nist.gov/nistpubs/Legacy/TN/nbstechnicalnote1173.pdf (visited on 04/30/2022).

[34] H. W. Ott, *Noise Reduction Techniques in Electronic Systems*, 2nd ed. New York: Wiley, 1988, 426 pp., ISBN: 978-0-471-85068-7.

[35] F. Hooge, "1/f Noise Sources", *IEEE Transactions on Electron Devices*, vol. 41, no. 11, pp. 1926–1935, Nov. 1994. DOI: 10.1109/16.333808.

[36] M. Gupta, "Thermal Noise in Nonlinear Resistive Devices and its Circuit Representation", *Proceedings of the IEEE*, vol. 70, no. 8, pp. 788–804, 1982. DOI: 10.1109/PROC.1982.12405.

[37] A. Van Der Ziel, "Flicker Noise in Electronic Devices", in *Advances in Electronics and Electron Physics*, vol. 49, Elsevier, 1979, pp. 225–297. DOI: 10.1016/S0065-2539(08)60768-4.

[38] J. Barnes, A. Chi, L. Cutler, D. Healey, D. Leeson, T. McGunigai, J. Mullen, W. Smith, R. Sydnor, R. Vessot, and G. Winkler, "Characterization of Frequency Stability", 1970, National Bureau of Standards, NBS. [Online]. Available: https://www.govinfo.gov/content/pkg/GOVPUB-C13-a37cdb50e80b2eac88039ece7516b889/pdf/GOVPUB-C13-a37cdb50e80b2eac88039ece7516b889.pdf (visited on 05/03/2022).

[39] M. Meyer, *Signalverarbeitung*, 6th ed. Vieweg+Teubner, 2011, ISBN: 978-3-658-02612-7.

[40] C. E. Calosso and E. Rubiola, "Phase noise and jitter in digital electronics", 2017. [Online]. Available: http://www.rubiola.org/pdf-articles/archives/2016-arXiv-1701.00094-Digital-electronics.pdf (visited on 05/27/2021).

[41] D. Howe and T. Tasset, "Clock Jitter Estimation based on PM Noise Measurements", in *IEEE International Frequency Control Sympposium and PDA Exhibition Jointly with the 17th European Frequency and Time Forum, 2003. Proceedings of the 2003*, Tampa, USA: IEEE, 2003, pp. 541–546. DOI: 10.1109/FREQ.2003.1275149.

[42] *IEEE Standard Definitions of Physical Quantities for Fundamental Frequency and Time Metrology—Random Instabilities.* 2009, ISBN: 978-0-7381-6855-5.

[43] S. A. Maas, *Noise in Linear and Nonlinear Circuits*. Artech House Microwave Library, 2005, ISBN: 978-1580538497.

[44] *Phase noise characterization of microwave oscillators*, Application note, 1985. [Online]. Available: https://hpmemoryproject.org/an/pdf/pn11729C-2.pdf.

[45] E. Rubiola, R. Boudot, and Y. Gruson, "The effect of AM noise on correlation PM noise measurements", May 31, 2007, CNRS, Université de Franche Comté, Besancon, Presentation. (visited on 04/02/2022).

[46] D. M. Pozar, *Microwave Engineering*, 4th ed. Hoboken, NJ: Wiley, 2012, 732 pp., ISBN: 978-0-470-63155-3.

[47] *Phase Noise Measurement Solutions*, Selection Guide, Keysight Technologies, Jan. 26, 2018. [Online]. Available: https://www.keysight.com/de/de/assets/7018-02528/technical-overviews/5990-5729.pdf (visited on 07/26/2021).

[48] D. Owen, "Good Practice Guide to Phase Noise Measurement", Measurement good practice guide, May 2004. [Online]. Available: http://eprintspublications.npl.co.uk/3519/.

[49] C. Ziomek and P. Corredoura, "Digital I/Q Demodulator", in *Proceedings Particle Accelerator Conference*, vol. 4, Dallas, TX, USA: IEEE, 1995, pp. 2663–2665. DOI: 10.1109/PAC.1995.505652.

[50] S. Simrock and Z. Geng, *Low-Level Radio Frequency Systems*. 2022, ISBN: 978-3-030-94419-3.

[51] T. Kowalski, G. P. Gibiino, J. Szewiński, K. Czuba, D. Rybka, K. Chmielewski, Z. Wojciechowski, and M. Sitek, "Experimental Evaluation of Sub-Sampling IQ Detection for Low-Level RF Control in Particle Accelerator Systems", *Sensors*, vol. 22, no. 1, p. 38, Dec. 22, 2021. DOI: 10.3390/s22010038.

[52] L. Doolittle, H. Ma, and M. S. Champion, "Digital Low-Level RF Control using Non-IQ Sampling", *Proceedings of LINAC 2006*, 2006. [Online]. Available: https://accelconf.web.cern.ch/l06/papers/thp004.pdf (visited on 01/18/2022).

[53] T. Schilcher, "RF applications in digital signal processing", Paul Scherrer Institut, Villigen, Switzerland, 2008. [Online]. Available: https://cds.cern.ch/record/1100538/files/p249.pdf (visited on 06/15/2022).

[54] Y. W. Lee, T. Cheatham, and J. B. Wiesner, "The Application of Correlation Functions in the Detection of Small Signals in Noise", in *RLE Technical Reports*, vol. 141, Research Laboratory of Electronics, Massachusetts Institute of Technology, 1949. [Online]. Available: http://hdl.handle.net/1721.1/4912 (visited on 07/12/2021).

[55] M. Sampietro, L. Fasoli, and G. Ferrari, "Spectrum analyzer with noise reduction by cross-correlation technique on two channels", *Review of Scientific Instruments*, vol. 70, no. 5, pp. 2520–2525, May 1999. DOI: 10.1063/1.1149785.

[56] A. I. Harris, "Spectroscopy with multichannel correlation radiometers", *Review of Scientific Instruments*, vol. 76, no. 5, p. 054 503, May 2005. DOI: 10.1063/1.1898643.

[57] E. Rubiola and F. Vernotte, "The cross-spectrum experimental method", 2010. [Online]. Available: http://arxiv.org/abs/1003.0113 (visited on 07/12/2021).

[58] S. Oberholzer, "Fluctuation Phenomena in Low Dimensional Conductors", 2001. DOI: 10.13140/RG.2.2.19601.74080. (visited on 07/12/2021).

[59] G. Bärwolff, *Höhere Mathematik für Naturwissenschaftler und Ingenieure*, 3. Auflage, in collab. with G. Seifert, ser. Lehrbuch. Berlin; [Heidelberg]: Springer Spektrum, 2017, 997 pp., ISBN: 978-3-662-55022-9.

[60] "R&S® FSWP Phasenrausch- und VCO-Messplatz", 81671 München, Manual, 2017, Rohde&Schwarz GmbH& Co. KG. [Online]. Available: https://cdn.rohde-schwarz.com/pws/dl_downloads/dl_common_library/dl_brochures_and_datasheets/pdf_1/FSWP_bro_de_3607-2090-11_v0500.pdf (visited on 07/14/2021).

[61] A. Hati, D. A. Howe, F. L. Walls, and D. Walker, "Noise Figure vs. PM Noise Measurements: A Study at Microwave Frequencies", in *IEEE International Frequency Control Symposium and PDA Exhibition jointly with the 17th European Frequency and Time Forum, 2003*, 2003, pp. 516–520. DOI: 10.1109/FREQ.2003.1275144.

[62] F. Ludwig, "High Performance Measurement Applications in MicroTCA.4", 2016, Presentation. [Online]. Available: https://indico.cern.ch/event/489996/contributions/2299444/attachments/1343905/2025168/Frank_Ludwig.pdf (visited on 06/28/2022).

[63] U. Mavrič, "Calibration of the FFT y-axis for reading phase and amplitude noise in an SSA-like format", May 18, 2020, Internal Documentation, DESY.

[64] "RO4000 series", Data Sheet, Advanced Connectivity Solutions, Rogers Corp. [Online]. Available: https://rogerscorp.com/-/media/project/rogerscorp/documents/advanced-electronics-solutions/english/data-sheets/ro4000-laminates-ro4003c-and-ro4350b---data-sheet.pdf (visited on 10/28/2021).

[65] L. Springer, F. Ludwig, U. Mavrič, V. Vasylyuk, H. Pryschelski, M. Hoffmann, H. Schlarb, A. Kölpin, and A. F. Jacob, "Phase Noise Measurements for L-Band Applications at Attosecond Resolution", *IEEE Transactions on Instrumentation and Measurement*, vol. 71, pp. 1–7, 2022. DOI: 10.1109/TIM.2022.3170975.

[66] W. Schottky, "Über spontane Stromschwankungen in verschiedenen Elektrizitätsleitern", *Annalen der Physik*, vol. 362, no. 23, pp. 541–567, 1918. DOI: 10.1002/andp.19183622304.

[67] T. Kleinpenning, "Noise in p-n Diodes", *Physica B+C*, vol. 98, no. 4, pp. 289–299, Mar. 1980. DOI: 10.1016/0378-4363(80)90045-5.

[68] M. J. Wiggins, "An Experimental Study of 1/f Noise in Transistors", *IEEE Transactions on Broadcast and Television Receivers*, vol. BTR-10, no. 1, pp. 84–92, May 1964. DOI: 10.1109/TBTR1.1964.6312042.

[69] G. Vasilescu, *Electronic Noise and Interfering Signals: Principles and Applications*. Berlin, Heidelberg: Springer-Verlag Berlin Heidelberg, 2005, ISBN: 978-3-540-26510-8.

[70] "E5052B Signal Source Analyzer", Data Sheet, 2017, Keysight Technologies. [Online]. Available: https://www.keysight.com/de/de/assets/7018-01528/data-sheets/5989-6388.pdf (visited on 01/06/2022).

[71] "HA7062D Phase Noise Analyzer", Data Sheet, Holzworth Instrumentation. [Online]. Available: https://www.holzworth.com/Portals/0/HA7062D_Web_Datasheet_1.pdf (visited on 01/06/2022).

[72] "MS2840A Signal Analyzer", Data Sheet, Anritsu. [Online]. Available: https://dl.cdn-anritsu.com/en-en/test-measurement/files/Brochures-Datasheets-Catalogs/Brochure/ms2840a-040-041-e1800.pdf (visited on 01/06/2022).

[73] "APPH signal source analyzer", Data Sheet, AnaPico AG. [Online]. Available: https://www.anapico.com/products/phase-noise-analyzers/apph-models-up-to-40-ghz/ (visited on 01/06/2022).

[74] C. Boggs, A. Doak, and F. Walls, "Measurement of Voltage Noise in Chemical Batteries", in *Proceedings of the 1995 IEEE International Frequency Control Symposium (49th Annual Symposium)*, San Francisco, USA: IEEE, 1995, pp. 367–373. DOI: 10.1109/FREQ.1995.483923.

[75] "Skyworks Solution Inc.", Website, 2008, Varactor Diodes. [Online]. Available: https://www.skyworksinc.com/en/Products/Varactor-Diodes (visited on 07/14/2021).

[76] U. Tietze, C. Schenk, and E. Gamm, *Halbleiter-Schaltungstechnik*, 13th ed. 2010, ISBN: 978-3-662-48553-8.

[77] F. Bonani and G. Ghione, *Noise in Semiconductor Devices Modeling and Simulation*. 2001, ISBN: 978-3-662-04530-5.

[78] G. Trefán and L. Vandamme, "1/f noise in homogeneous and inhomogeneous media", *IEE Proceedings - Circuits, Devices and Systems*, vol. 149, no. 1, pp. 3–12, Feb. 1, 2002. DOI: 10.1049/ip-cds:20020329.

[79] D. A. Bell, "A survey of 1/f noise in electrical conductors", *Journal of Physics C: Solid State Physics*, vol. 13, no. 24, pp. 4425–4437, 1980. DOI: 10.1088/0022-3719/13/24/007.

[80] F. N. Hooge, T. G. M. Kleinpenning, and L. K. J. Vandamme, "Experimental studies on 1/f noise", *Reports on Progress in Physics*, vol. 44, no. 5, pp. 479–532, 1981. DOI: 10.1088/0034-4885/44/5/001.

[81] R. Zettler and A. Cowley, "P-N Junction-Schottky Barrier Hybrid Diode", *IEEE Transactions on Electron Devices*, vol. 16, no. 1, pp. 58–63, Jan. 1969. DOI: 10.1109/T-ED.1969.16565.

[82] T. Kleinpenning, "Low-Frequency Noise in Schottky Barrier Diodes", *Solid-State Electronics*, vol. 22, no. 2, pp. 121–128, Feb. 1979. DOI: 10.1016/0038-1101(79)90103-5.

[83] A. V. Klyuev, E. I. Shmelev, and A. V. Yakimov, "Sources of 1/f Noise in Si Delta-Doped Schottky Diodes", in *2011 21st International Conference on Noise and Fluctuations*, Toronto, Canada: IEEE, 2011, pp. 102–105. DOI: 10.1109/ICNF.2011.5994273.

[84] K. Lange, K. H. Löcherer, H. H. Meinke, and F. W. Gundlach, Eds., *Taschenbuch der Hochfrequenztechnik: Grundlagen, Komponenten, Systeme*, 4., völlig neubearb. Aufl, Berlin: Springer, 1986, ISBN: 978-3-642-96894-5.

[85] B. S. Murthy and P. R. S. Rao, "Frequency Dependence of Junction Capacitance", *IETE Journal of Research*, vol. 17, no. 7, pp. 273–276, Jul. 1971. DOI: 10.1080/03772063.1971.11486806.

[86] "Infineon Technologies AG", Website, Varactor diodes. [Online]. Available: https://www.infineon.com/cms/de/product/rf-wireless-control/rf-diode/ (visited on 07/14/2021).

[87] T. I. Băjenescu and M. I. Bâzu, "Noise and reliability", in *Reliability of Electronic Components*. Berlin, Heidelberg: Springer Berlin Heidelberg, 1999, pp. 329–338, ISBN: 978-3-642-63625-7.

[88] C. D. Motchenbacher and J. A. Connelly, *Low-Noise Electronic System Design*. New York: Wiley, 1993, 422 pp., ISBN: 978-0-471-57742-3.

[89] A. Victor, J. Nath, D. Ghosh, B. Boyette, J.-P. Maria, M. Steer, A. Kingon, and G. Stauf, "Noise characteristics of an oscillator with a barium strontium titanate (BST) varactor", *IEE Proceedings - Microwaves, Antennas and Propagation*, vol. 153, no. 1, p. 96, 2006. DOI: 10.1049/ip-map:20050068.

[90] D. Chase, Lee-Yin Chen, and R. York, "Modeling the Capacitive Nonlinearity in Thin-Film BST Varactors", *IEEE Transactions on Microwave Theory and Techniques*, vol. 53, no. 10, pp. 3215–3220, 2005. DOI: 10.1109/TMTT.2005.855141.

[91] R. Jakoby, P. Scheele, S. Muller, and C. Weil, "Nonlinear Dielectrics for Tunable Microwave Components", in *15th International Conference on Microwaves, Radar and Wireless Communications (IEEE Cat. No.04EX824)*, Warsaw, Poland: IEEE, 2004, pp. 369–378. DOI: 10.1109/MIKON.2004.1357043.

[92] "STMicroelectronics", Website, RF tunable capacitors. [Online]. Available: https://www.st.com/en/emi-filtering-and-signal-conditioning/rf-tunable-capacitors (visited on 07/14/2021).

[93] H. Maune, M. Jost, R. Reese, E. Polat, M. Nickel, and R. Jakoby, "Microwave Liquid Crystal Technology", *Crystals*, vol. 8, no. 9, p. 355, Sep. 5, 2018. DOI: 10.3390/cryst8090355.

[94] "Teledyne relays", Website, Electromechanical Relays. [Online]. Available: https://www.teledynedefenseelectronics.com/relays/ourproducts/electro%E2%80%8Bmechanicalrelays/Pages/Electromechanical-Relays.aspx (visited on 07/14/2021).

[95] "Analog devices, inc.", Website, MEMS Switches. [Online]. Available: https://www.analog.com/en/products/switches-multiplexers/mems-switches.html (visited on 07/14/2021).

[96] G. Rebeiz, Guan-Leng Tan, and J. Hayden, "RF MEMS Phase Shifters: Design and Applications", *IEEE Microwave Magazine*, vol. 3, no. 2, pp. 72–81, Jun. 2002. DOI: 10.1109/MMW.2002.1004054.

[97] G. Rebeiz, "Phase-Noise Analysis of MEMS-Based Circuits and Phase Shifters", *IEEE Transactions on Microwave Theory and Techniques*, vol. 50, no. 5, pp. 1316–1323, May 2002. DOI: 10.1109/22.999145.

[98] ——, *RF MEMS: Theory, Design, and Technology*. Hoboken, NJ: J. Wiley, 2003, 483 pp., ISBN: 978-0-471-20169-4.

[99] R. Goggin, P. Fitzgerald, J. Wong, B. Hecht, and M. Schirmer, "Fully integrated, high yielding, high reliability DC contact MEMS switch technology & control IC in standard plastic packages", in *2011 IEEE SENSORS Proceedings*, Limerick, Ireland: IEEE, 2011, pp. 958–961. DOI: 10.1109/ICSENS.2011.6127072.

[100] R. Goggin, P. Fitzgerald, B. Stenson, E. Carty, and P. McDaid, "Commercialization of a Reliable RF MEMS Switch with Integrated Driver Circuitry in a Miniature QFN Package for RF Instrumentation Applications", in *2015 IEEE MTT-S International Microwave Symposium*, Phoenix, USA, May 2015, pp. 1–4. DOI: 10.1109/MWSYM.2015.7166959.

[101] "Laurin AG", Website. [Online]. Available: https://laurin-ag.com/ (visited on 07/14/2021).

[102] T. Gabrielson, "Mechanical-Thermal Noise in Micromachined Acoustic and Vibration Sensors", *IEEE Transactions on Electron Devices*, vol. 40, no. 5, pp. 903–909, May 1993. DOI: 10.1109/16.210197.

[103] L. Melo, A. Vaz, M. Salvadori, and M. Cattani, "Grain Sizes and Surface Roughness in Platinum and Gold Thin Films", *Journal of Metastable and Nanocrystalline Materials*, vol. 20-21, pp. 623–628, Jul. 2004. DOI: 10.4028/www.scientific.net/JMNM.20-21.623.

[104] C. Kosla, P. Fitzgerald, and M. Hill, "Continuous dynamic timing measurements to monitor spring and surface forces in MEMS switch reliability", in *2014 IEEE 27th International Conference on Micro Electro Mechanical Systems (MEMS)*, San Francisco, USA, Jan. 2014, pp. 596–599. DOI: 10.1109/MEMSYS.2014.6765711.

[105] R. Holm, *Electric Contacts Theory and Application*. Springer-Verlag Berlin Heidelberg, 1967, ISBN: 978-3-662-06688-1.

[106] L. Vandamme, "On 1/f Noise in Ohmic Contacts", Publisher: Technische Hogeschool Eindhoven, PhD thesis, Technische Hogeschool Eindhoven, Eindhoven, Netherlands, 1976. [Online]. Available: https://research.tue.nl/en/publications/on-1f-noise-in-ohmic-contacts(e18c624c-8274-4404-9a2c-44a98d6bda94).html (visited on 04/01/2022).

[107] E. Rubiola and V. Giordano, "A low-flicker scheme for the real-time measurement of phase noise", in *Proceedings of the 2001 IEEE International Frequncy Control Symposium and PDA Exhibition (Cat. No.01CH37218)*, Seattle, USA, 2001, pp. 138–143. DOI: 10.1109/FREQ.2001.956177.

[108] W. D. Callister and D. G. Rethwisch, *Materialwissenschaften und Werkstofftechnik*. Wiley-VCH, 2012, ISBN: 978-3-527-33007-2.

[109] A. Stierle, T. F. Keller, H. Noei, V. Vonk, and R. Roehlsberger, "DESY NanoLab", *Journal of large-scale research facilities JLSRF*, vol. 2, A76, Jun. 9, 2016. DOI: 10.17815/jlsrf-2-140.

[110] H. V. D. Brom, "Noise Properties of Atomic-Size Contacts", PhD thesis, 2000. [Online]. Available: http://rgdoi.net/10.13140/RG.2.1.4367.5363 (visited on 04/01/2022).

[111] "Mini-Circuits SPHSA-152", Data Sheet. [Online]. Available: https://www.minicircuits.com/pdfs/SPHSA-152+.pdf (visited on 08/03/2021).

[112] A. Hauff, M. Brönnimann, I. Brunnenkant, A. Dietrich, F. Gärtner, Z. Geng, M. Jurcevic, R. Kalt, S. Mair, A. Rezaeizadeh, L. Schebacher, T. Schilcher, and W. Sturzenegger, "SwissFEL C-band LLRF prototype system", in *27th international linear accelerator conference*, TUPP111, 2014. [Online]. Available: https://s3.cern.ch/inspire-prod-files-1/179a1af7790f903577fb57dbcd869151 (visited on 04/23/2022).

[113] Q. Du, L. Doolittle, M. Betz, B. Flugstad, M. Vinco, and K. Baptiste, "Digital Low-Level RF control system for Advanced Light Source Storage Ring", 2019. DOI: 10.48550/ARXIV.1910.07175.

[114] A. Bellandi, V. Ayvazyan, J. Branlard, W. Cichalewski, C. Gümüş, S. Pfeiffer, K. Przygoda, R. Rybaniec, H. Schlarb, C. Schmidt, and J. Sekutowicz, "LLRF R&D Towards CW Operation of the European XFEL", *Proceedings of the 29th Linear Accelerator Conf.*, vol. LINAC2018, in collab. with S. RW (Ed.) Volker, P. Guoxi (Ed.), C. Ho (Ed.) Yong, F. Shinian (Ed.), and Z. Ning (Ed.), 4 pages, 2018. DOI: 10.18429/JACOW-LINAC2018-MOPO104.

[115] A. Bellandi, V. Ayvazyan, Ł. Butkowski, W. Cichalewski, B. Dursun, C. Gümüş, M. Omet, S. Pfeiffer, R. Onken, R. Rybaniec, C. Schmidt, V. Vogel, and J. Branlard, "Results on FPGA-Based High-Power Tube Amplifier Linearization at DESY", *IEEE Transactions on Nuclear Science*, vol. 67, no. 5, pp. 762–767, 2020. DOI: 10.1109/TNS.2020.2980929.

[116] A. Bellandi, "LLRF Control Techniques for the European XFEL Continuous Wave Upgrade", PhD thesis, Universität Hamburg, Hamburg, 2021.

[117] J. Branlard, V. Ayvazyan, A. Bellandi, J. Eschke, C. Gümüş, D. Kostin, K. Przygoda, H. Schlarb, and J. Sekutowicz, "Status of Cryomodule Testing at CMTB for CW R&D", in *19th International Conference on RF Superconductivity (SRF 2019)*, 2019. DOI: 10.18429/JACoW-SRF2019-THP092.

[118] "MicroTCA Technology Lab", [Online]. Available: https://techlab.desy.de/.

[119] J. Branlard, G. Ayvazyan, V. Ayvazyan, M. Grecki, M. Hoffmann, T. Jeżyński, F. Ludwig, U. Mavrič, S. Pfeiffer, H. Schlarb, C. Schmidt, H. Weddig, B. Yang, P. Barmuta, S. B. Habib, Ł. Butkowski, K. Czuba, M. Grzegrzółka, E. Janas, J. Piekarski, I. Rutkowski, D. Sikora, Ł. Zembala, M. Żukociński, W. Cichalewski, W. Jałmużna, D. Makowski, A. Mielczarek, A. Napieralski, P. Perek, A. Piotrowski, T. Poźniak, K. Przygoda, G. Bołtruczyk, S. Korolczuk, M. Kudła, J. Szewiński, K. Oliwa, and W. Wierba, "MTCA.4 LLRF System

for the European XFEL", in *Proceedings of the 20th International Conference Mixed Design of Integrated Circuits and Systems - MIXDES 2013*, Jun. 2013, pp. 109–112. [Online]. Available: https://ieeexplore.ieee.org/stamp/stamp.jsp?tp=&arnumber=6613323 (visited on 02/07/2022).

[120] U. Mavrič, M. Hoffmann, F. Ludwig, H. Schlarb, and L. Springer, "Automatic Loop for Carrier Suppression in Attosecond RF Receivers", *Proceedings of the 10th Int. Particle Accelerator Conf.*, vol. IPAC2019, 3 pages, 2019. DOI: 10.18429/JACOW-IPAC2019-THPRB021.

[121] C. Gerth, F. Ludwig, and H. Schlarb, "Beam Based Measurements of the RF Amplitude Stability at FLASH Using a Synchrotron Radiation Monitor", presented at the DIPAC09, Basel. [Online]. Available: https://accelconf.web.cern.ch/d09/papers/tupd22.pdf (visited on 04/15/2022).

[122] E. Rubiola and F. Vernotte, "The Companion of the Enrico's Chart for Phase Noise and Two-Sample Variances", Jan. 19, 2022. arXiv: 2201.07109.

[123] D. Allan, "Statistics of Atomic Frequency Standards", *Proceedings of the IEEE*, vol. 54, no. 2, pp. 221–230, 1966, ISSN: 0018-9219. DOI: 10.1109/PROC.1966.4634.

[124] E. Rubiola, "The Enrico's Chart for Phase Noise and Two-Sample Variances", Dec. 29, 2020. DOI: 10.5281/ZENODO.4915911.